OPTOFLUIDIC MICROSCOPY AND WAVEFRONT MICROSCOPY: INNOVATIONS IN BIOLOGICAL IMAGING

Thesis by

Xiquan Cui

In Partial Fulfillment of the Requirements

for the Degree of

Doctor of Philosophy

California Institute of Technology

Pasadena, California

2010

(Defended on November 18th, 2009)

Thesis Committee

Professor Changhuei Yang (Chair)

Professor Amnon Yariv

Professor Yu-Chong Tai

Professor Scott E. Fraser

Professor Harry A. Atwater

This thesis is dedicated to my family.

Acknowledgments

The successful completion of my thesis has relied on the support from many individuals. I am grateful for their caring and guidance during my enjoyable graduate study at Caltech.

First of all, I would like to express my sincere gratitude to my advisor, Professor Changhuei Yang. Yang is absolutely supportive to my research, and I really enjoy working in the Biophotonics lab. Yang gave me the complete freedom to learn and access any resources that could help the development of OFM. I feel my ability of performing independent research has grown a great deal during my Ph.D. study, and I truly appreciate Yang's belief in me. In addition, Yang has amazing passion for scientific research. He always can bring up a new idea every time I see him. It totally stirs up my zeal to research as well. I am very thankful that Yang has taught me how to think like a creative researcher.

I am also grateful to Professor Demetri Psaltis. He and his students have given me much generous help on the OFM project. The optofluidic center led by him also provided a great platform for me to communicate with experts from other institutes.

I feel deeply indebted to Professor Paul W. Sternberg and Professor Scott E. Fraser. They are always there to provide me precious advice and generous help, and to encourage me to grow.

I would like to thank Professor Harry A. Atwater, Professor Scott E. Fraser, Professor Ali Hajimiri, Professor Yu-Chong Tai, and Professor Amnon Yariv for being my thesis committee and/or my candidacy committee, and providing me their valuable

suggestions. They are all professors I admired. I wish I would accomplish similar achievement someday as they did.

I would also like to thank for the discussion and help from Professor Axel Scherer, Professor Babak Hassibi, Professor P. P. Vaidyanathan, Dr. Guillermo J. Tearney, Dr. C. Thomas Vangsness, Jr., and Dr. Richard J. Cote.

I have enjoyed working in the friendly and creative research group of Biophotonics at Caltech. Dr. Zahid Yaqoob, Dr. Xin Heng, and Dr. Jigang Wu have helped me quickly become involved in the lab when I first came to Caltech. Dr. Xin Heng, Lap Man Lee, Dr. Jigang Wu, and Sean Pang are my teammates on the OFM project, and I am thankful for their generous help and insightful discussions. Dr. Emily J. McDowell and I joined the group at the same year, and we have shared the same office for three years. I could not say enough thanks to express my gratitude to her constant help. Matthew Lew was my SURF student, and now is my great colleague. I really enjoy working with him and being friends with him. I would also like to thank other group members: Dr. Marinko V. Sarunic, Dr. Vahan Senekerimyan, Dr. Meng Cui, Guoan Zheng, Jian Ren, Shuo Pang, Ying Min Wang, Arthur Chang, and Tony Wu for their friendship and enjoyable communications during these years.

Thanks to Dr. Emily J. McDowell, Ying Min Wang, Dr. Meng Cui, Dr. Sri Rama Prasanna Pavani, and Dr. Michael Salvador for reading my thesis. I have learned a lot of from them to improve my writing skill.

Anne Sullivan, Christine Garske, Ya-Yun Liu, and Agnes Tong are our greatest secretaries. They have been extremely helpful to supply my research and take care of me in the lab. They make the lab feel like a home to me.

During my Ph.D. research at Caltech, I have also benefited a lot from the generous help from many collaborators: Dr. Weiwei Zhong (now at Rice University), Dr. Ying Zhou, Dr. Claudiu Giurumescu, Oren Schaedel, Dr. Xiaoyan Robert Bao, and Dr. Zhenyu Li, to name a few.

My final and most important acknowledgements contribute to my Dad, Jun Cui, my Mom, Guihua Wang, my sister, Yanyan Cui, for their love and support. Without their encouragement, I would not have had enough determination to complete my Ph.D. study.

Xiquan Cui

崔喜泉

Pasadena, CA

Fall, 2009

Abstract

This thesis presents two new microscopic imaging techniques: the optofluidic microscopy (OFM) and the wavefront microscopy (WM). By integrating optical functionalities onto a single semiconductor chip, these inventions could reduce the cost and improve the efficiency and quality of microscopic imaging in biological research and clinical diagnostics. First, OFM utilizes a microfluidic flow to deliver cellular samples across array(s) of micron-sized apertures defined on a metal-coated CMOS image sensor to acquire direct projection images of the samples. Although the OFM prototype is as small as a dime, it can render high resolution images (~1 μm) with comparable quality to those of a bulky standard optical microscope. OFM has great potential in revolutionizing the way we use microscopes. For example, the availability of tens or even hundreds of microscopes on a single chip will allow massively paralleled imaging of large populations of cells or microorganisms; the compactness and low cost of the OFM can enable portable and even disposable biomedical diagnostic tools for future telemedicine and personalized health care. Second, we present a new microscopy concept - WM. Wavefront image sensor (WIS) is the enabling component of WM. By monitoring the tightly confined transmitted light spots through a 2D aperture grid (spacing = 11 μm, diameter = 6 μm) fabricated on a CMOS image sensor in a high Fresnel number regime, we can accurately measure both intensity and phase front variations (a measured normalized phase gradient sensitivity of 0.1 mrad under the typical working condition - 1.0 second total signal accumulation time and 9.2 $\mu W/cm^2$ light intensity on the sensor) of a wavefront separately and quantitatively. Therefore, researchers and clinicians can

incorporate pure phase imaging into their current microscope systems by simply adding the WIS in place of the conventional camera. When combined with adaptive optics strategies, this technology will facilitate deep tissue imaging using multiphoton microscopy.

Table of Contents

Table of Figures

LIST OF FREQUENTLY USED ACRONYMS

Acronym	Full name
Al	Aluminium
C. elegans	*Caenorhabditis elegans*
CMOS	Complementary metal–oxide–semiconductor
DIC	Differential interference contrast
DIC-OFM	Differential interference contrast OFM
FWHM	Full width at half maximum
OFM	Optofluidic microscopy
PSF	Point spread function
N.A.	Numerical Aperture
SA	Structured aperture
SA-DIC	Structure aperture DIC
SAI	Structured aperture interference
SNR	Signal-to-noise ratio
WIS	Wavefront imaging sensor
WM	Wavefront microscopy

Chapter 1: Introduction

Seeing is believing! Optical microscopy has been one of the major tools used to see and understand the biological world since its first invention and the first discovery of the unit of life – the cell. At the same time, the variety and heterogeneity of biological problems also creates space for innovative ideas in optical microscopy. Here we will briefly introduce and discuss some of them.

In this beginning chapter, we will first introduce the classical imaging model of a conventional optical microscope. Based on that, we will then review how modern optical microscopy techniques break through the boundaries set by this imaging model and create new venues for bioscience and biomedicine research. At the end, we will introduce our efforts in this area, and outline the organization of this thesis.

1.1 Conventional optical microscopy

1.1.1 Configuration

Fundamentally, a conventional optical microscope consists of three major parts: an object, an objective lens and an image (Fig. 1-1 (a)). The basic function of the microscope is to magnify the small object into an image large enough to be observed. Based on the thin lens approximation, the governing equations are:

$$\begin{cases} \dfrac{1}{l_o}+\dfrac{1}{l_i}=\dfrac{1}{f} \\ M=\dfrac{l_i}{l_o}=\dfrac{h_2}{h_1} \end{cases}, \tag{1-1}$$

where l_o is the object distance, l_i is the image distance, f is the focal length of the objective lens, M is the magnification of the objective lens or the optical microscope, h_1 is the size of the object, and h_2 is the size of the image. Because the basic function of the microscope is magnification, it usually requires significant space l_i to project the image. This is one of main sources of difficulties for miniaturizing the microscope.

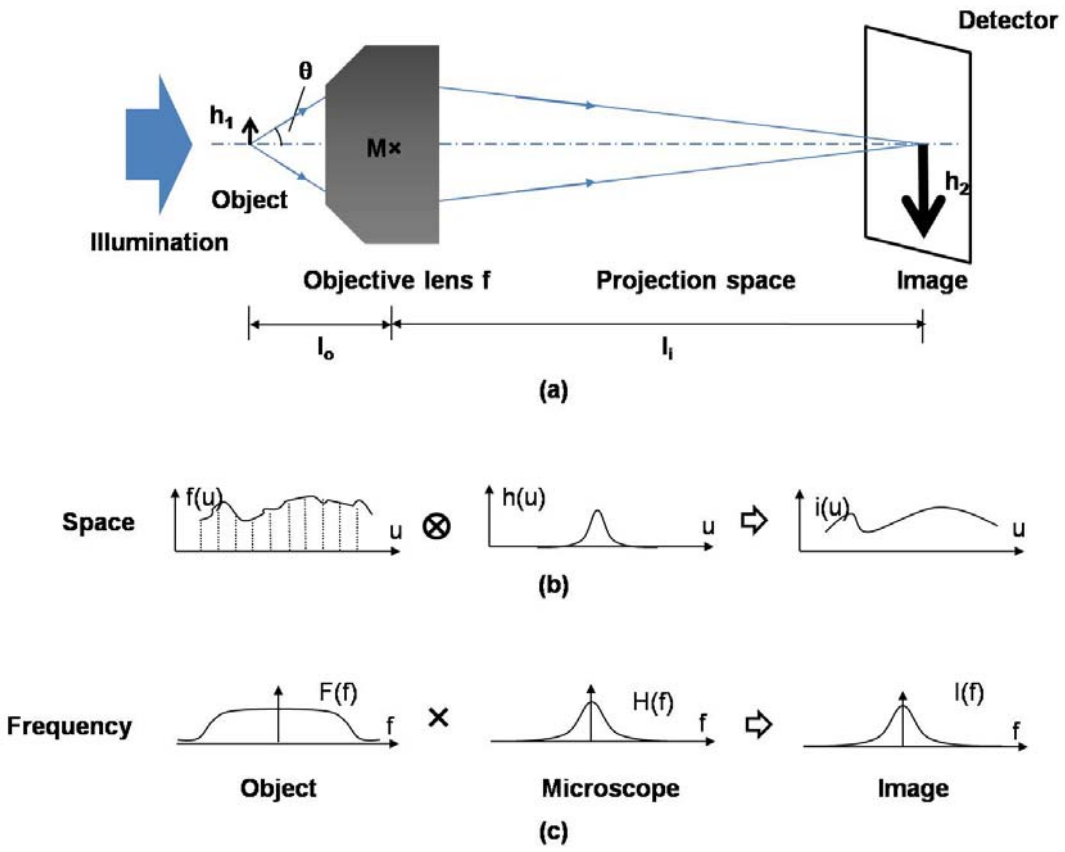

Figure 1-1 (color): Imaging principle of a standard optical microscope. (a) The object is magnified and projected onto the image plane by an objective lens. (b) In the space domain, the image function is the convolution of the object function and the point spread function (PSF) of the microscope. (c) In the frequency domain, the image spectrum is the product of the object spectrum and the effective low-pass filter of the microscope.

In reality, the ideal case of thin lens imaging is hard to achieve. First, the optical design of a good objective lens requires the combination of multiple lenses to correct optical aberrations. This is usually the reason why microscope systems are bulky, complicated, and expensive. Second, limited by the design difficulties and the physical

diameter of the objective lens, the microscope can only accept information carried by light within a certain angle range, θ. Based on Abbe's equation, the resolution of a microscope is defined as

$$R = \frac{0.61\lambda}{N.A.}, \tag{1-2}$$

where R is the resolution of the microscope, λ is the wavelength of the illumination, and $N.A.$ is the numerical aperture of the objective. $N.A.$ is defined as $n\sin\theta$, where n is the refractive index of the imaging medium. From Eq. (1-2), we can see that the resolution of the microscope is limited by the ability of the objective lens to collect the information of light. This can be better appreciated when the concepts of *signal and system* and *Fourier optics* are introduced.

1.1.2 Signal and system model of microscope imaging

From the *signal and system* point of view, the microscope is a linear system, and its impulse response characterizes the complete performance of the microscope.

When the object of the microscope is a point source, its image is always a blob. The size of the blob determines the closest lateral distance between two point sources at which we still can resolve them in the object, i.e., the resolution of the microscope. Usually we define the distribution of the blob as the point spread function (PSF) of the microscope.

In the space domain u (for clarity, we will be discussing the microscope imaging in 1D, and the result can be easily generalized in 2D.), if we consider that an object composed of point sources, its microscope image $i(u)$ is simply the convolution of the object function $f(u)$ and the PSF of the microscope system $h(u)$. Therefore, we will lose some details of the object in the microscope image (Fig. 1-1 (b)).

$$f(u) \otimes h(u) = i(u). \tag{1-3}$$

In the frequency domain f, the wide frequency spectrum of the object $F(f)$ will be truncated by the effective low-pass filter of the microscope system $H(f)$, and the information within the microscope image $I(f)$ will be less than that in the object spectrum $F(f)$ (Fig. 1-1 (c)).

$$F(f) \bullet H(f) = I(f). \tag{1-4}$$

From the *Fourier optics* point of view, we can decompose the object function into plane waves. If we collect all of the plane waves through the objective lens, ideally we should be able to restore a perfect image of the object.

$$\begin{cases} A(k_x, k_y) = \int_{-\infty}^{\infty}\int_{-\infty}^{\infty} O(x,y)\exp[-j(k_x x + k_y y)]dxdy \\ O(x,y) = \dfrac{1}{(2\pi)^2}\int_{-\infty}^{\infty}\int_{-\infty}^{\infty} A(k_x, k_y)\exp[j(k_x x + k_y y)]dk_x dk_y \end{cases}, \tag{1-5}$$

where $A(k_x, k_y)$ are coefficients of the decomposed plane waves, $O(x, y)$ is the object function in 2D, and k_x and k_y are the components of the k vectors of the plane waves.

However, limited by the $N.A.$ of the objective lens, $k_x^2 + k_y^2 < (\frac{2\pi}{\lambda} N.A.)^2$, we will lose some details of the object in the microscope image. We can increase the

resolution of the microscope by immersing the object into a medium with high refractive index n (i.e., microscopes with oil immersion objectives lens). The highest achievable resolution in such medium is $R = \frac{0.61\lambda}{n}$ when $\sin\theta = 1$. Because the above analysis is based on the diffraction theory, the ultimate achievable resolution of the microscope is also called the diffraction limit.

Limit! Does this necessarily mean we are hitting a hard wall in the research of optical microscopy? On the contrary, there are continuing ground-breaking research in this old but vibrant field.

1.2 Modern optical microscopy methods

Recently, there appear many new and exciting optical microscopy methods. The goals are either to break the diffraction limit and achieve super resolution, or, to change the format of optical microscopy to gain exceptional capabilities.

How can we break the diffraction limit? Unlike near field optical scanning microscopy (NSOM) [1, 2], recent super resolution microscopy methods aim to see more and clearer than conventional microscopy methods in the far field. For example, photo-activated localization microscopy (PALM) [3], fluorescence photoactivation localization microscopy (FPALM) [4], and stochastic optical reconstruction microscopy (STORM) [5] switch on individual fluorescent molecules and use Gaussian fitting to estimate their positions precisely. By repeating this process, these methods build up a super resolution image molecule by molecule. Even though these methods still utilize the same optical

configuration as a conventional microscope, they can distinguish two molecules closer than the resolution of the microscope because the positions of the two molecules are measured at different times. Stimulated emission depletion (STED) microscopy [6] utilizes a non-linear optical process to sharpen the PSF of the microscope and achieve super resolution images. The classic microscope model is based on linear optical processes, therefore it fails to limit the resolution of STED. Structured illumination microscopy (SIM) [7] generates spatial illumination gratings along multiple directions on the object to shift the high spatial frequency components of the object into the low frequency band of the conventional microscope. By stitching the object frequency bands back together numerically, the bandwidth and the lateral resolution of the final image are doubled. 4Pi microscopy [8, 9] uses two objective lenses to excite and/or collect signals from both sides of the specimen, so its effective *N.A.* is doubled, and both the axial resolutions of the microscope can be improved 3-7 times. The super resolution microscope images enabled by these “nanoscopy” techniques allow for direct visualization of biological events [6] and molecular interactions [5] at the nanometer scale.

Alternatively, being creative with the way we perform microscopy can also obtain extraordinary benefits. For example, stimulated Raman scattering microscopy (SRS) [10] illuminates the specimen with two laser beams. By tuning the frequency difference between the laser beams to match the vibrational frequency of certain type of molecules, we can probe molecules of interest in the specimen and image them free of background noise from other molecules. Single plane illumination microscopy (SPIM) [11] scans a thin 2D light sheet through the specimen from the side, and excites only a certain plane of

the specimen at a time. A camera efficiently captures the fluorescent photons emitted. This method allows high resolution fluorescent imaging in both axial and lateral directions with fast speed and generates less photobleaching to dye molecules. Double helix point spread function (DH-PSF) microscopy [12] uses a spatial light modulator in the Fourier plane to engineer the PSF of the microscope system in such a way that a fluorescent molecule appears as two dots in the image. The center of the two dots represents the lateral position of the molecule, and the angle of the line between them encodes the depth information of the molecule. One remarkable feature of this technique is its ability to perform 3D imaging. Adaptive microscopy either calculates [13] or measures [14] the optical aberration generated by the heterogeneity of the biological specimen itself, and uses a pre-deformed illumination wavefront to compensate the aberration. This way, we can achieve high resolution images even in deep and complicated biological tissues.

Creative microscopy research not only redefines the limit established by previous arts and provides new tools to see what people could not see before, but also inspires us to revisit the existing imaging theories and encourages thinking outside the box. In the rest of the thesis, we will present our views of modern optical microscopy.

1.3 Organization of the thesis

This thesis consists of two main parts in which we will present two microscope techniques developed in the Biophotonics group at Caltech: optofluidic microscopy (OFM) and wavefront microscopy (WM).

Part I describes the invention of OFM, a lensless, high-resolution and complete on-chip microscope method suitable for the application of compact and automated cell-level microscope imaging. In Chapter 2, we will present the construction and application of the first complete on-chip OFM device in an intuitive fashion. In Chapter 3, we will introduce the PSF and signal and system model of OFM imaging to discuss its resolution, sampling, and aliasing issues. In Chapter 4, we will introduce a new on-chip phase imaging method – structured aperture interference (SAI) and demonstrate the feasibility of creating a phase sensitive OFM device based on SAI.

Part II focuses on WM, a new microscopy method which detects both the amplitude and phase information of the wavefront induced by the specimen separately with a single data acquisition. In Chapter 5, we will introduce the enabling component of WM – the wavefront imaging sensor (WIS). In Chapter 6, we will demonstrate how to turn a standard microscope into a WM by simply adding the WIS onto the camera port of the microscope. In Chapter 7, we will discuss fundamental details about the imaging process of WM and WIS.

Bibliography

1. U. Dürig, D. Pohl, and F. Rohner, "Near field optical scanning microscopy," Journal of Applied Physics **59**, 3318 (1986).
2. E. Betzig, and R. Chichester, "Single molecules observed by near-field scanning optical microscopy," Science **262**, 1422-1425 (1993).
3. E. Betzig, G. Patterson, R. Sougrat, O. Lindwasser, S. Olenych, J. Bonifacino, M. Davidson, J. Lippincott-Schwartz, and H. Hess, "Imaging intracellular fluorescent proteins at nanometer resolution," (American Association for the Advancement of Science, 2006), pp. 1642-1645.
4. S. T. Hess, T. P. K. Girirajan, and M. D. Mason, "Ultra-high resolution imaging by fluorescence photoactivation localization microscopy," Biophysical Journal **91**, 4258-4272 (2006).
5. M. Rust, M. Bates, and X. Zhuang, "Sub-diffraction-limit imaging by stochastic optical reconstruction microscopy (STORM)," Nature Methods **3**, 793-796 (2006).
6. K. Willig, S. Rizzoli, V. Westphal, R. Jahn, and S. Hell, "STED microscopy reveals that synaptotagmin remains clustered after synaptic vesicle exocytosis," Nature **440**, 935-939 (2006).
7. M. Gustafsson, "Surpassing the lateral resolution limit by a factor of two using structured illumination microscopy," Journal of Microscopy **198**, 82 (2000).
8. S. Hell, S. Lindek, C. Cremer, and E. Stelzer, "Measurement of the 4Pi confocal point spread function proves 75 nm axial resolution," Applied Physics Letters **64**, 1335 (1994).
9. P. Hänninen, S. Hell, J. Salo, E. Soini, and C. Cremer, "Two photon excitation 4Pi confocal microscope: Enhanced axial resolution microscope for biological research," Applied Physics Letters **66**, 1698 (1995).
10. C. Freudiger, W. Min, B. Saar, S. Lu, G. Holtom, C. He, J. Tsai, J. Kang, and X. Xie, "Label-free biomedical imaging with high sensitivity by stimulated Raman scattering microscopy," Science **322**, 1857 (2008).
11. P. Keller, A. Schmidt, J. Wittbrodt, and E. Stelzer, "Reconstruction of zebrafish early embryonic development by scanned light sheet microscopy," Science **322**, 1065 (2008).
12. S. Pavani, M. Thompson, J. Biteen, S. Lord, N. Liu, R. Twieg, R. Piestun, and W. Moerner, "Three-dimensional, single-molecule fluorescence imaging beyond the diffraction limit by using a double-helix point spread function," Proceedings of the National Academy of Sciences **106**, 2995 (2009).
13. M. Booth, M. Neil, R. Juškaitis, and T. Wilson, "Adaptive aberration correction in a confocal microscope," Proceedings of the National Academy of Sciences **99**, 5788 (2002).
14. M. Rueckel, J. Mack-Bucher, and W. Denk, "Adaptive wavefront correction in two-photon microscopy using coherence-gated wavefront sensing," Proceedings of the National Academy of Sciences **103**, 17137 (2006).

PART I: OPTOFLUIDIC MICROSCOPY (OFM)

Part I is about optofluidic microscopy (OFM), a lensless, high-resolution and complete on-chip microscope method. Its invention allows low-cost, compact, automated and high-throughput optical microscope imaging available to the analysis of cell-level biological specimens.

In Chapter 2, we will present the construction and application of the first complete on-chip OFM device in an intuitive fashion. In Chapter 3, we will introduce the PSF and signal and system model of OFM to discuss its resolution, sampling and aliasing issues. In Chapter 4, we will introduce a new on-chip phase imaging method – structured aperture interference (SAI) and demonstrate the feasibility of creating phase sensitive OFM device based on SAI.

Chapter 2: Optofluidic Microscopy Method

In this chapter, we will report the first implementation of a high resolution (~ 0.9 μm), lensless, and highly compact (~ the size of dime) on-chip microscope device (Fig. 2-1) based on the optofluidic microscopy (OFM) method, and its potential applications in biomedicine and bioscience.

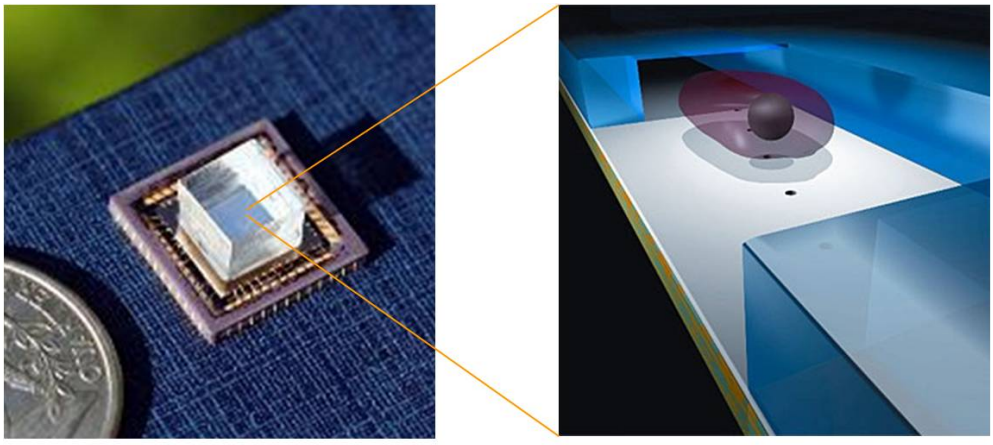

Figure 2-1 (color): The first completely on-chip OFM device. (a) Its size is comparable to a dime. **(b)** A high-resolution projection image of the specimen can be formed by flowing the specimen across the micron-sized apertures array in an OFM device.

We will begin with the motivation, "Why is an on-chip microscope device useful?". Then, we will overview the challenges discovered in previous attempts at on-

chip microscopy research, and introduce our solution to this problem - the OFM method. Next, we will describe how to construct an OFM device on a chip, how to operate it with a gravity driven flow, and report on its use for automated *Caenorhabditis elegans* (*C. elegans* or worm) imaging and quantitative phenotype characterization. After that, we will discuss some issues of OFM imaging, e.g., "What contrast are we looking at in an OFM image?", "How do we maintain steady movement of specimens in an OFM device to achieve good images?", and "How is the resolution of the OFM imaging impacted by the Brownian motion of the specimen in the microfluidic channel?" (Because the resolution characterization is the heart of a new imaging device, we will dedicate the entire Chapter 3 to discuss the resolution of an OFM device). Finally, we will conclude by briefly discussing potential applications of OFM devices.

2.1 Background

In spite of the long history of microscopy and the remarkable range of imaging tools that have been developed since the invention of the first microscope in the early 1600s, the fundamental design of microscopes has undergone little change. A typical microscope still consists of an objective, space for relaying the image, and an eyepiece or an imaging lens to project a magnified image onto a person's retina or a camera. In addition to its relatively high implementation cost (precise and expensive lenses are needed), the conventional microscope design has also proven difficult to miniaturize.

In recent years, there has been an explosion in the development of lab-on-a-chip systems [1-9]. The major advantages of these devices are their inherent compactness and low cost, which makes them suitable for both portable and point-of-care testing in clinical, bioscience, and even military settings. A high resolution and low cost on-chip microscope has been cited as one of the major tools that have, thus far, eluded induction into the family of on-chip instruments [10-11]. Therefore, inventing lensless on-chip microscope devices is developing into an interesting research area.

2.2 Lensless on-chip microscopy

Here, we will introduce some of the recent advance in the lensless on-chip microscopy. For example, digital inline holographic microscopy (DIHM) [12-13] showed that it is possible to render microscope-resolution images of objects without the use of lenses; however, as a method, DIHM requires significant post-measurement computation and the use of a coherent light source, which are impediments to widespread use.

In 2005, Lange et al. reported a direct projection method to implement compact and low cost imaging systems [14]. In Lange's method, the specimen is placed directly on a CMOS image sensor, and the projection image is then recorded by the sensor (Fig. 2-2 (a)). The resolution in such a system is given by the sensor pixel size. Since the typical pixel size of a commercial CCD or CMOS sensor is larger than 3 μm, this approach is incapable of yielding images that have resolution comparable to conventional microscope images (resolution of 1 μm or smaller). Despite the low image quality, recent

works [15] have shown that these pixelated images are useful for certain high-throughput cell identification applications.

Here we report a new lensless on-chip microscopy method – Optofluidic microscopy (OFM). We modify the direct projection imaging accordingly so that microscope-resolution images can be collected. We believe it can be a viable low-cost and compact replacement of the conventional microscope system for a range of applications.

2.3 Optofluidic microscopy

It is difficult to conceive or develop a direct projection imaging strategy by which single-time-point images at resolution better than the sensor pixel size can be acquired. However, if we permit ourselves to exploit the time dimension during the image acquisition process, it is possible to develop viable high resolution direct projection imaging strategies in which resolution and sensor pixel size are independent.

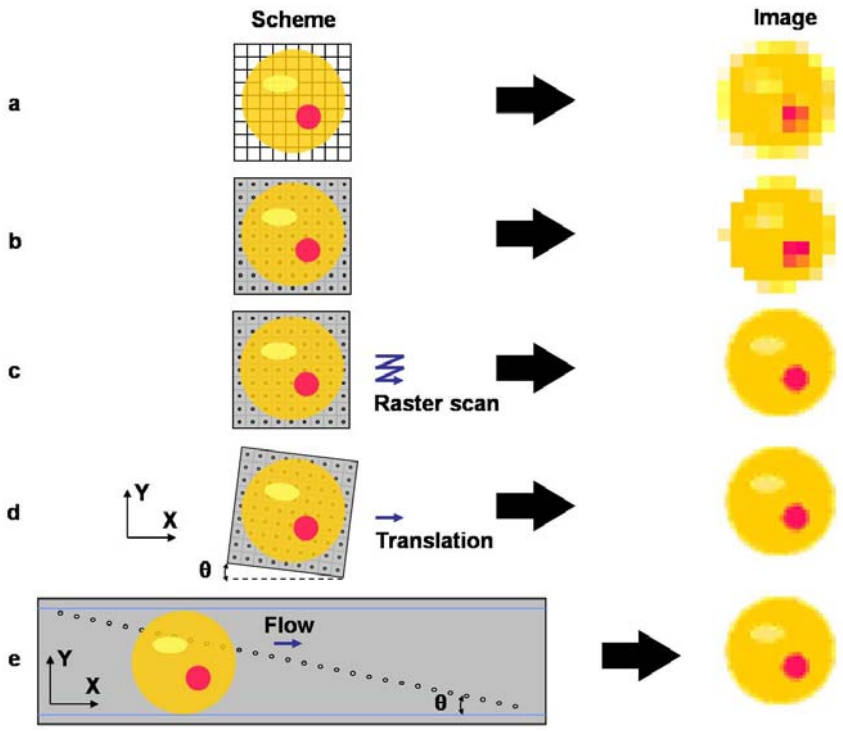

Figure 2-2 (color): Comparison of on-chip imaging schemes. (a) Direct projection imaging scheme. By placing the specimen directly on top of the sensor grid, we can obtain a projection image with resolution equal to the sensor pixel size. **(b)** By placing the specimen on a grid of apertures, we can obtain a sparse image. However, for the same grid density, the obtained image will not be much improved over that of scheme (a). **(c)** By raster-scanning the specimen over the aperture grid, we can obtain a 'filled-in' image. In this case, the image resolution is limited by the aperture size. Grid density is no longer a factor in resolution consideration. **(d)** The scanning scheme can be simplified into a single pass flow of the specimen across the grid by orientating the grid at a small angle (θ) with respect to the flow direction (X-axis). **(e)** The aperture grid can be simplified by substitution with a long linear aperture array. This scheme is the basis for the optofluidic microscopy method.

As an example, one can imagine covering a sensor grid with a thin metal layer and etching a small aperture onto the layer at the center of each sensor pixel. The sensor pixel will then be sensitive only to light transmitted through the aperture. By placing a target specimen on top of the grid, we can then obtain a sparsely sampled image of the object (Fig. 2-2 (b)). A 'filled-in' image can be generated by raster-scanning the specimen over the grid (or equivalently, raster-scanning the grid under the specimen) and compositing the time varying transmissions through the apertures appropriately (Fig. 2-2 (c)). We can see that in this case, the resolution is fundamentally determined by the aperture size and not the pixel size. Therefore, by choosing the appropriate aperture size we can achieve high resolution microscope imaging. The imaging strategy can be simplified by tilting the aperture grid at a small angle (θ) with respect to X-axis and replacing the raster-scan pattern with a single linear translation of the specimen across the grid (Fig. 2-2 (d)). As long as a sufficient number of apertures span the specimen completely in Y-axis, and neighboring apertures overlap sufficiently along Y-axis, a 'filled-in' high resolution image of the specimen will be achieved. The design can be further simplified by replacing the tilted 2D aperture grid with a long tilted 1D aperture array (Fig. 2-2 (e)). This imaging strategy [16] forms the basis of the OFM method. The OFM method shares many similarities with near field scanning optical microscopy methods [17]. In fact, the OFM aperture array can be interpreted as a series of NSOM apertures. Whereas NSOM sensors are generally raster-scanned over the target objects, the OFM approach uses object translation to accomplish scanning – in the microfluidic system, this is a far simpler and more efficient strategy.

More specifically, an OFM device utilizes a photosensor array (e.g., a CCD or CMOS image sensor) that is covered by a metal layer and has a line of small apertures (1 μm or less) milled through the metal layer. The apertures are spaced appropriately so that each maps uniquely onto the underlying sensor pixels (Fig. 2-3 (a)). A microfluidic channel is then aligned on top of the array in a diagonal fashion, and the system is uniformly illuminated from above. The metal layer blocks light from the underlying pixels; light can only be transmitted through the apertures. The imaging process involves uniformly flowing the specimen through the channel and recording the time varying light transmission through each aperture as the specimen passes (Fig. 2-3 (b)). Each time scan represents a line profile across the specimen. Since the specimen passes the apertures sequentially, there is a constant time delay between adjacent line scans if the speed of the specimen is uniform (Fig. 2-3 (c)). By shifting the line scans with this delay, we can obtain an accurate projection image of the specimen (Fig. 2-3 (d)).

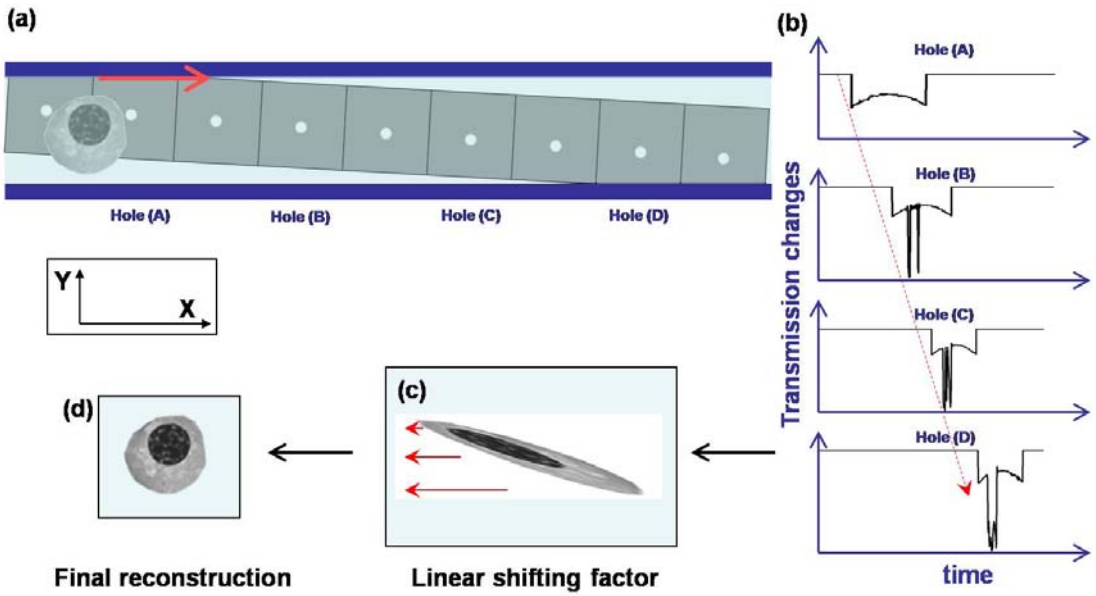

Figure 2-3 (color): The working principle of the OFM method. (a) The specimen flows across the slanted apertures array in the OFM device (top view). **(b)** The time traces recorded through the apertures in the OFM device. **(c)** Stacking the time traces together forms a skewed image with a linear shifting factor. **(d)** A high resolution image of the specimen can be easily reconstructed by correcting the shifting factor.

Unlike the physical sensing grid in a CCD or CMOS image sensor, the OFM sampling scheme effectively establishes a virtual sensing grid (see Chapter 3 for detailed discussion). The grid density is adjustable by changing the number of apertures spanning the channel, the flow speed of the specimen, and the OFM readout rate. Higher pixel density is helpful to oversample the specimen and prevent undesirable aliasing artifacts in the images. The ultimate resolution of such a system is limited by the aperture size. The

OFM method circumvents the resolution limitation imposed by the sensor pixel size in Lange's method.

The use of microfluidics also brings some advantages to OFM imaging. First, fluid is a natural environment for many biological specimens. This means there is less sample preparation necessary and less impact to the biological specimens for OFM imaging. Second, the format of microfluidic transportation can also potentially enable high-through microscope imaging via an OFM device, i.e., in a flow cytometer system [18]. Third, the micron-sized microfluidic channel can confine the specimen close to the aperture array in an OFM device, and ensure sharp and high-resolution OFM images. Last but not least, OFM and other microfluidic devices share similar fabrication processes. Therefore, OFM can be integrated as an imaging component in a larger lab-on-a-chip system, and serve for more complicated specimen analysis.

2.4 The first completely on-chip OFM device

2.4.1 Fabrication

The first completely on-chip OFM prototype device was fabricated on a commercially available 2D CMOS image sensor (Micron MT9V403C12STM) with 9.9 μm pixel size. We planarized the surface of the sensor with a 2 μm thick SU8 resin, and coated it with a 300 nm thick aluminium (Al) layer. We then milled two lines of apertures (1 μm diameter) separated by a single line of sensor pixels onto the Al layer with a focused ion beam (FIB) machine (FEI Company Nova 200). The apertures were spaced 9.9 μm apart so that each aperture mapped uniquely onto a single sensor pixel (Fig. 2-4 (a, b)). Each line consisted of 100 apertures. A 0.2 μm thick poly(methyl methacrylate) (PMMA) layer was spin-coated on top of the Al film to protect the OFM apertures. Finally we bonded an optically transparent poly(dimethylsiloxane) (PDMS) microfluidic chip containing a channel (width = 50 μm, height = 15 μm) on top of the sensor with a Karl Suss mask aligner (MA3). The channel was oriented at $\theta = 0.05$ radians with respect to the aperture arrays. The top of the system was uniformly illuminated with white light (~ 20 mW/cm^2, approximately the intensity of sunlight) from a halogen lamp.

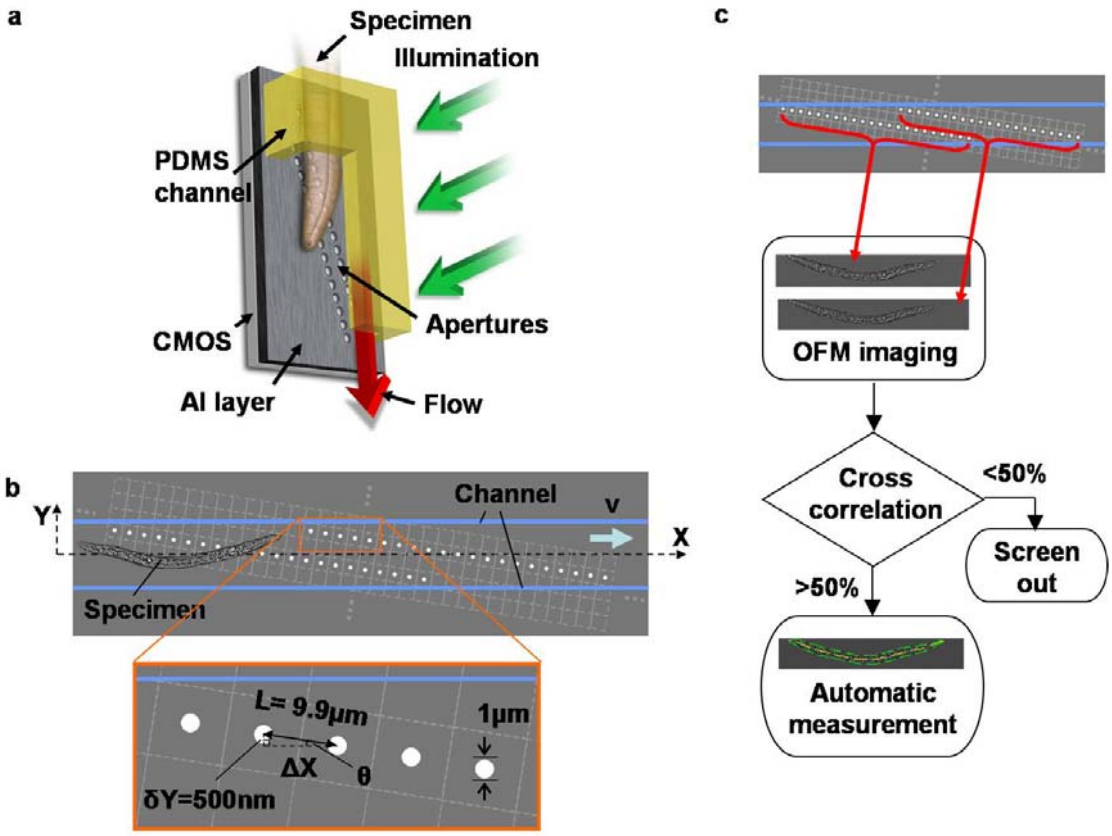

Figure 2-4 (color): The fabrication and operation of the first on-chip OFM prototype. (a) The first OFM prototype utilizes gravity to drive the specimen. **(b)** The schematic of the device (top view). The OFM apertures (white circles) are defined on the Al (gray) coated 2D CMOS image sensor (light gray dashed grid), and span the entire microfluidic channel (blue lines). **(c)** Flow diagram of the OFM operation. Two OFM images of the same *C. elegans* are acquired by the two OFM arrays respectively (red arrows). If the image correlation is less than 50%, the image pair is rejected. Otherwise, the area and the length of the worms are measured automatically by evaluating the contour (green dashed line), and the midline (yellow dashed line).

This on-chip OFM prototype (Fig. 2-4 (a, b)) utilizes two parallel OFM arrays for two reasons. First, by measuring the time difference between when the specimen first crosses each array and knowing the separation between the two arrays along the channel axis X, we can determine the flow speed of the specimen v, which is important for correct OFM image construction. (Note that the flow speed is determined for each specimen independently. As such, speed variations between specimens have no impact on our ability to perform correct OFM image reconstruction.) Second, significant differences between the two OFM images acquired by the two OFM arrays for the same specimen will indicate shape changes, flow speed variations, and/or rotations of the specimen during the data acquisition. As accurate OFM imaging requires the absence of these variations, discrepancy between the images is a possible criterion for rejecting that image pair (Fig. 2-4 (c)). We set our rejection criterion at the image-pair correlation threshold of less than 50%. During our experiment of *C. elegans* imaging and phenotype characterization (Section 2.5), approximately 50% of the specimens were rejected based on this criterion. We note that this processing approach was highly conservative as it also rejected a large proportion of acceptable images in which image-pair correlation was low due to small variations in flow speed and slight specimen shifts. We believe that better flow controls (such as smoother channels and better speed tracking) and better image processing algorithms can significantly lower the rejection rate. This is an area that is worth further study.

2.4.2 OFM imaging with a gravity driven microfluidic flow

OFM imaging relies on the steady movement of the specimen transported by the microfluidic flow. We have been developing several forms of on-chip microfluidic drive (see Section 2.6.2 for discussion) in order to eliminate the need for bulky external microfluidic pumps. In the first OFM prototype device, we used gravity driven microfluidic flow, where we operated the OFM prototype in an upright mode to utilize gravity to drive the specimen solution across the device (Fig. 2-4 (a)). We demonstrated the proper functioning of this on-chip microscope system by employing it to image *C. elegans* larvae.

To facilitate efficient flow of the specimens through the system, we took the following steps in preparing the microfluidic channel. The PDMS microfluidic channel was designed with a smooth funnel at each end, and oxygen plasma was used to render the inner surface of the PDMS channel hydrophilic. Prior to use, we conducted a surface treatment process to reduce specimen adhesion to the channel walls. The microfluidic channel was filled and flushed with a 10 % poly(ethylene glycol) (PEG) solution, 0.5mM NAIO4, and 0.5% (by weight) benzyl alcohol. Under the activation of UV light for 1 hour, the channel surface was conjugated with the PEG molecules. The process is similar to that in [19]. The PEG grafted surface prevented non-specific adsorption with biological entities and lubricated the object flow. The chip could then be rinsed with DI water, dried and stored under ambient condition since the PEG grafted surface has long-term stability. The PEG grafting process promoted the flow of specimens in OFM imaging.

During the OFM imaging process, the specimen solution (newly hatched *C. elegans* L1 larvae in S-basal buffer, ~ 20 worms/μL) was first injected into the top funnel. The solution wetted the channel and the specimens were continuously pulled into the channel by the gravity driven microfluidic flow. To prevent excessive motion of the worms, we immobilized them by subjecting them to a 70 ^{o}C heat bath for 3 min. Due to the sedimentation of the worms in the solution, the throughput of OFM imaging was not constant. The maximum observed throughput was about 5 worms/min. However, the flow speed of worms v in the channel was fairly uniform (~ 500 μm/sec). The data readout rate f of each OFM array was 1k frames/sec, and imaging of each worm required about 2.5 seconds. The spacing of the OFM virtual grid was 0.5 μm along both X and Y axes (less than the 1 μm aperture size).

2.4.3 Comparison of the image quality between OFM and conventional imaging techniques

Figure 2-5 (a) shows a pair of OFM images acquired by the two OFM arrays from the same wild-type *C. elegans*. The image correlation between them was 56%. Consistent internal structures were found in both OFM images. Fig. 2-5 (b) shows an image collected from a similar worm that was placed directly onto an unprocessed CMOS sensor (note that the pixel size is 9.9 μm); the worm was barely distinguishable in this low resolution direct projection image. Fig. 2-5 (c) shows a conventional microscope image of a similar worm acquired through a 20× Olympus objective lens (650 nm resolution for 555 nm wavelength under Sparrow's criterion). Similar internal structures of the *C. elegans* appeared in both the microscope and the OFM images. This confirmed

that OFM can render images comparable in quality to those of a conventional microscope with similar resolution.

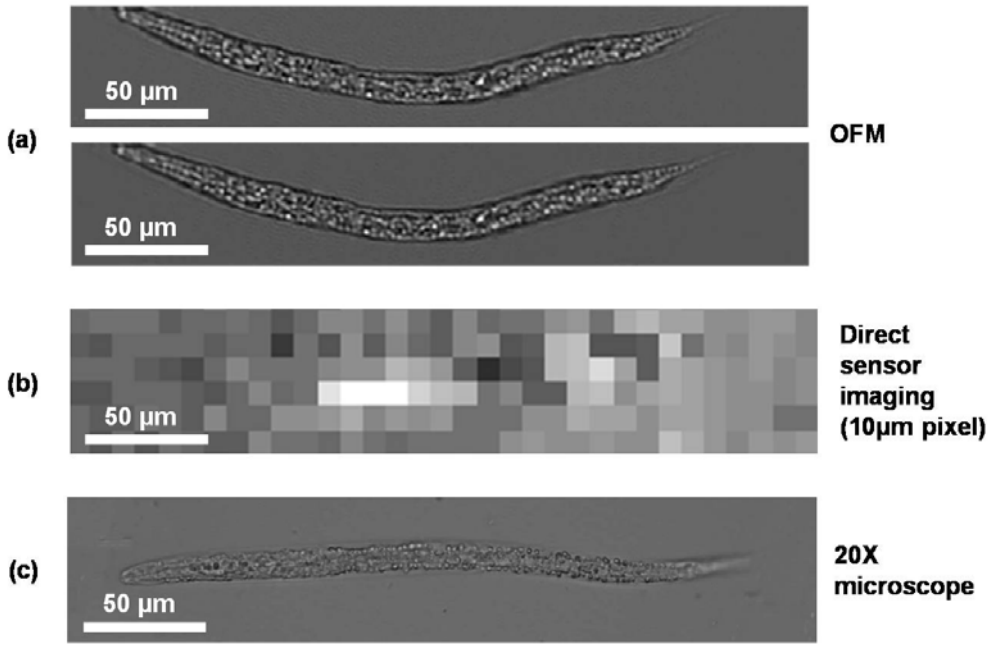

Figure 2-5: Images of wild-type *C. elegans* L1 larvae. **(a)** Duplicate OFM images acquired by the two OFM arrays for the same *C. elegans*. **(b)** Direct projection image on a CMOS sensor with 9.9 µm pixel size. **(c)** Conventional microscope image acquired with a 20× objective.

2.5 Automated microscopy and quantitative phenotype characterization of *Caenorhabditis elegans*

The function of a gene must manifest itself in a certain phenotype to be observed, but the formidable number of genes and their combinations imposes a difficult challenge to systematic phenotype characterization [20-21]. Inexpensive, automated, and quantitative phenotype characterization devices are critical to comprehensive biology studies. Motivated by the extensive use of phenotype characterization, especially morphology, in the genetic studies of microorganisms and cells, we used the OFM prototype to image and analyze phenotypes of *C. elegans*. The phenotypes/alleles used were *dpy-7(e88)*, *sma-3(e491),* and wild-type (N2). All *C. elegans* strains were cultured at 20° C. Bleaching was used to synchronize the development of *C. elegans* L1 larvae [22].

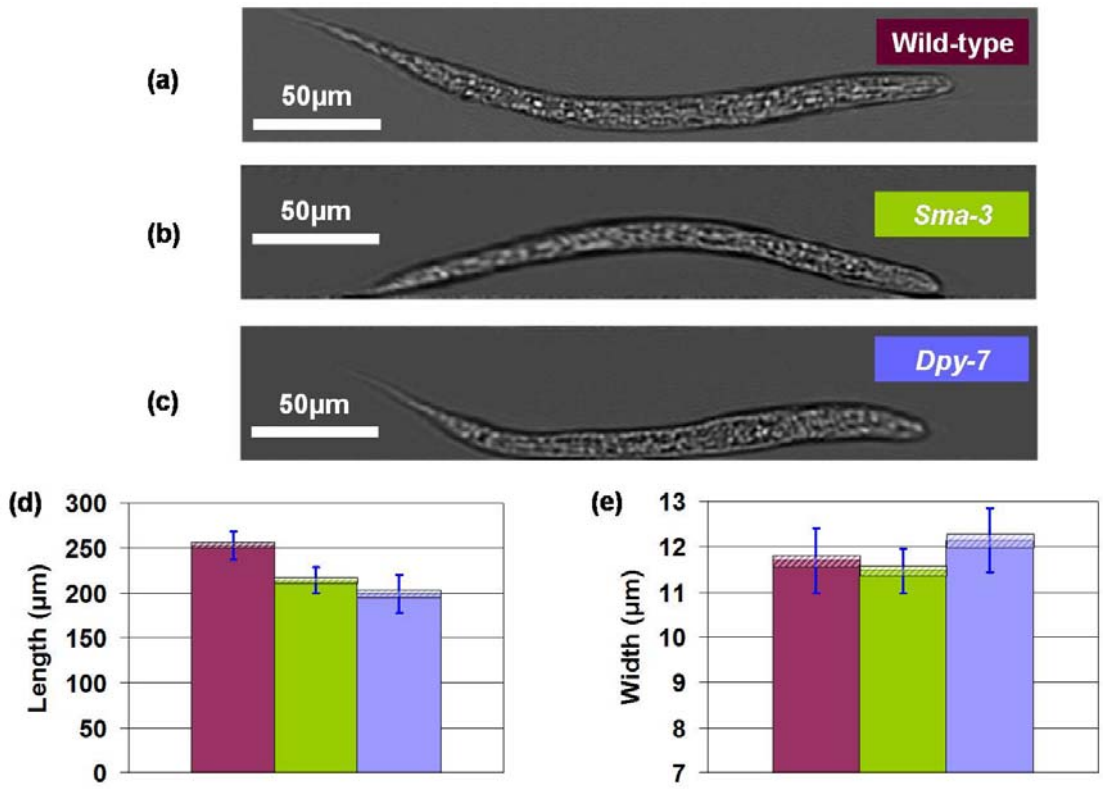

Figure 2-6 (color): Phenotype characterization of *C. elegans* L1 larvae. (a-c) Typical OFM images of wild-type, *sma-3*, and *dpy-7* worms, respectively. **(d, e)** The length (d) and effective width (e) of wild-type, *sma-3*, and *dpy-7*worms, respectively (color-coded). The columns represent the mean values in the population; the hatched areas correspond to the confidence intervals of the mean values; and the error bars are the standard deviations indicating the variation between individuals in the population. Twenty-five worms were evaluated for each phenotype.

To compare body sizes of the wild-type (N2), *sma-3* (e491) and *dpy-7 C. Elegans* (e88), we imaged 25 specimens of each strain. The *sma-3* (e491) gene is part of a family of transforming growth factor β pathway components [23]. The dpy-7 gene encodes a cuticular collagen required for proper body form [24]. The typical OFM images of the three strains (Fig. 2-6 (a-c)) show that the *sma-3* worm is smaller and thinner than the wild-type worm, and the *dpy-7* worm is wider and shorter than the wild-type worm. These observations are consistent with those made under a conventional microscope.

Since OFM images are, by its nature, digitalized, we can perform large volume and automatic quantitative information extraction by computer assisted post-processing. We developed a Matlab program to determine the area and length of the worms in batches (Fig. 2-4 (c)). We first delineated the boundary around each *C. elegans* from the OFM images, and then calculated the area occupied by each *C. elegans* based on the boundary. Next we segmented the *C. elegans* image along its length and calculated the centroid for each segment. Lastly, we connected the centroids by a continuous line. The length of the *C. elegans* is given by the length of this line. The width of the *C. elegans* is calculated by dividing the area occupied by the nematode with its length.

In Fig. 2-6 (d, e), the columns represent the mean length and width of the three *C. elegans* strains; the hatched areas correspond to the confidence intervals of our mean length and width estimates. The standard deviations (blue error bars) of the measurement indicate the variation between individuals within the strain. The measured mean length and width were 252.9 ± 3.1 μm and 11.7 ± 0.1 μm for wild-type, 214.3 ± 2.9μm and 11.5 ± 0.1 μm for *sma-3*, 199.1 ± 4.3 μm and 12.1 ± 0.1 μm for *dpy-7*. They were consistent with reported data [25]. The three strains have distinct length ($p<0.01$ for each

pair; Student t-test). *dpy*-7 mutants are significantly wider than N2 and *sma-3* ($p<0.05$ and $p<0.01$ respectively). However, we observed no statistically significant width difference in width between *sma-3* and N2 for the specimen size employed.

OFM enabled automated cell imaging is a particularly promising area. It can potentially be used in applications such as blood fraction analysis [26], urine screening for infection [27],[28], stem cell screening and sorting [29], [30], tumor cell counting [31],[32] and drug screening [33].

2.6 Discussion

We have introduced the concept of the OFM method, described the construction of the first completely on-chip OFM prototype device, and demonstrated its application in biology by automated and quantitative phenotype characterization of *C. elegans*. In this discussion session, we will look into some details about OFM imaging, e.g., the contrast mechanism, the stable microfluidic control of the specimen movement, and the impact of the OFM resolution by Brownian motion of the specimen in microfluidics.

2.6.1 Contrast mechanism

The contrast in OFM images shares similar origins with that in conventional microscopy images. OFM achieves its highest resolution in the plane that is just above the aperture array. In effect, OFM is similar to a conventional microscope in which the focal plane is locked at the plane that is just below the target object. The light field at that plane consists of the combination of the unscattered component of the illumination and the light

fields that are scattered by scattering sites (e.g., subcellular organelles) in the object. The presence of a scattering site immediately above a specific point in that plane will typically result in a dark patch in the image as the illumination light is scattered away by the scatterer. At other locations, the constructive interference of scattered light and the illumination field can result in a higher-than-average light field brightness. The dark boundary in Fig. 2-7 (e) can be attributed to a diminished light field from the presence of the pollen boundary scattering light away. The bright boundary is attributable to the constructive interference of that scattered light component with the illumination at those locations.

We note that the abovementioned similarity between OFM and a conventional microscope with a fixed focal plane holds only if near field components are insignificant. As OFM samples the wavefront without resorting to propagative projection, it is also sensitive to near field light components. Therefore, it is possible for an OFM system to achieve better resolution by using smaller apertures.

It is also worth noting that, similar to a conventional transmission microscope, there is, in principle, no upper limit on the specimen thickness that OFM can process. In practice, OFM will fail to acquire an image if the specimen is too optically scattering or absorptive to permit sufficient light to be transmitted through the OFM apertures. However, this practical limit exists for the conventional transmission microscope as well. Thus, this is not a relative disadvantage of OFM.

2.6.2 The stable on-chip microfluidic control of specimens in OFM

Stable motion control of the specimen in OFM devices is critical for the integrity of the OFM imaging process. Progressing from the first demonstration of the gravity driven microfluidic flow, we have been developing DC electrokinetic (DC-EK) and hydrodynamic focusing microfluidic drives to achieve stable and on-chip specimen actuations.

2.6.2.1 DC Electrokinetic (DC-EK)

A DC-EK driven OFM system was designed for imaging cells and other spherical/ellipsoidal objects. Pressure driven liquid flow in a microfluidic channel typically develops a parabolic velocity profile (Poiseulle flow) due to the non-slip boundary condition on the channel side walls. An object flowing in the channel will receive a torque from this non-uniform velocity profile and start to tumble if it is slightly off-center or if it is asymmetric (Fig. 2-7 (a)). This non-uniform translational movement can prevent the OFM system from acquiring an accurate image of the object.

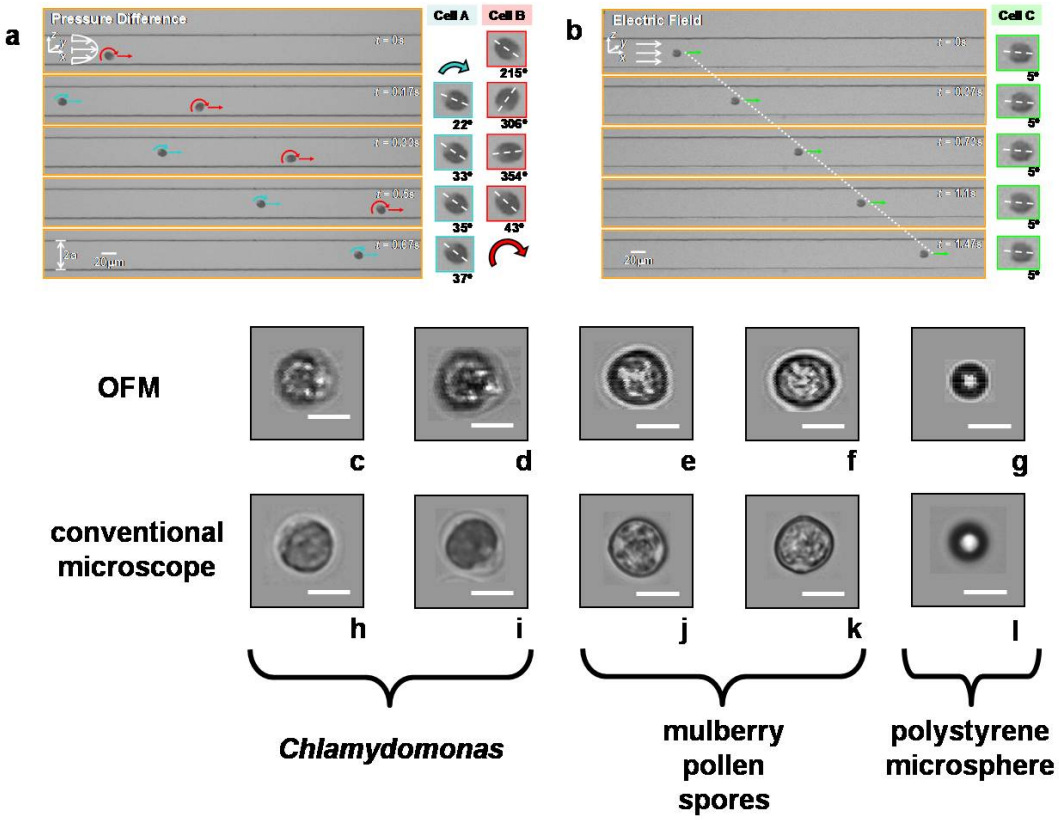

Figure 2-7 (color): DC-EK driven microfluidic flow and its application in OFM. (Courtesy of L. M. Lee) **(a)** The motion of cells in a pressure driven microfluidic flow. **(b)** The motion of cells in a DC-EK (E = 10 V/mm) microfluidic flow. **(c, d)** *Chlamydomonas* cell images taken from the on-chip OFM driven by DC-EK. **(h, i)** *Chlamydomonas* cell images from a conventional light transmission microscope with a 20 × objective. **(e, f)** Mulberry pollen spores images from OFM. **(h, k)** mulberry pollen spores image from the conventional microscope. **(g)** 10 μm polystyrene microsphere image from OFM. **(l)** 10 μm polystyrene microsphere image from a conventional microscope. (The white scale bar represents 10μm.)

DC-EK provides a simple and direct way to control the motion of biological cells in the on-chip OFM system to suppress object rotation (Fig. 2-7 (b)). By imposing a uniform electric field across the microfluidic channel in an OFM device, a dipole can be induced on the target ellipsoidal cell. The dispersed dipole moment can only be stabilized when its major axis is aligned along the electric field lines. In other words, the cell will experience an electro-orientation force [34]. At the same time, since the cell surface is likely to carry a net electrical charge, the external electric field will also exert an electrophoretic force on the cell [35]. This induces the cell to move along the channel down the electric gradient imposed. The velocity dependent viscous Stokes drag will eventually match this force and result in a constant rotation-free translational motion of the cell. The application of the external electric field also causes the translation of the electric double layer (EDL) at the channel walls; this phenomenon is known as electroosmosis [36]. Under the thin EDL assumption, the electroosmotic plug-like velocity profile will exert a symmetrical shear stress distribution on the cells. In steady-state situations, this movement is also non-rotational. At a constant voltage of 25 V to a pair of platinum electrodes at the channel inlet and outlet, we found that an average translational speed of 270 μm/s was achieved for the *Chlamydomonas* cells.

Several OFM images of *Chlamydomonas* cells (8 μm to 16 μm, from Carolina Scientific), mulberry pollen spores (11 μm to 16 μm, from Duke Scientific) and polystyrene microspheres (10 μm, from PolyScience) are shown respectively in Fig. 2-7 (c-g) in comparison with images acquired by an inverted microscope (Olympus IX-71) under a 20× objective in Fig. 2-7 (h-l).

2.6.2.2 Hydrodynamic focusing

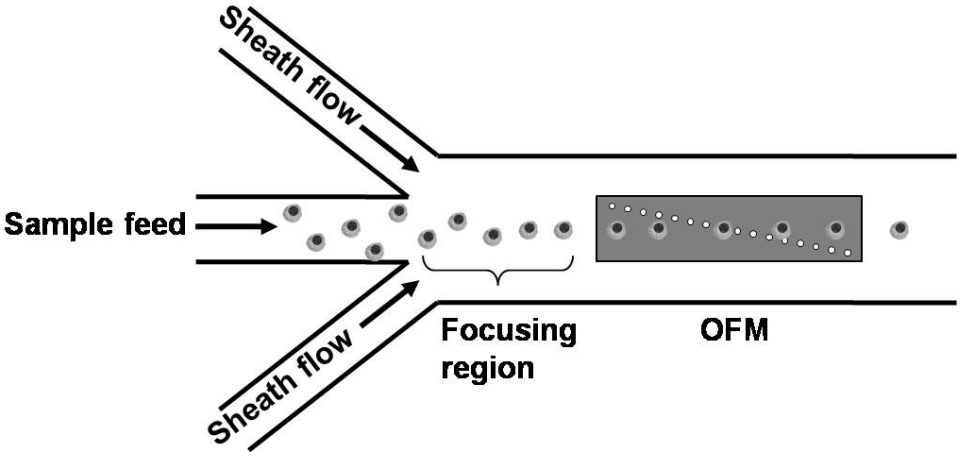

Figure 2-8: The application of hydrodynamic focusing in OFM. Hydrodynamic focusing utilizes side sheath flows to squeeze the specimen solution into a narrow stream and enable the steady movement control of spherical/elliptical cells in OFM.

Another way of avoiding the parabolic flow front and achieving stable movement control of the spherical/elliptical cells is to use hydrodynamic focusing. The microfluidic flow in an OFM device is almost always in the low Reynolds number regime, so cells follow the well-defined streamlines. Hydrodynamic focusing uses two side flows (sheath flows) to squeeze the specimen solution into a narrow tube of flow with a uniform velocity or a rectangular flow profile [37]. Therefore, cells in a hydrodynamic focused flow are less subject to rotation. We could place the OFM device at the downstream of the focused flow and achieve stable and high-throughput OFM imaging (Fig. 2-8).

2.6.3 Impact of Brownian motion on OFM resolution

Since the specimens in an OFM device are immersed in solution, the resolution of the OFM imaging will be influenced by the ubiquitous Brownian motion, but by how much? In this section, we will use Einstein's Brownian motion model to answer this question.

Brownian motion is the result of particles suspended in a liquid being bombarded across their surfaces by the liquid molecules. In Einstein's Brownian motion model, the magnitude of the displacement of the suspended particle from its initial position follows a Gaussian statistical distribution with a mean square displacement in one dimension given by:

$$\left|\Delta\bar{d}^{2}\right| = 2Dt\,, \tag{2-1}$$

where t is the observation time and D is the diffusion coefficient. For spherical particles in a liquid, this is given by

$$D = \frac{k_B T}{6\pi\eta r}\,, \tag{2-2}$$

where η is the viscosity of the medium, r is the radius of the particle, T is the temperature (in Kelvin), and k_B is the Boltzmann constant. The mean displacement for spherical particles is given by:

$$\left|d\right| = \sqrt{\frac{k_B T t}{3\pi r\eta}}\,. \tag{2-3}$$

If we consider the object for OFM imaging as a spherical object, we can use above equation to give an estimate of the impact of Brownian motion on OFM imaging.

For a *C. elegans* L1 wild-type larvae, k_B =1.3806503 × 10^{-23} m^2 kg s^{-2} K^{-1} , T= 293K (room temperature) , t=2.5 sec (total imaging time), η=8.90 × 10^{-4} kg·m^{-1}·s^{-1} (water), and r=30μm (radius of a sphere which has the similar surface area as a *C. elegans* L1 wild-type larvae , 10μm in width, 300μm in length). During the 2.5 seconds of OFM imaging, the mean displacement of the *C. elegans* due to the Brownian motion was $|d|$=0.2 μm, which is smaller than the ultimate resolution of the OFM prototype device 1 μm.

For *Chlamydomonas*, Mulberry Pollen Spores in EK OFM, we can consider a 15 μm sphere. Then k_B =1.3806503 × 10^{-23} m^2 kg s^{-2} K^{-1} , T= 293K (room temperature), t=0.3 sec (total imaging time), η=8.90 × 10^{-4} kg·m^{-1}·s^{-1} (water), and r=7.5μm. During the 0.3 second OFM imaging, the mean displacement of the object due to the Brownian motion was $|d|$=0.1 μm, which is smaller than the ultimate resolution of EK OFM prototype 0.5 μm.

Therefore, although the specimens in an OFM device do exibit Brownian motion, its magnitude is small compared to the ultimate resolution of our OFM devices, mostly due to the relatively short imaging time of OFM.

2.7 Conclusion

We have implemented the first completely on-chip OFM prototype device. It is compact, simple and lensless. The invention of OFM can significantly benefit a broad spectrum of biomedicine applications and bioscience research, and may also change the way we conduct cell-level imaging experiments. For example, the availability of tens or even hundreds of microscopes on a chip can allow automated and massively parallel imaging of large populations of cells or microorganisms. Being cost-effective enough to be disposable, an on-chip microscope system can also potentially provide low cross-contamination risk (by being cost-effective enough to be disposable) point-of-care analysis in a clinical setting. In a third world countries, a complete, low-cost and compact microscope system suitable for malaria diagnosis can be a boon for health workers who need to travel from village to village.

The OFM devices can also help facilitate the development of personal medicine or personal care. For example, recently we demonstrated that OFM devices can be used for imaging *Giardia lamblia* trophozoites and cysts, a disease-causing parasite species that is commonly found in poor-quality water sources [38]. Because the OFM devices are not bigger than the digital cameras in most of cell phones nowadays, it is possible to envision the emergence of personal diagnostic tools with the microscopic imaging capability.

Bibliography

1. A. Y. Fu, C. Spence, A. Scherer, F. H. Arnold, and S. R. Quake, "A microfabricated fluorescence-activated cell sorter," Nat. Biotechnol. **17**, 1109-1111 (1999).
2. Y. C. Tai, J. Xie, Q. He, J. Liu, and T. Lee, "Integrated micro/nano fluidics for mass-spectrometry protein analysis," International Journal of Nonlinear Sciences and Numerical Simulation **3**, 739-741 (2002).
3. J. Xie, Y. N. Miao, J. Shih, Q. He, J. Liu, Y. C. Tai, and T. D. Lee, "An electrochemical pumping system for on-chip gradient generation," Analytical Chemistry **76**, 3756-3763 (2004).
4. L. Licklider, X. Q. Wang, A. Desai, Y. C. Tai, and T. D. Lee, "A micromachined chip-based electrospray source for mass spectrometry," Analytical Chemistry **72**, 367-375 (2000).
5. M. Tokeshi, Y. Kikutani, A. Hibara, K. Sato, H. Hisamoto, and T. Kitamori, "Chemical processing on microchips for analysis, synthesis, and bioassay," Electrophoresis **24**, 3583-3594 (2003).
6. L. J. Jin, J. Ferrance, and J. P. Landers, "Miniaturized electrophoresis: An evolving role in laboratory medicine," Biotechniques **31**, 1332-+ (2001).
7. P. S. Doyle, J. Bibette, A. Bancaud, and J. L. Viovy, "Self-assembled magnetic matrices for DNA separation chips," Science **295**, 2237-2237 (2002).
8. D. Trau, T. M. H. Lee, A. I. K. Lao, R. Lenigk, I. M. Hsing, N. Y. Ip, M. C. Carles, and N. J. Sucher, "Genotyping on a complementary metal oxide semiconductor silicon polymerase chain reaction chip with integrated DNA microarray," Analytical Chemistry **74**, 3168-3173 (2002).
9. S. R. Liu, "A microfabricated hybrid device for DNA sequencing," Electrophoresis **24**, 3755-3761 (2003).
10. G. M. Whitesides, "The origins and the future of microfluidics," Nature **442**, 368-373 (2006).
11. J. El-Ali, P. K. Sorger, and K. F. Jensen, "Cells on chips," Nature **442**, 403-411 (2006).
12. J. Garcia-Sucerquia, W. B. Xu, S. K. Jericho, P. Klages, M. H. Jericho, and H. J. Kreuzer, "Digital in-line holographic microscopy," Applied Optics **45**, 836-850 (2006).
13. S. Seo, T. Su, D. Tseng, A. Erlinger, and A. Ozcan, "Lensfree holographic imaging for on-chip cytometry and diagnostics," Lab on a Chip **9**, 777-787 (2009).
14. D. Lange, C. W. Storment, C. A. Conley, and G. T. A. Kovacs, "A microfluidic shadow imaging system for the study of the nematode Caenorhabditis elegans in space," Sensors and Actuators B-Chemical **107**, 904-914 (2005).
15. A. Ozcan, and U. Demirci, "Ultra wide-field lens-free monitoring of cells on-chip," Lab on a Chip **8**, 98-106 (2008).
16. X. Heng, D. Erickson, L. R. Baugh, Z. Yaqoob, P. W. Sternberg, D. Psaltis, and C. H. Yang, "Optofluidic microscopy - a method for implementing a high resolution optical microscope on a chip," Lab on a Chip **6**, 1274-1276 (2006).

17. D. Courjon, *Near-field microscopy and near-field optics* (Imperial College Press, London, 2003).
18. S. Perfetto, P. Chattopadhyay, and M. Roederer, "Seventeen-colour flow cytometry: unravelling the immune system," Nature Reviews Immunology **4**, 648-655 (2004).
19. S. Hu, X. Ren, M. Backman, C. E. Sims, G. P. Li, and N. Allbritton, "Cross-linked coatings for electrophoretic separations in poly(dimethylsiloxane) microchannels," Electrophoresis **2003**, 3679-3688 (2003).
20. B. R. Bochner, "New technologies to assess genotype-phenotype relationships," Nature Reviews Genetics **4**, 309-314 (2003).
21. W. W. Zhong, and P. W. Sternberg, "Genome-wide prediction of C-elegans genetic interactions," Science **311**, 1481-1484 (2006).
22. J. E. Sulston, and J. A. Hodgkin, *The Nematode Caernorhabditis Elegans* (Cold Spring Harbor Laboratory Press, Cold Spring Harbor, NY, 1988).
23. C. Savage, P. Das, A. L. Finelli, S. R. Townsend, C. Y. Sun, S. E. Baird, and R. W. Padgett, "Caenorhabditis elegans genes sma2, sma-3, and sma-4 define a conserved family of transforming growth factor beta pathway components," Proceedings of the National Academy of Sciences of the United States of America **93**, 790-794 (1996).
24. J. S. Gilleard, J. D. Barry, and I. L. Johnstone, "cis regulatory requirements for hypodermal cell-specific expression of the Caenorhabditis elegans cuticle collagen gene dpy-7," Molecular and Cellular Biology **17**, 2301-2311 (1997).
25. C. Savage-Dunn, R. Tokarz, H. Wang, S. Cohen, C. Giannikas, and R. W. Padgett, "SMA-3 Smad has specific and critical functions in DBL-1/SMA-6 TGF beta-related signaling," Developmental Biology **223**, 70-76 (2000).
26. W. Cui, Y. Fan, W. Wu, F. Zhang, J. Y. Wang, and A. P. Ni, "Expression of lymphocytes and lymphocyte subsets in patients with severe acute respiratory syndrome," Clinical Infectious Diseases **37**, 857-859 (2003).
27. J. M. Marrazzo, C. L. White, B. Krekeler, C. L. Celum, W. E. Lafferty, W. E. Stamm, and H. H. Handsfield, "Community-based urine screening for Chlamydia trachomatis with a ligase chain reaction assay," Annals of Internal Medicine **127**, 796-& (1997).
28. K. C. Carroll, D. C. Hale, D. H. Vonboerum, G. C. Reich, L. T. Hamilton, and J. M. Matsen, "Laboratory evaluation of urinary-tract infections in an ambulatory clinic," American Journal of Clinical Pathology **101**, 100-103 (1994).
29. G. B. McCowage, K. L. Phillips, T. L. Gentry, S. Hull, J. Kurtzberg, E. Gilboa, and C. Smith, "Multiparameter-fluorescence activated cell sorting analysis of retroviral vector gene transfer into primitive umbilical cord blood cells," Experimental Hematology **26**, 288-298 (1998).
30. J. Buchstaller, L. Sommer, M. Bodmer, R. Hoffmann, U. Suter, and N. Mantei, "Efficient isolation and gene expression profiling of small numbers of neural crest stem cells and developing Schwann cells," Journal of Neuroscience **24**, 2357-2365 (2004).
31. T. Fujiwara, D. W. Cai, R. N. Georges, T. Mukhopadhyay, E. A. Grimm, and J. A. Roth, "Therapeutic effect of a retroviral wild-type P53 expression vector in an orthotopic lung-cancer model," Journal of the National Cancer Institute **86**, 1458-1462 (1994).

32. S. B. Fox, K. C. Gatter, R. Bicknell, J. J. Going, P. Stanton, T. G. Cooke, and A. L. Harris, "Replationship of endothelial-cell proliferation to tumor vascularity in human breast-cancer," Cancer Research **53**, 4161-4163 (1993).
33. Z. E. Perlman, M. D. Slack, Y. Feng, T. J. Mitchison, L. F. Wu, and S. J. Altschuler, "Multidimensional drug profiling by automated microscopy," Science **306**, 1194-1198 (2004).
34. M. P. Hughes, *Nanoelectromechanics in Engineering and Biology* (CRC Press, 2003).
35. P. D. Grossman, and J. C. Colburn, *Capilliary Electrophoresis* (Academic Press, 1992).
36. R. F. Probstein, *Physicochemical Hydrodynamics* (Wiley-Interscience, 2003).
37. C. Simonnet, and A. Groisman, "Two-dimensional hydrodynamic focusing in a simple microfluidic device," Applied Physics Letters **87**, 114104 (2005).
38. L. Lee, X. Cui, and C. Yang, "The application of on-chip optofluidic microscopy for imaging Giardia lamblia trophozoites and cysts," Biomedical Microdevices, 1-8.

Chapter 3: Imaging Model and Resolution Characterization of OFM

In Chapter 2, we gave an intuitive description for the OFM method. However, this does not sufficiently answer some basic questions about OFM imaging. For example, what is the resolution of OFM? How is the aperture size related to the resolution? How dense should we make the virtual sensing grid (effectively established by the OFM imaging) in order to achieve certain resolution? In this chapter, we will introduce a signal and system model to discuss OFM, and answer these questions.

First, we will revisit the virtual sensing grid picture of the OFM method, and compare it to the digital imaging scheme of a conventional image sensor. Then we will discuss the resolution of OFM imaging with a thought experiment, where we move a point light source across an OFM aperture at certain height and examine how the transmission signal measured at the underlying CMOS pixel changes correspondingly. After that, we will introduce the signal and system model for OFM. By looking at the model in both space/time and frequency domains, we can thoroughly understand the sampling, resolution and aliasing issues in OFM imaging. Next, we will describe how we characterized the resolution of OFM devices experimentally by both point spread function (PSF) measurement and the analysis of OFM images. Finally, we will conclude and discuss the possibility of engineering the PSF of OFM devices to achieve unique performance.

3.1 Revisiting the sampling scheme of OFM

As mentioned in Chapter 2, the OFM sampling scheme effectively establishes a virtual sensing grid. Here we will explain this idea in more detail.

Suppose we have an OFM device with a readout rate of f. The diameter of the apertures is d, the distance between neighboring apertures is L, and the tilt angle between the aperture array and the microfluidic channel is θ (Fig. 3-1). When the specimen flows across the aperture array at a speed of v, it is equivalent to the case where the specimen is instead fixed while the aperture array moves in the opposite direction. In this way, the trace of the aperture array forms a virtual sampling grid across the specimen. The density of the grid in the Y direction is controlled by the tilt angle, $\delta Y = L\sin\theta$ (L is usually set to the minimum possible value before worrying about the cross-talk between apertures, and 10 μm is the value used in the OFM prototype), and the density in the X direction is determined by the flowing speed of the specimen and/or the readout rate of the OFM, $\delta X = v / f$.

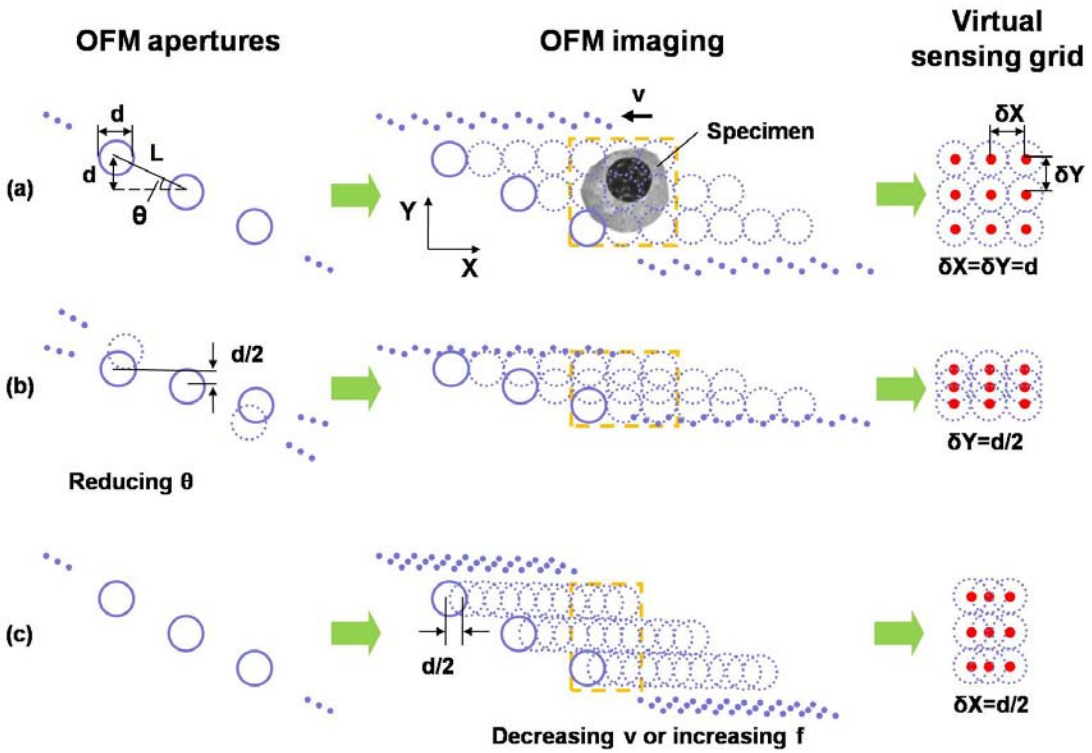

Figure 3-1 (color): Tunable virtual sensing grid of OFM. (a) When the tilt angle, the flow speed of the specimen, and the readout rate of OFM are appropriate, the virtual sensing grid formed by the OFM scheme is equivalent to that of a conventional solid-state image sensor $\delta X = \delta Y = d$. **(b)** By reducing the tilt angle θ, the spacing of the sensing grid in the *Y*-direction can be reduced, e.g. to half of the aperture size $\delta Y = d/2$. **(c)** By decreasing the flow speed of the specimen v or increasing the readout rate of OFM f, the spacing of the sensing grid in the *X*-direction can be reduced, e.g. to half of the aperture size $\delta X = d/2$.

When $\delta X = \delta Y = d$ (Fig. 3-1 (a)), the sampling grid formed by the OFM scheme is exactly equivalent to the sampling configuration in a conventional solid-state image sensor (In CMOS or CCD sensors, the minimum spacing between two neighboring sampling points is the physical size of a pixel). But unlike a conventional image sensor, the density of the virtual sensing grid established by the OFM imaging scheme can be further increased. For example, when we reduce the tilt angle θ, the spacing δY between two neighboring OFM apertures in the Y-direction becomes smaller (Fig. 3-1 (b)); when we decrease the flow speed v of the specimen or increase the readout rate of OFM f, the spacing δX between two sequential recording points becomes closer (Fig. 3-1 (c)). Similarly, an increase of the sampling density in both directions at the same time can also be achieved.

Although the OFM device samples the projection of the specimen temporally by each OFM aperture in the X direction and spatially by different OFM apertures in the Y direction, the image sampling schemes in these two directions are essentially equivalent to each other. Therefore, for the sake of simplicity we will use the temporal scanning of one OFM aperture as an example to discuss OFM imaging; the same conclusion can be drawn for the spatial OFM sampling in a similar way.

3.2 Resolution of OFM imaging

How do we test the resolution of a microscope system? The most common way method employed is the point spread function (PSF) measurement.

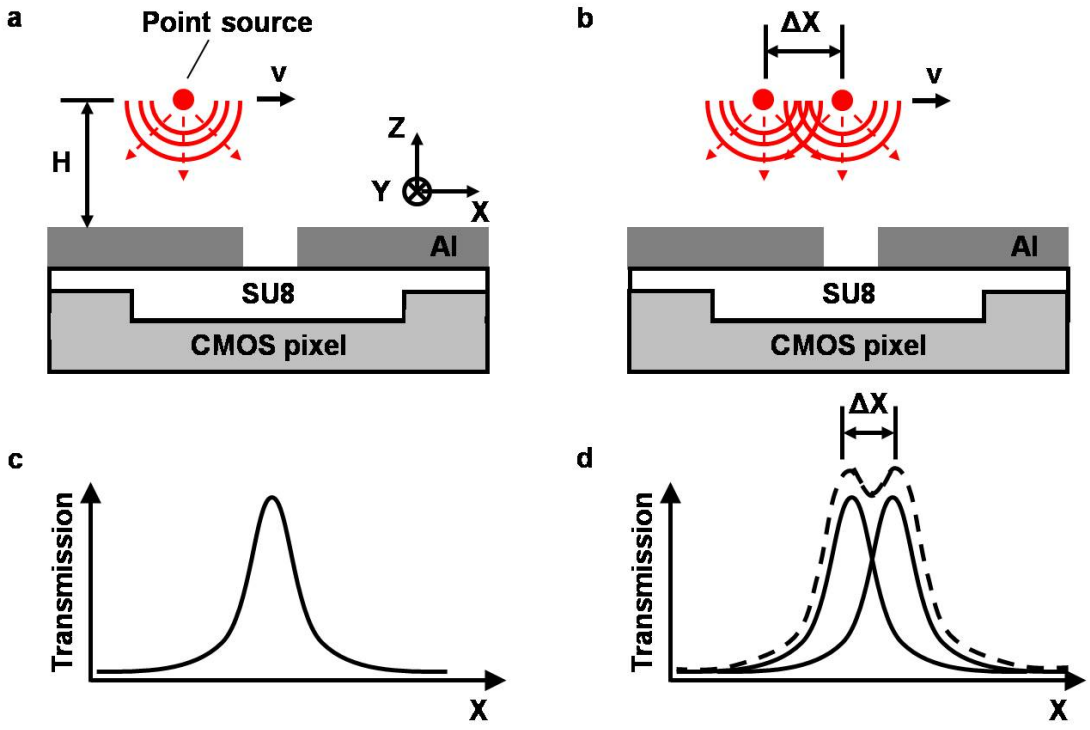

Figure 3-2 (color): Point spread function (PSF) and resolution of OFM. (a) Scan a point source across one of the OFM apertures at height *H*, and record the transmission signal with the underlying CMOS pixel. **(b)** Scan two point sources with spacing *ΔX* across one of the OFM apertures at height *H*, and record the transmission signal with the underlying CMOS pixel. **(c)** The transmission signal of a single scanning point source is the PSF of OFM. **(d)** The minimum distance between two resolvable scanning point sources defines the resolution of OFM.

First, we move a point source across an OFM aperture in the X direction at certain height, H (Fig. 3-2 (a)). If we record the transmission signal collected by the underlying CMOS pixel, we will have a Gaussian-like curve (Fig. 3-2 (c)).

If we move two equally bright incoherent point sources spaced by ΔX across the same OFM aperture at the same height, H (Fig. 3-2 (b)), the transmission signal collected by the CMOS pixel is simply the superposition of two above-mentioned Gaussian-like curves, and the distance between these two curves is ΔX (Fig. 3-2 (d)). When ΔX is much larger than the spread of the Gaussian-like curve, we will see two distinct bumps on the recorded transmission signal, so that we can tell there are two point sources. If these two point sources are two scattering sites of the specimen in the OFM device, we can resolve them from the OFM data. When ΔX is smaller than the spread of the Gaussian-like curve, the two bumps on the recorded transmission signal will merge into one, and we will not be able to tell whether it is formed by two closely-packed point sources or just one point source. If these two point sources are two scattering sites in the specimen, we will not be able to resolve them with the OFM device.

The spread of the recorded transmission signal with the presence of one point source at certain height H characterizes the resolution of OFM at this height. However, because there are several resolution criteria that determine the smallest ΔX before we lose the ability to resolve the two point sources [1], the exact value of the OFM resolution depends on the criterion we choose. In Section 3.4.1, we will be using the Sparrow criterion to define the resolution of OFM experimentally, because it is not tightly related to the exact shape of the transmission signal.

We also notice that the OFM resolution changes with the distance (H) from the object to the OFM aperture. More specifically, when we decrease the height of the point source, the transmission signal becomes narrower in the X direction. This means that when we have two point sources at this height, they can be resolved from the transmission signal at closer spacing (ΔX) compared to that at a higher position.

There is a limit, however, for such improvement on OFM resolution. In the extreme case, if we bring the point source all the way to the surface of the OFM aperture, the transmission signal will give us the exact transmission profile of the aperture, which is large within the aperture diameter range and zero outside of it. If we have two point sources inside the aperture diameter range, we will be unable to distinguish them by the transmission signal regardless of their separation. In other words, the ultimate resolution of OFM is limited by the size of apertures.

Based on the above discussion, we can conclude that the actual resolution of OFM is related to both the size of apertures and the height of the object from the aperture.

3.3 Signal and system model of OFM imaging

In the previous thought experiment, we were actually testing the impulse response of the OFM imaging system from the *signal and system* point of view. Here we will complete the construction of the whole model for OFM imaging, and use it to discuss the resolution, sampling and aliasing issues of OFM imaging.

As discussed in the previous section (Section 3.2), the OFM imaging system is a linear system. Therefore, we can decompose the object in an OFM device into many point sources, and the final OFM image will be the summation of the impulse responses of the OFM imaging system to each of these point sources. For clarity, we model the OFM imaging device as a three-stage system, including image collection, digital sampling and reconstruction filtering.

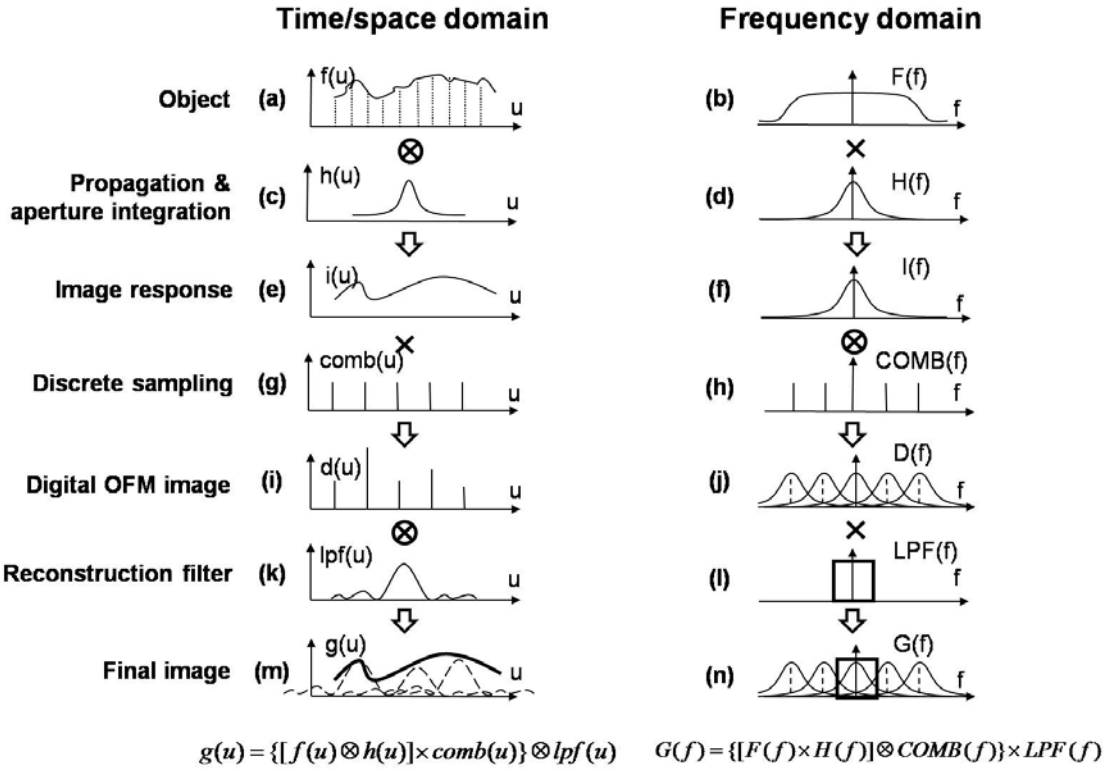

Figure 3-3: Signal and system model of the whole OFM imaging process. OFM imaging includes three stages: image collection, digital sampling, and reconstruction filtering. In the time/space domain, the object function **(a)** is first convolved with the PSF of OFM **(c)** to form a smoothed and continuous image response **(e).** Then the image response is multiplied by the discrete comb sampling function **(g)** to form the digital OFM image **(i).** At last, the digital OFM image will be convolved with the reconstruction filter function **(k)** to form the final OFM image **(m)** for display. In the frequency domain, the object spectrum **(b)** is first multiplied by the transfer function of OFM **(d)** to form the image spectrum **(f)** with narrow bandwidth. Then the image spectrum will be convolved with the comb sampling function **(h)** to form the digital OFM image spectrum **(j).** At last, the digital OFM image spectrum has to be filtered by an ideal low pass filter (LPF) **(l)** to control the aliasing errors in the final OFM image spectrum **(n).**

3.3.1 Image collection

For the image collection stage, let us picture an object in an OFM device that is composed of incoherent point sources (Fig. 3-3 (a)). Because of the free space propagation of these point sources, the projection image of the object on the OFM aperture plane is a blurred version of the object. The OFM apertures will then scan across the projection image and collect data by integrating a portion of the projection image over the aperture opening area. The entire effect *i(u)* of these two above processes (Fig. 3-3 (e)) is nothing but the convolution of the object function *f(u)* with the PSF of OFM *h(u)* (Fig. 3-3(c)). *u* is the sampling dimension, which could be either time in the *X* direction or space in the *Y* direction of the OFM imaging scheme (see Section 3.1 for the definition of the coordinate system). In the frequency domain, the object spectrum *F(f)* usually contains a wide bandwidth of information (Fig. 3-3 (b)), but the image collection process acts as a low-pass filter *H(f)* (Fig. 3-3 (d)) and limits the bandwidth of the final collected image *I(f)* (Fig. 3-3 (f)). Therefore, the PSF of OFM limits the information content in an OFM image, and determines the resolution of OFM imaging.

3.3.2 Sampling and aliasing

Image collection is only the first part of the OFM imaging process. An appropriate sampling strategy must be employed to use discrete sampling points to contain all information in the continuous image function *i(u)*. How dense should we sample the OFM image? This is a classical digital sampling problem, and has been summarized in Fig. 3-3 (e-j). Because the PSF of OFM *h(u)* is a Gaussian function (see Section 3.4.1),

the transfer function of OFM *H(f)* is a Gaussian function as well. When the bandwidth of the object spectrum *F(f)* is much wider than *H(f)*, the spectrum of the OFM image *I(f)* will be very similar to *H(f)*. In the frequency domain, the sampling process is the convolution of the spectrum of the continuous image *I(f)* and the sampling comb function *COMB(f)*. The spacing between neighboring impulses of *COMB(f)* is equal to the sampling rate $f_{sampling}$. Since the bandwidth of the Gaussian transfer function of OFM *H(f)* is unlimited, the higher the sampling rate $f_{sampling,}$ the less spectrum overlap between neighboring harmonics (Fig. 3-3 (j)), i.e. the less aliasing artifact in the OFM images. Thus, denser sampling is always desirable, but it means we have to increase the number of OFM apertures, the readout rate and the amount of computer resources, e.g. memory and computing time, for reconstructing the OFM images in the OFM device. If we can tolerate certain level of aliasing errors, we can choose a less demanding sampling rate, $f_{sampling,}$. Figure 3-4 illustrates the point.

The red circles in Fig. 3-4 (a) are the Gaussian harmonics in the 2D spectrum of an OFM image (the influence of other harmonics can be neglected); the spacing between neighboring harmonics is determined by the sampling rate of OFM. Even after applying the reconstruction filter (see Section 3.3.3), the spectrum of the OFM image (in blue box) will still mix with some component from the neighboring harmonics. Figure 3-4 (b) illustrates how the aliasing error changes with respect to the sampling rate of OFM imaging. We used doubled sampling ($f_{sampling} = 2/d$, where d is the aperture size of OFM) in our prototype device. It guarantees that the aliasing artifact in our OFM image is less than 0.4% no matter what specimen is imaged by the device.

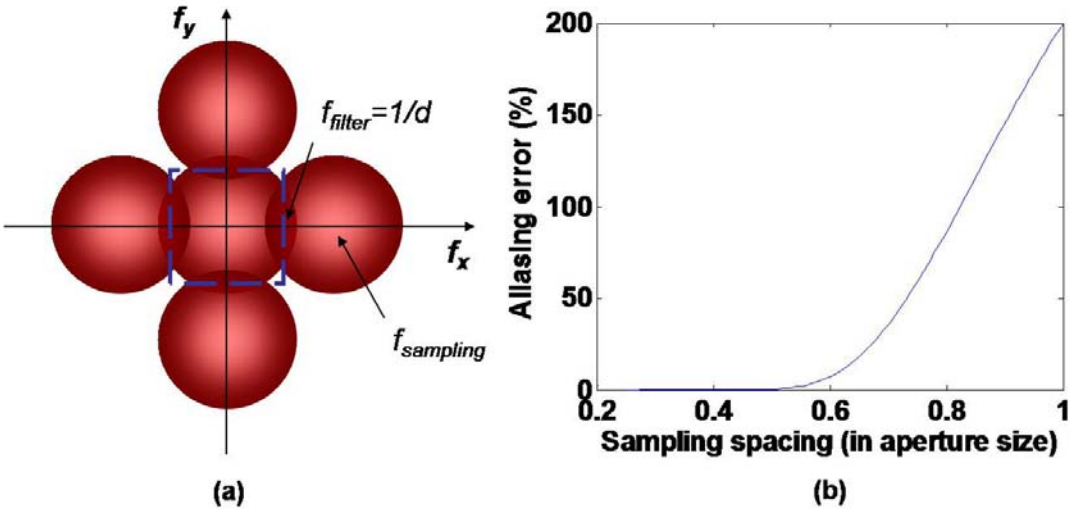

Figure 3-4 (color): OFM sampling rate and aliasing error. (a) Because of the discrete sampling, the overlapping between neighboring harmonics in the spectrum of digital OFM images can cause aliasing errors. **(b)** By increasing the sampling rate, the aliasing error can be controlled to a certain level.

If there are not many features on the object, the frequency spectrum of the OFM might be limited to certain bandwidth f_H. According to the Nyquist sampling theorem, we only need sampling rate of $f_{sampling}=2\,f_H$ to contain all information in the OFM image.

3.3.3 Reconstruction

Once we have the appropriately sampled discrete OFM image data, we can pass them through a low-pass filter (*LPF(f)*) to reconstruct the OFM image (Fig. 3-3 (i-n)). This low-pass filter might include a designed digital filter ($f_{filter}=1/d$ in our OFM prototype

device) and/or our eyes (e.g. our eye are nature smoothing filters, which is why a pixelated image on a computer screen look smooth to us).

We have seen that the resolution of OFM is determined by its PSF. If we engineer the PSF appropriately, we might be able to improve the performance of OFM. On the other hand, we also need to be careful about the sampling of OFM imaging to avoid severe aliasing errors and to ensure the fidelity of OFM images.

3.4 Experimental resolution characterization

3.4.1 Point spread function (PSF) measurement

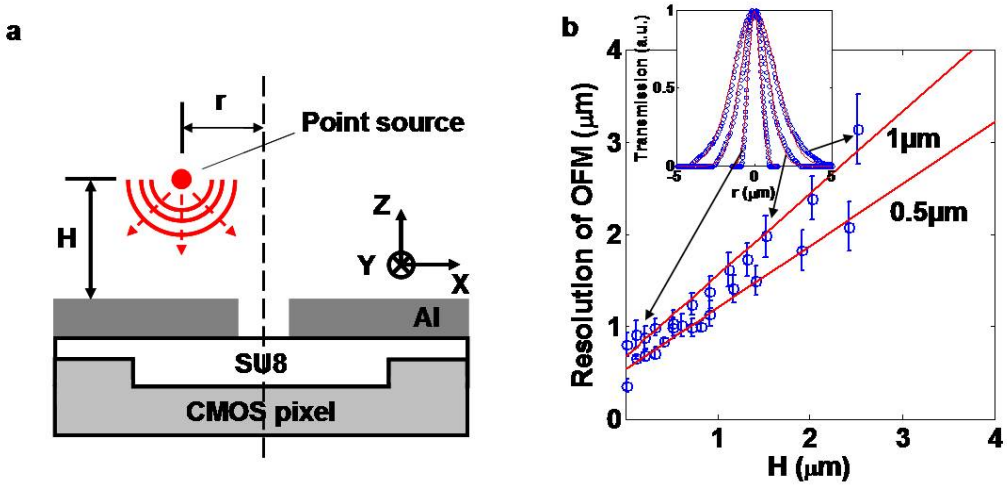

Figure 3-5 (color): Experimental resolution characterization of the OFM prototype. **(a)** Schematic of the point spread function (PSF) measurement. **(b)** The resolution of the prototype at various heights *H* above a 1 μm and 0.5 μm diameter aperture under the Sparrow's criterion. The inset shows representative OFM PSF plots for the 1 μm diameter aperture at *H* = 0.1 μm, 1.5 μm and 2.5 μm.

As discussed in previous sections, the resolution of OFM is determined by its PSF. Here we will describe an experiment in which we measured the PSF of OFM.

We measured the PSF of our prototypes by laterally scanning a near field scanning optical microscope (NSOM) (Alpha-SNOM, WITec Gmbh) tip across one of the OFM apertures (1 μm and 0.5 μm in diameter) at various heights *H* and measuring the signal detected by the underlying pixel (Fig. 3-5 (a)). We approximated the NSOM tip, which was less than 100 nm in diameter, as a point source. The inset of Fig. 3-5 (b) shows representative OFM PSF plots at H = 0.1 μm, 1.5 μm and 2.5 μm for the 1 μm diameter aperture. The PSF broadened as a function of *H*. We quantified the height dependent resolution of our prototype by the width of the PSF. Figure 3-5 (b) shows the resolution (Sparrow's criterion) [2] as a function of *H*. From the plot, we can see that the ultimate resolution of the OFM device with 1 μm apertures was 0.9 μm (with the 0.2μm thick layer of PMMA above the metal layer accounted for) and the resolution degraded to 3 μm at H = 2.5 μm. The ultimate resolution of the OFM device with 0.5 μm apertures was 0.8 μm (with the 0.4 μm thick layer of PMMA above the metal layer accounted for) and the resolution degraded to 2 μm at H = 2.5 μm. The result was consistent with our more detailed study on the light collection characteristics of small apertures [3].

However, the slopes of the two curves in Fig. 3-5 (b) are surprising. It seems that the resolution of the OFM device with 1 μm apertures degrades faster than that of the OFM device with 0.5 μm apertures. We will give our explanation and present our thoughts on this finding in the discussion (Section 3.5) of this chapter.

We note that, given the contrast mechanism of OFM, a better approach for resolution characterization would be to translate a point scatterer across the aperture

under a uniform illumination field and measure the light collected by the aperture. However, we further note that the point source and point scatterer configurations are optically similar in the context of resolution considerations. Under Sparrow's criterion [2] and in the small scatterer limit, the point source resolution computation is directly translatable for point scatter consideration.

3.4.2 OFM image analysis

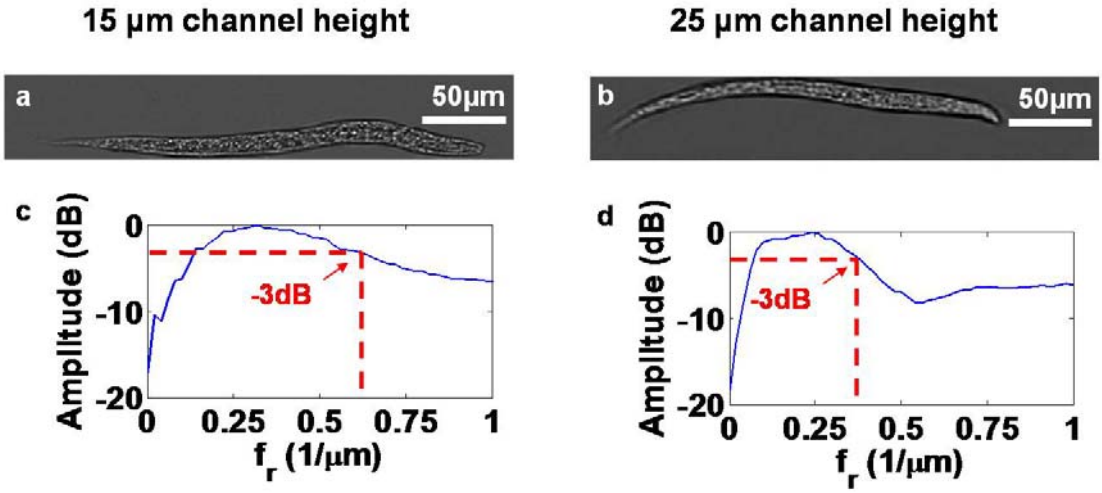

Figure 3-6 (color): Resolution analysis of OFM images. (a, b) OFM images of wild-type *C. elegans* L1 larvae in a 15 µm and a 25 µm tall microfluidic channel respectively. **(c, d)** The radial frequency spectra of OFM images in c and d respectively. The -3 dB bandwidths (dashed red lines) are at 0.62 μm^{-1} and 0.38 μm^{-1} respectively.

We also verified the resolution of OFM and its degradation with height through a *C. elegans* imaging experiment in which we varied the channel height. Figure 3-6 (a, b)

show OFM images of wild-type *C. elegans* in 15 μm and 25 μm tall channels respectively. A shallow channel was able to better confine the specimen close to the aperture array and thus was able to provide better resolved images (Fig. 3-6 (a)). Figure 3-6 (c, d) show the radial frequency spectrums of the OFM images, which revealed that the -3 dB bandwidths were at 0.62 μm^{-1} and 0.38 μm^{-1} respectively for the 15 μm and 25 μm channels. It means shallow microfluidic channels generate sharper OFM images and record OFM images with higher spatial resolution than the tall channels.

3.5 Discussion

3.5.1 Engineering the point spread function (PSF)

The result in Fig. 3-5 (b) seems counter-intuitive, because it shows that the resolution of the OFM device with 1 μm apertures degrades faster than that of the OFM device with 0.5 μm apertures. As we know, when we illuminate an aperture, small apertures are supposed to diffract light more severely than the larger apertures do (Fig. 3-7 (a)). However, the result actually does not contradict the common wisdom because OFM devices use apertures not to emit but to receive light instead (Fig. 3-7 (b)). We are currently performing a research to verify the result and to find out the answer of the mystery.

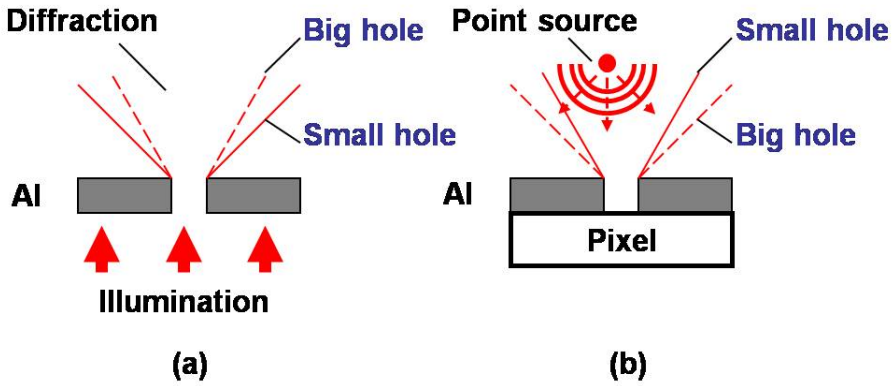

Figure 3-7 (color): Depth of field in illumination and collection mode OFM. (a) Bigger hole will give longer depth of field for illumination mode OFMs. **(b)** Our PSF measurement suggests that smaller hole could give longer depth of field for collection mode OFMs.

Our cursory explanation is as follows. Like in waveguides, small apertures support a smaller number of modes than larger apertures. Therefore, only light within a limited angular range will be accepted by the small apertures. In other words, the small apertures have narrower viewing angle and can resolve two point sources packed at closer distance than the big apertures. This means that OFM devices with small apertures have a longer depth of field than OFM devices with larger apertures. Thus, we can engineer the PSF of OFM by using different apertures!

This observation provided us insights that inspired us a whole line of research in our group, where we attempted to implement new functionality by modifying the OFM apertures. For example, if we punch four closely packed holes to be used as a single OFM aperture, these holes will form an on-chip phase imager based on 2D generalized Young's interference (see Chapter 4). This will allow us to build a phase sensitive OFM

device. If we engrave a set of concentric rings around a subwavelength hole on a gold film with proper parameters, the surface Plasmon generated by the rings can interfere destructively with and suppress the direct transmission (-27dB) through the hole [4]. This will allow us to build a dark-field OFM device. If we instead used a C-shaped aperture instead, the transmission could potentially be 3 orders of magnitude higher [5]. This would be very useful as we are trying to increase the resolution of OFM or reduce the amount of light illuminated onto the specimen. We also can texturize the metal surface around the OFM aperture to achieve angular, spectral and polarimetric selectivity [6-7].

3.5.2 Deconvolution OFM

We can measure and engineer the PSF of OFM, so we should also be able to remove the PSF numerically. Deconvolution has been increasingly adopted for improving the contrast and resolution of digital images captured by the microscope [8]. Because the cell-level specimens in OFM devices are weakly scattering objects, their OFM image can be sharpen by removing the blurring of the PSF caused by the free-space propagation. This deconvolution calculation is the reverse process of OFM image collection (Fig. 3-3 (a, c, and e)). Furthermore, with the additional phase information detected by phase sensitive OFM (see Chapter 4), we anticipate that better “deconvolution” effect can be achieved.

3.6 Conclusion

We have established the signal and system model for OFM, discussed the fundamental aspects of the resolution, sampling and aliasing issues in the OFM imaging, and characterized the 3D PSF of OFM experimentally. It is important to attempt to understand the underlying process for a new imaging system. It not only provides us a guideline to further improve the performance of the system, but may also reveal a new arena for us to explore, e.g. engineering the PSF of OFM by structuring the OFM apertures.

Bibliography

1. A. Den Dekker, and A. Van den Bos, "Resolution: a survey," Journal of the Optical Society of America A **14**, 547-557 (1997).
2. A. W. Jones, and J. Bland-Hawthorn, "Towards a General Definition for Spectroscopic Resolution. ," ASP Conference Series **77** (1995).
3. X. Heng, X. Q. Cui, D. W. Knapp, J. G. Wu, Z. Yaqoob, E. J. McDowell, D. Psaltis, and C. H. Yang, "Characterization of light collection through a subwavelength aperture from a point source," Optics Express **14**, 10410-10425 (2006).
4. Guoan Zheng, Xiquan Cui, Meng Cui, and C. Yang, "Surface-plasmon-enabled darkfield aperture: a method for suppressing background during weak signal detections," Submitted (2009).
5. X. Shi, L. Hesselink, and R. Thornton, "Ultrahigh light transmission through a C-shaped nanoaperture," Optics Letters **28**, 1320-1322 (2003).
6. H. Lezec, A. Degiron, E. Devaux, R. Linke, L. Martin-Moreno, F. Garcia-Vidal, and T. Ebbesen, "Beaming light from a subwavelength aperture," (2002), pp. 820-822.
7. E. Laux, C. Genet, T. Skauli, and T. Ebbesen, "Plasmonic photon sorters for spectral and polarimetric imaging," Nature Photonics **2**, 161-164 (2008).
8. http://micro.magnet.fsu.edu/primer/digitalimaging/deconvolution/deconintro.html.

Chapter 4: Differential Interference Contrast OFM (DIC-OFM)

Progressing from our first completely on-chip OFM device, we are attempting to create a family of OFM devices with a variety of functionalities. In this chapter, we will introduce differential interference contrast OFM (DIC-OFM) device. It makes use of a novel Young's-interference-like compact phase detection scheme, and images otherwise transparent cell-level biological specimens in an OFM device.

We will first start by motivating why phase imaging is important. Subsequently, we will review the conventional phase microscopy methods. Because the conventional methods require bulky and complicated optical components, we will then introduce a new on-chip phase imager, the structured aperture interference (SAI) wavefront sensor, for implementing the DIC-OFM. After that, we will present two proof-of-concept experiments to demonstrate its feasibility. Finally, we will discuss strategies for implementing a complete on-chip DIC-OFM device, as well as the potential to numerically change the focal plane in an OFM device.

4.1 Background

4.1.1 Amplitude/Intensity and phase imaging

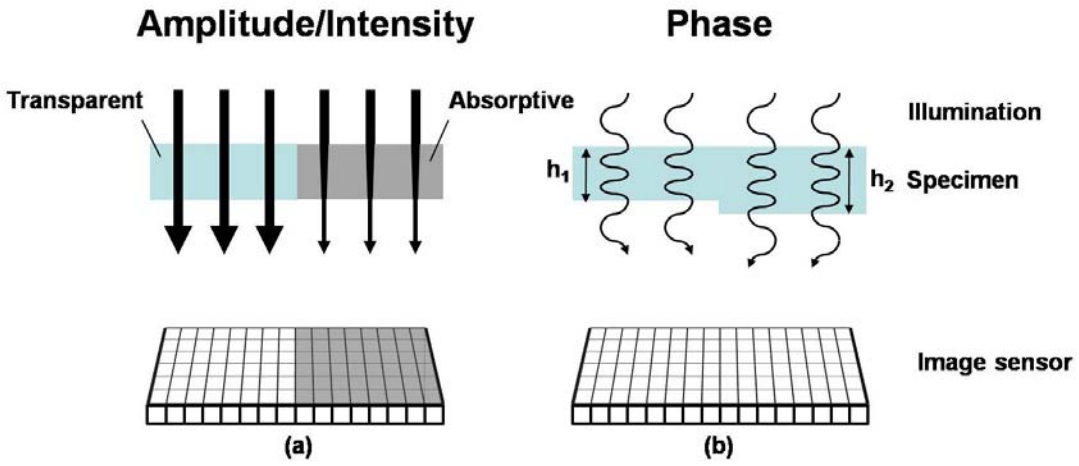

Figure 4-1 (color): Amplitude/Intensity and phase imaging. (a) Amplitude/Intensity contrast can be easily measured by most image sensors. **(b)** Phase contrast, representing the optical thickness of the specimen, is harder to detect.

An optical microscope image contains two major types of image information: light amplitude/intensity and phase spatial distribution. They are both important, but the phase information is much harder to detect than the amplitude/intensity information. For example, let us consider a simple optical experiment to image a piece of material, where we illuminate the material from the top and use an image sensor to record the strength of the light transmission at the bottom. If the left part of the material is transparent and the right part is absorptive (Fig. 4-1 (a)), we can immediately see the contrast of the specimen from the light intensity (the square of light amplitude) signal at the image

sensor. In contrast, if the left and right sides of the material are both transparent but have different thicknesses (Fig. 4-1 (b)), we will not be able to see any contrast (except at the edge) on the image sensor. This is because our commonly used image sensor cannot differentiate between the light that travels a longer distance through the right side of the material than through the left side (the phases of the light are different).

While the amplitude image information is readily extractable by our eyes or a CCD camera, the optical phase distribution associated with a microscope image is more difficult to extract. Generally, optical phase detection requires the use of interferometry to encode the phase into amplitude variations. This entails the use of more elaborate optical arrangements. Phase information is useful as the optical phase delay is a sensitive measure of refractive index variations or path length variations. For example, a phase sensitivity of 5 deg at a wavelength of 600 nm translates to an ability to discern a refractive index variation of 10^{-3} in a 10 μm thick specimen.

4.1.2 Phase microscopy

In the biomedical realm, two phase microscopy methods dominate: Phase Contrast Microscopy [1, 2] and Differential Interference Contrast (DIC) Microscopy [3]. The phase information each provides is different. The phase contrast microscopes tend to highlight locations of high scatter – it derives contrast by interfering scattered light components with unscattered light components. On the other hand, the DIC microscope tends to highlight regions where the refractive index of the specimen is rapidly changing. Both techniques can be adapted into a conventional microscopy setup. However, the

requisite optical arrangements are elaborate and, as such, phase microscopes are expensive and relatively high maintenance. In addition, both techniques share a common shortcoming – in both cases, the phase information is inextricably mixed with the amplitude information. In other words, a dark spot in the acquired phase contrast or DIC image can be due to a corresponding absorptive spot on the specimen or a phase variation – there is no way to distinguish the two effects without additional measurements. This shortcoming also prevents phase contrast and DIC microscopy from providing quantitative phase measurements.

Besides phase contrast and DIC microscopy, various full-field quantitative phase imaging techniques [4-11] have been recently developed. Some of the prominent techniques are: 1) phase shifting interferometry schemes [4,5] – where two or more interferograms with different phase shifts are acquired sequentially and a phase image is generated from them, 2) digital holography [6,7] or the Hilbert phase microscopy [8,9] – where high frequency spatial fringes encoded on the interferogram are demodulated to generate the phase image, 3) Swept-source phase microscopy [10] – where modulation in the interferogram generated by a wavelength sweep can be processed to create a phase image, 4) Polarization quadrature microscopy [11] – where phase images are generated by a polarization based quadrature interferometer, and 5) Harmonically matched grating-based phase microscopy [12] – a technique recently developed by our group where we make use of non-trivial phase shifts between the different diffraction orders from a harmonic combination grating to generate phase images. These methods do provide quantitative phase information and have been demonstrated to perform well.

However, as with phase contrast and DIC microscopy, most of these advanced methods contain significant optical elements and have relatively steep learning curves. In addition, this class of phase microscopy techniques invariably requires the use of a laser source to provide coherent light. In comparison, phase contrast and DIC microscopes work well with the usual standard microscope light sources.

4.1.3 DIC microscopy

Because our new phase imaging technique provides phase images similar to those provided by conventional DIC microscopy, it is worth taking a closer look at the operating principle of the DIC microscope. The exact imaging strategy of the DIC microscope can be found from ref. [13]. We will presently skip the technical detail and go right to the heart of the strategy.

In essence, a conventional DIC microscope operates by first creating two identical illumination light fields exploiting polarization selection (Fig. 4-2 (a)). Next, the light fields are laterally displaced (displacement = a) with respect to each other (along x-direction in the Fig. 4-2 (a) example) and are transmitted through the specimen. A net phase lag (typically $\pi/2$) is then introduced on one of the transmitted image light fields. Finally, the two light fields are allowed to interfere with each other at the image plane. Simply put, the process is equivalent to duplicating the transmitted image light field, laterally displacing the copy slightly, and interfering the two light fields.

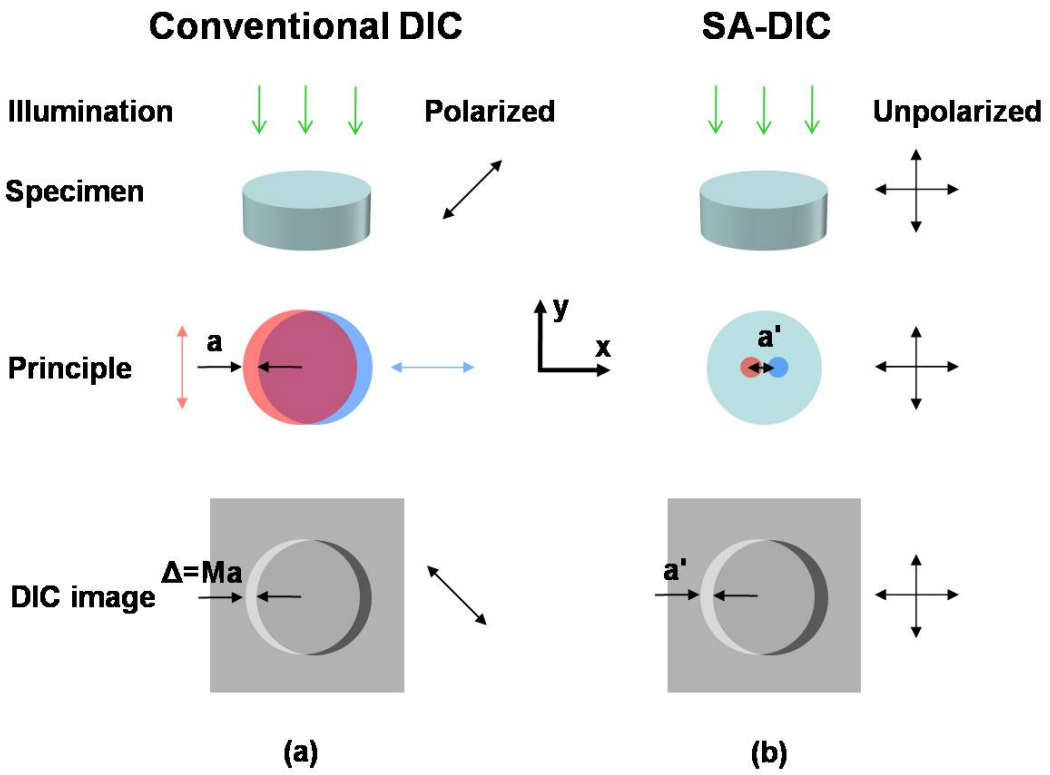

Figure 4-2 (color): Comparison of conventional DIC and structure aperture DIC (SA-DIC) microscope imaging. (a) A conventional DIC microscope operates by interfering slightly displaced duplicate image light fields exploiting polarization selection. **(b)** A SA-DIC microscope operates by interfering light from two adjacent points on the image light field.

Mathematically, this implies that the observed conventional DIC intensity image from a microscope with a magnification factor of M is given by:

$$\begin{aligned} I_{DIC}(x,y) &= \left|\psi_{DIC}(x,y)\right|^2 \\ &= B(x,y) + C(x,y) * \sin\left(\arg\left(\psi(x-\Delta/2,y)\right) - \arg\left(\psi(x+\Delta/2,y)\right)\right), \\ &\approx B(x,y) + C(x,y) * \left(\arg\left(\psi(x-\Delta/2,y)\right) - \arg\left(\psi(x+\Delta/2,y)\right)\right) \end{aligned} \quad (4\text{-}1)$$

where $B(x,y) = \left|\left(\psi(x-\Delta/2,y)\right)\right|^2 + \left|\left(\psi(x+\Delta/2,y)\right)\right|^2$,

$C(x,y) = 2\left|\left(\psi(x-\Delta/2,y)\right)\right|\left|\left(\psi(x+\Delta/2,y)\right)\right|$, $\psi(x,y)$ is the image wavefront as relayed by the microscope for each light field, $\psi_{DIC}(x,y)$ is the DIC image wavefront, and $\Delta = Ma$ is the relative displacement of the images associated with the light fields. The last expression in Eq. (4-1) is valid only when the phase difference is small.

We can see from the above equation that the contrast in DIC is given by the spatial differential phase change across the raw image. In other words, the DIC phase image is mathematically similar to the result of differentiating the raw image phase distribution along the displacement direction Δx.

As we shall later show, such a phase comparison can also be performed by acquiring a simple microscope image of the object after selectively combining-and-interfering the light fields at two adjacent points of the image (separation = a') (Fig. 4-2 (b)). We call this technique structured aperture DIC (SA-DIC) microscopy. SA-DIC can be implemented on the sensor chip and, more importantly, without the use of elaborate bulk optical elements.

In addition, conventional DIC images of birefringent specimens can have significant artifacts as the conventional DIC microscope uses polarization in its phase imaging strategy [14]. Our on-chip phase imager, based on SA-DIC, introduced in the following section is free of those above-mentioned artifacts.

4.2 On-chip phase imager with structured aperture interference

4.2.1 Phase gradient detection with a Young's double slit setup

Let us consider a Young's double slit experiment (Fig. 4-3), where we define two slits with spacing, *Δx,* on a metal coated CMOS image sensor. The spacer between the metal film and the CMOS sensor has refractive index of *n* and thickness of *H*. When a vertical plane wave is incident on the two slits on a metal film, the interference pattern will be centered on the CMOS image sensor. If we put a transparent specimen above the slits, the phase difference induced by the specimen between the two slits will shift the center of the interference pattern to one side. The phase difference *Δφ* is directly related to the offset *Δs* of the interference pattern.

$$\Delta\varphi \approx \frac{2\pi}{\lambda} n \frac{\Delta s}{H} \Delta x , \tag{4-2}$$

when $\Delta s << H$. If the spacing between the two slits is small, we can use this simple and compact Young's interference setup to measure the differential phase ($\frac{\partial\varphi}{\partial x}$) induced by the specimen through a measurement of the offset (*Δs*) of the interference pattern:

$$\frac{\partial\varphi}{\partial x} \approx \frac{2\pi}{\lambda} n \frac{\Delta s}{H} . \tag{4-3}$$

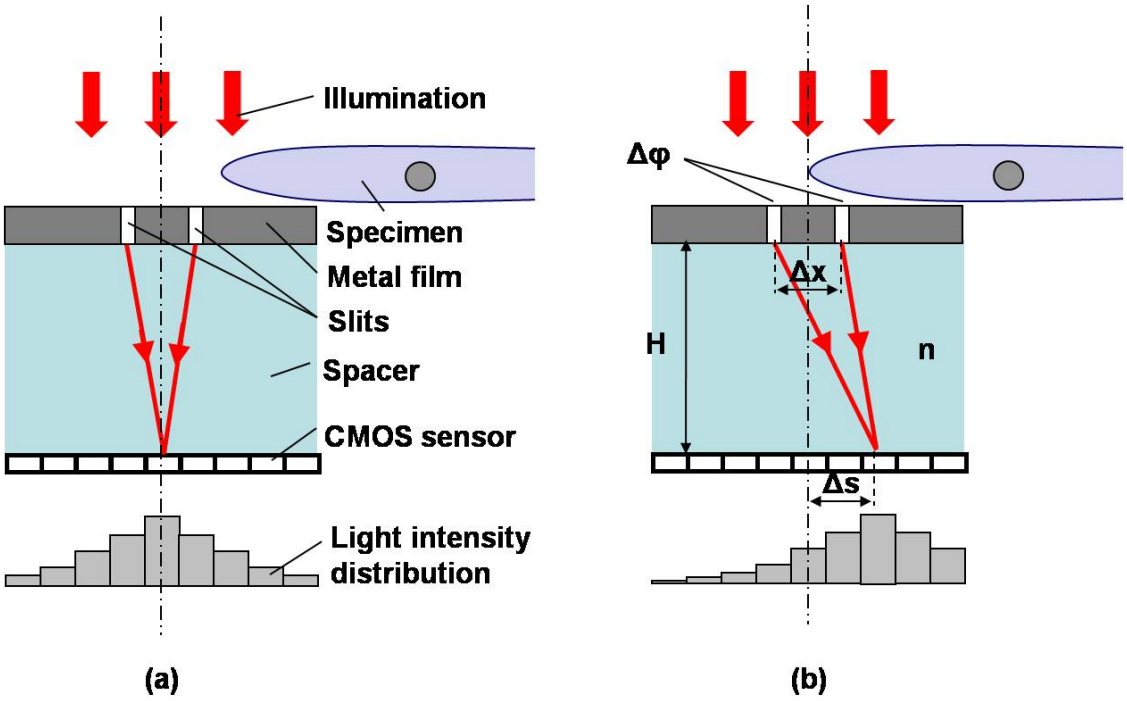

Figure 4-3 (color): Phase gradient detection with a Young's double slit setup. (a) When the illumination is vertical, the phase gradient on the slits is zero and the interference pattern is centered on the CMOS sensor. **(b)** When a specimen is inserted, the interference pattern will shift according to the phase gradient induced by the specimen on the slits.

We can also measure the light transmission of the specimen by simply integrating the entire signal incident on the CMOS image sensor. Because we are measuring the intensity and phase gradient of the light modulated by the specimen through two independent aspects of the Young's interference pattern, we can completely separate the amplitude and phase information of the light from each other. This makes our phase detection technique unique. Of course, Young's double slits experiment is a 1D system,

and only provides us phase gradient information in one direction. However, this can be generalized to 2D. We call structured aperture interference (SAI).

4.2.2 Structured aperture interference (SAI) and structured aperture (SA) wavefront sensor

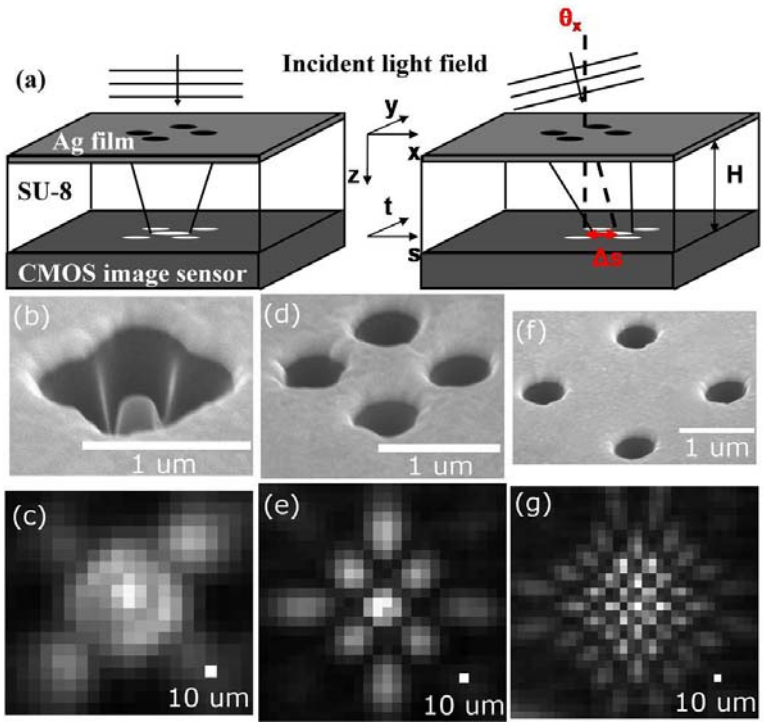

Figure 4-4 (color): Structured aperture interference. (a) Device geometry and principle. **(b)** SEM image and **(c)** interference pattern of 600 nm holes with 600 nm spacing. **(d), (e)** Same plots for holes with 1.2 μm spacing. **(f), (g)** Same plots for holes with 2.4 μm spacing.

Structured aperture interference (SAI) is simply a 2D generalization of Young's interference, where we use four holes instead of two slits on the metal coated CMOS image sensor (Fig. 4-4).

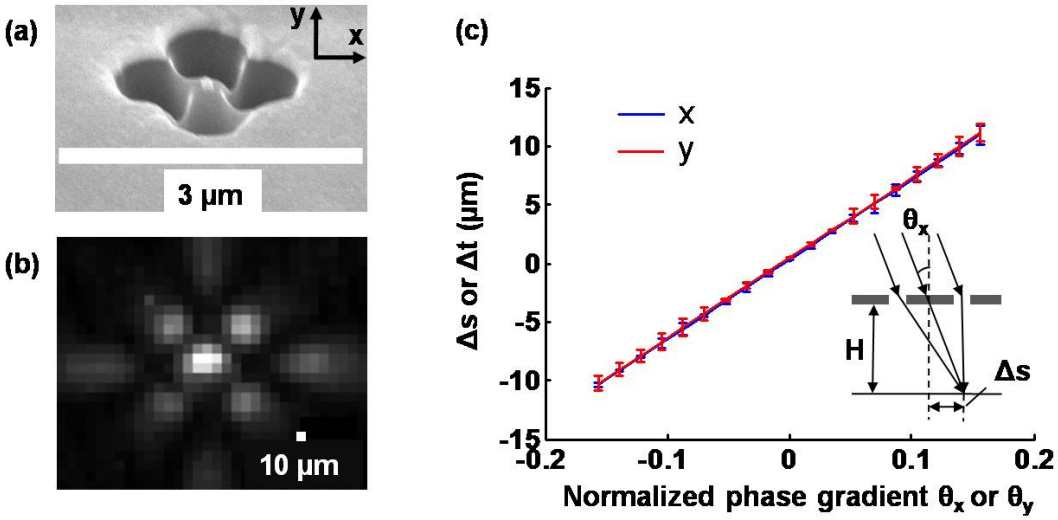

Figure 4-5 (color): Structure aperture (SA) wavefront sensor. (a) SEM image of the SA defined on the silver film. **(b)** the interference pattern of the structure aperture interference recorded by the CMOS image sensor. **(c)** the Δs (Δt) of the zero-order interference spot of the SA is linearly proportional to the phase gradient θ_x in blue (θ_y in red) along the *x*- (*y*-) direction in our measurement range.

In this chapter, we will focus on one particular structured aperture (SA) wavefront sensor based on SAI. The SA wavefront sensor consists of four holes (1 μm diameter for each hole, 1 μm center-to-center hole spacing, with the two long axes in the orthogonal *x*- and *y*- directions respectively) defined in a silver film (100 nm thick) above a CMOS image sensor (Micron MT9V403) (Fig. 4-5 (a)). The holes and the CMOS sensor are

separated by an 80 μm thick layer of SU-8 resin (*d*) (as measured by a Thorlabs Optical Coherence Tomography system OCMP1300SS). The four holes will selectively transmit and combine the light fields from four adjacent points on a wavefront to create an interference pattern on the CMOS sensor. The total transmission of the interference is proportional to the average image intensity at the aperture plane. The offsets (Δs and Δt) of the zero-order interference spot are related to the wavelength-normalized phase gradients (θ_x and θ_y) at the aperture, respectively, [15] through the spacer thickness (*H*):

$$\begin{aligned} \theta_x &= \frac{\lambda}{2\pi}\frac{\partial\varphi}{\partial x} \approx n\frac{\Delta s}{H} \\ \theta_y &= \frac{\lambda}{2\pi}\frac{\partial\varphi}{\partial x} \approx n\frac{\Delta t}{H} \end{aligned}. \tag{4-4}$$

Here we begin using normalized phase gradients θ_x and θ_y instead of $\frac{\partial\varphi}{\partial x}$ and $\frac{\partial\varphi}{\partial y}$, because they are applicable to both coherent and low-coherence phase imaging, and have intuitive meaning – the slope of the wavefront.

The relative simplicity and the absence of image intensity-related terms make SAI a particularly appealing way to measure the phase gradient in both spatial dimensions on the image plane simultaneously.

4.2.3 Phase gradient response

We experimentally determined the exact proportionality of this device by measuring the interference pattern (Fig. 4-5 (b)) as we illuminated the SA with a collimated He-Ne laser beam (632.8 nm wavelength, 25 mm beam diameter, and 4 mW power) from a range of incident angles. We used a least-square 2D Gaussian fit to compute the total transmission and the offsets (Δs and Δt) of the zero-order spot in both *x*- and *y*- directions. Figure 4-5 (c) shows the relationship between Δs (Δt) of the zero-order spot and the normalized phase gradient θ_x and θ_y. Both curves are approximately linear in our measurement ranges. This is consistent with the geometric optics prediction: $\Delta s = H \tan(\theta_x / n) \approx H\theta_x / n$, where θ_x is the normalized phase gradient or incident angle of the laser beam, and when the angle is small; similarly for Δt. Our experimentally measured proportionality from Fig. 4-5 (b) was 70 μm while the predicted thickness (H) was 80 μm. Finally, we note that this SA wavefront sensor works with broadband light sources as well, as the zero-order interference spots coincide spatially for all wavelengths.

4.3 Proof-of-concept experiment

4.3.1 Quantitatively imaging the phase front of a Gaussian and optical vortex beam

To demonstrate the quantitative phase imaging capability of our SA wavefront sensor, we projected a collimated He-Ne laser beam (4.2 mm spot diameter, 2 mW intensity) through an aspheric lens (Thorlabs C220TME-B, 11 mm focal length) focused ahead of the device (i.e., $z > 0$). This creates a differential phase pattern given by:

$$\begin{aligned} \nabla \phi_{Gaussian}(u,v,z) &= \frac{\partial \phi_{Gaussian}(u,v,z)}{\partial u}\hat{u} + \frac{\partial \phi_{Gaussian}(u,v,z)}{\partial v}\hat{v} \\ &= \frac{ku}{z\left[1+(z_0/z)^2\right]}\hat{u} + \frac{kv}{z\left[1+(z_0/z)^2\right]}\hat{v} \end{aligned}, \tag{4-5}$$

where $k = 2\pi/\lambda$, $z_0 = \pi w_0^{\,2}/\lambda$, and w_0 is the minimum waist radius of the beam. Our device was raster-scanned by a motorized (Newport CMA-25CCCL) two-axis precision translation stage controlled by a Newport ESP-300 motor controller. The motor controller and camera were coordinated by custom computer software to automate raster scanning and snapshot routines. The amplitude and differential phase profiles of the Gaussian beam are shown in Fig. 4-6 (a-d). Note that crosstalk between amplitude and differential phase measurements in Fig. 4-6 (a-c) is virtually nonexistent. The term differential phase instead of the normalized phase gradient is used in this section because it is more convenient for the quantitative phase measurement of a laser beam.

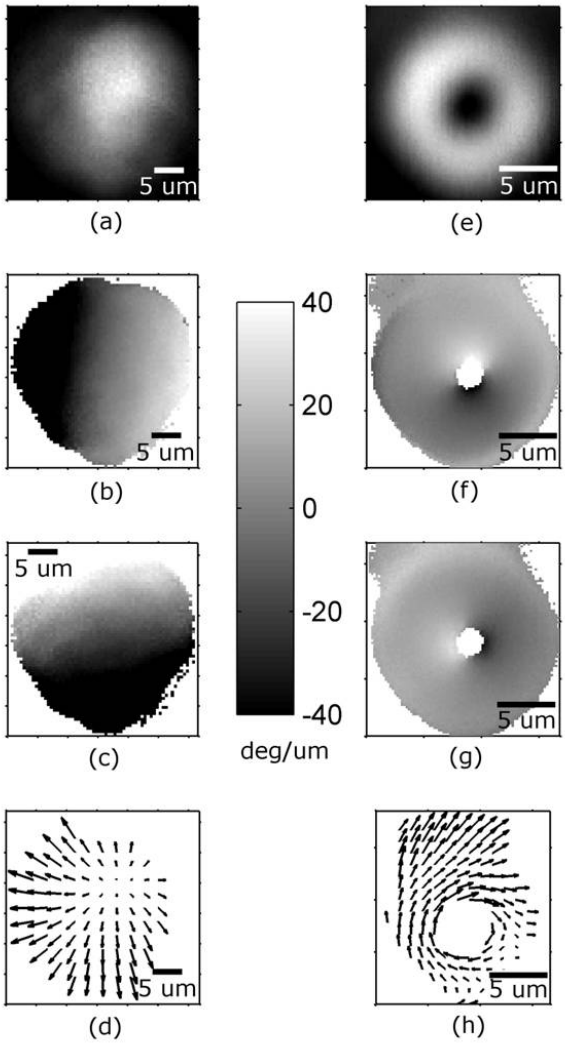

Figure 4-6: Quantitatively imaging the phase front of a Gaussian and optical vortex beam. (a) Intensity, **(b)** *u* component, **(c)** *v* component of differential phase, and **(d)** vector representation of the differential phase of a Gaussian beam. **(e–h)** Same plots for an optical vortex.

Next, we used a computer-generated hologram to generate an optical vortex [16] of topological charge one to image with our device. The interference pattern of a plane wave and an optical vortex at a 2 degree incidence angle was computed and used as the pattern for a chrome mask. A collimated He-Ne laser beam (2 mW intensity) was projected onto the hologram, and the first-order diffraction component (3.9 mm spot diameter) was focused onto our device (i.e., $z = 0$) by a plano-convex lens (Thorlabs LA1951, 25.4 mm focal length). This creates a differential phase pattern given by

$$\nabla \phi_{vortex}(u, v, z = 0) = -\frac{mv}{u^2 + v^2}\hat{u} + \frac{mu}{u^2 + v^2}\hat{v}, \tag{4-6}$$

where m is a signed integer called the topological charge. Our device was scanned across the vortex to measure its amplitude and differential phase profiles, which are shown in Fig. 4-6 (e-h). The differential phase of the vortex rotates about the center and is larger near the center, as predicted by Eq. (4-6). The experimentally measured line integral around the vortex in the $\hat{\theta}$-direction equals 332 degrees with a standard deviation of 3.71 degrees for radii between 2 and 4 μm.

4.3.2 Off-chip demonstration of DIC-OFM

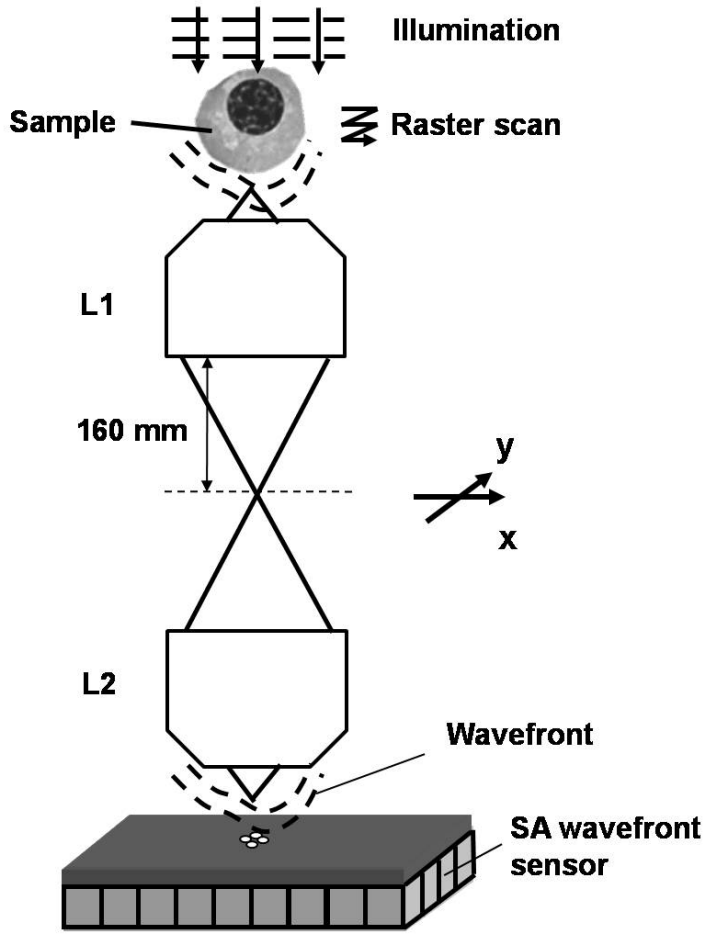

Figure 4-7: Off-chip demonstration of DIC-OFM. A 1:1 optics relay system is used to create a virtual specimen onto our SA wavefront sensor, and we raster-scanned the specimen in the *x*-*y* plane to complete the mapping of the intensity and phase gradient image.

In order to demonstrate the feasibility of the phase imaging of a biological specimen in an OFM device, we setup a 1:1 optics relay system to project a virtual specimen on our SA wavefront sensor. The experimental scheme is shown in Fig. 4-7. We aligned two 20× objective lenses (Newport M-20×) such that their rear conjugate planes (160 mm behind the objective lens) overlapped. We placed the specimen at the front conjugate plane of the top objective (L1), and illuminated it with collimated white light (halogen lamp, 200 mW/cm^2). Since the microscope system was symmetric, it formed a 1:1 image of the specimen at the front conjugate plane of the bottom objective (L2); this image was equal to the convolution of the input specimen light field with the PSF of the microscope system. Our SA wavefront sensor was placed at the center of the image plane. We raster-scanned (using two Newport CMH-25CCCL actuators) the specimen in the *x*-*y* plane to complete the mapping of the intensity and phase gradient images.

We chose a starfish embryo (Carolina Scientific) as a test specimen. Figure 4-8 (a) shows a microscope (Olympus BX41) image of the specimen acquired with a 10× objective. Figure 4-8 (b) is the corresponding image under a standard DIC microscope (Zeiss Axioplan, 40× objective). Figure 4-8 (c-e) shows the intensity, as well as *X* and *Y* phase gradient images acquired by our off-chip DIC-OFM demonstration setup. The spatial sampling step size was 0.5 μm in both *x*- and *y*- directions, and the exposure time associated with each sampling point was 8 ms.

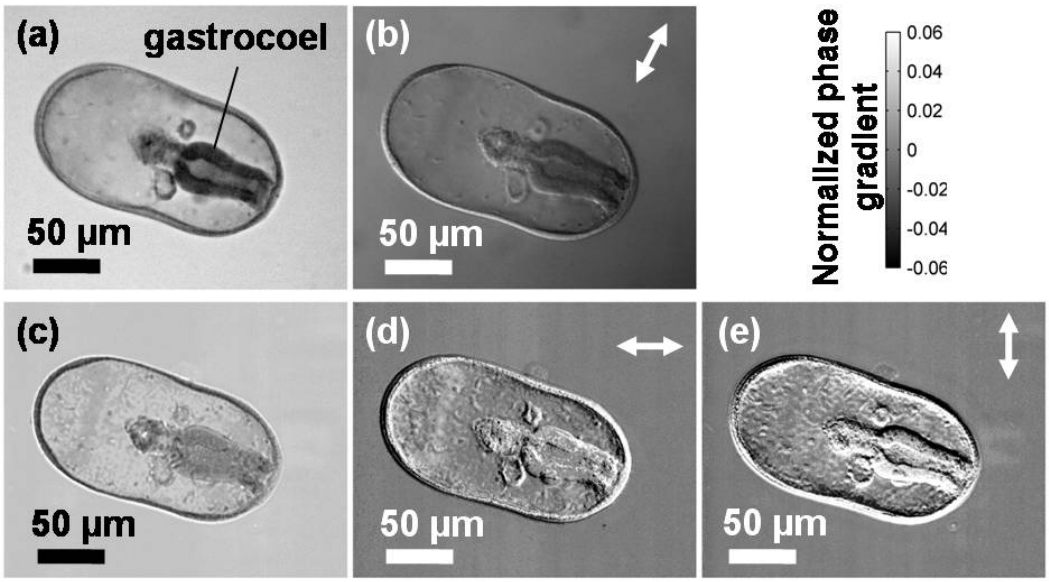

Figure 4-8: Images of starfish embryo. (a) Conventional transmission microscope image. **(b)** Conventional DIC microscope image. The **(c)** intensity, **(d)** X and **(e)** Y phase gradient images from the off-chip DIC-OFM demonstration setup. (Double arrows represent the phase gradient directions)

The conventional transmission microscope image and our intensity image are consistent with each other. On the other hand, our phase gradient images do appear to be different from the conventional DIC image. This is because, while our phase gradient images purely map the phase gradients, the conventional DIC image contains intensity image variations as well. This distinction is particularly apparent when we compare the gastrocoel of the embryo for all of the images. The image intensity associated with that region is low and the region appears darker in the conventional DIC image. In comparison, the corresponding areas of our phase gradient images do not appear darker

because they are pure phase maps. Finally, we note that the phase gradient and amplitude images are also an improvement over conventional DIC images in that they are quantitative maps. The wavefront gradient sensitivity of our prototype operating in the above described experimental conditions is approximately 4 mrad; the sensitivity can be improved by using a better sensor platform, increasing the measurement time, and/or increasing the illumination intensity [15].

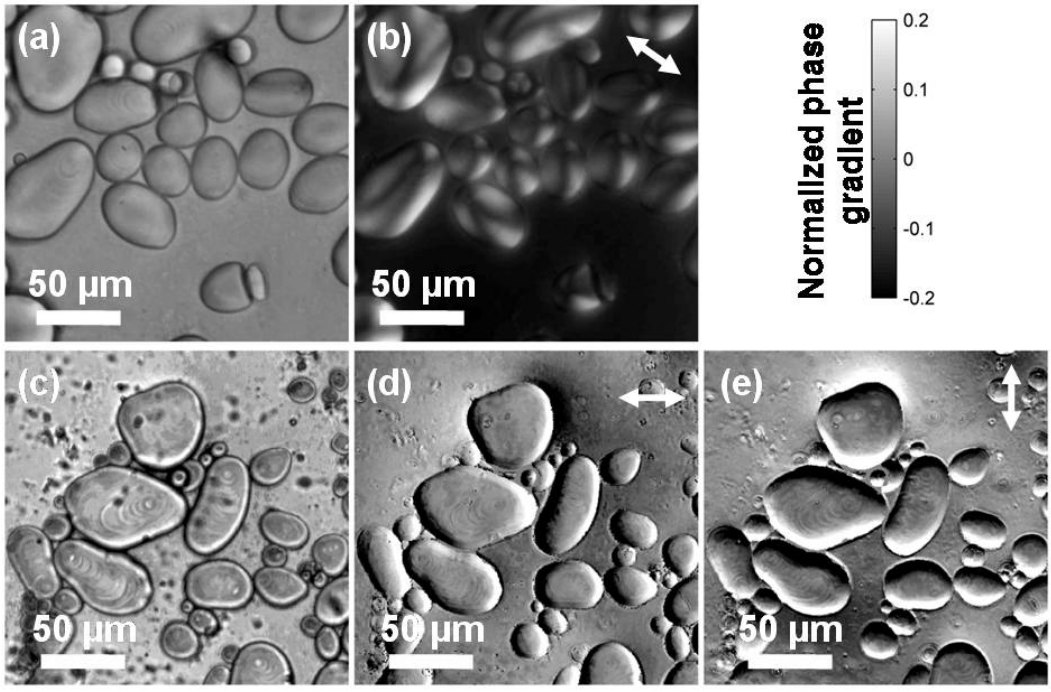

Figure 4-9: Images of potato starch storage granules in microscope immersion oil. (a) Conventional transmission microscope image. **(b)** Maltese-cross artifacts in the conventional DIC image. The **(c)** intensity, and artifact-free **(d)** *X* phase gradient and **(e)** *Y* phase gradient images from the off-chip DIC-OFM demonstration setup. (Double arrows represent the phase gradient directions)

The ability of our system to image birefringent specimens properly is yet another advantage. Birefringent objects, such as the potato starch storage granules, can alter the polarization of the two displaced light fields in a conventional DIC microscope, such that the subsequent combination of the two fields is no longer describable by Eq. (4-1). This can give rise to Maltese-cross artifacts in the resulting conventional DIC images (Fig. 4-9 (b)) [14]. Since our DIC-OFM demonstration uses unpolarized illumination and does not rely on polarization for image processing, it can image birefringent specimens without artifacts, as shown in Fig. 4-9 (d, e). It is also worth noting that the dark absorption spots of the starch granules in the center of the intensity images (Fig. 4-9 (c)) do not appear in our phase gradient images (Fig 4-9 (d, e)). This is another clear indication that our DIC-OFM demonstration can separate the intensity variations of the image wavefront from the phase variations.

4.4 Future on-chip DIC-OFM

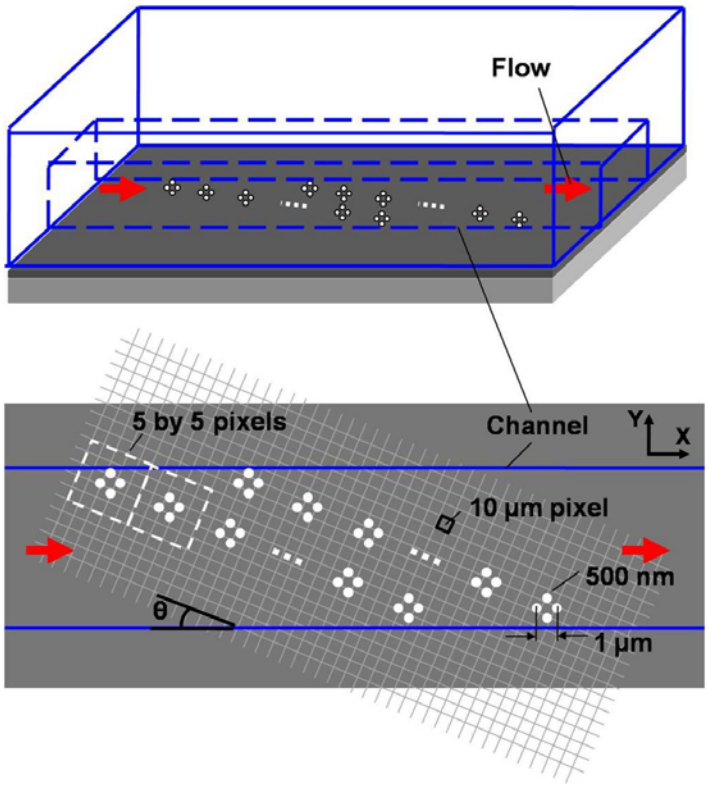

Figure 4-10 (color): Proposed DIC-OFM configuration. Two line arrays of four-hole apertures on an Al coated CMOS image sensor. When a specimen passes through, each line of apertures will generate a transmission intensity image and two orthogonal phase gradient images for the same specimen. By evaluating the cross-correlation between these two sets of images, we can evaluate the consistency of the DIC-OFM imaging.

Although we used a 2D scanning system to complete the image acquisition (raster-scanning) in the proof-of-concept experiment, it is straightforward to translate this process into an OFM imaging scheme and make the image scanning done in parallel by

OFM apertures. For example, we can punch two line arrays of four-hole apertures on an Al coated CMOS image sensor (Micron MT9V403C12STM, 9.9 μm pixel size) (Fig. 4-10). The four holes are arranged in a 'plus' sign pattern. The diameter of each hole is 500 nm; the spacing between diagonal holes is 1 μm. The tilt angle θ of two apertures arrays is in such way that the spacing between neighboring apertures in the Y direction is 500 nm to ensure a double sampling rate. When a specimen passes, each line of apertures will collect the information needed to generate a transmission intensity image and two orthogonal phase gradient images for the same specimen. By evaluating the cross-correlation between these two sets of images, we can evaluate the consistency of the DIC-OFM imaging.

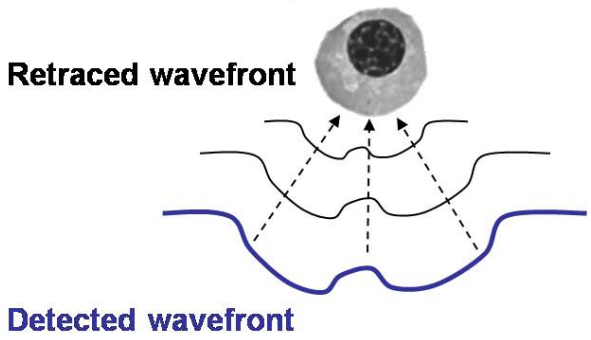

Figure 4-11 (color): Changing the focus of OFM imaging numerically. Based on electromagnetic theory, if we know the boundary conditions (including amplitude and phase) of an EM wave, we can retrace the wavefront back numerically, and compute the specimen image at any plane above the detection plane.

More ambitiously, we want to explore the possibility of rendering 3D structures of cells or microorganisms with the lensless and fully on-chip DIC-OFM microscope. Our previous OFM experiments measure only the 2D intensity projection image of the specimen at the aperture plane, with the focal plane of the OFM is fixed at the aperture plane [17] (see the discussion in Section 2.6.1). Thus, the structures at the bottom of the specimen appear sharper in the OFM image than the structures at the top. This prevents high-resolution imaging of the entire specimen body. DIC-OFM provides us with complete knowledge of both amplitude and phase information of the specimen wavefront at the aperture plane, and this suggests a potential way to change the focus of OFM imaging numerically. Based on the electromagnetic (EM) theory, if we know the boundary conditions (including amplitude and phase) of an EM wave, we can retrace the wavefront back numerically, and compute the specimen image at any plane above the detection plane (Fig. 4-11). This means we can run cells or microorganisms through a lensless and fully on-chip DIC-OFM device, and potentially compute complete 3D structural information of all specimens. However, this is also a challenging research topic. For example, we would need to reconstruct the phase profile of the specimen image from the two orthogonal differential phase components of DIC-OFM data. This reconstruction is theoretically possible, but noise in the differential phase data may impose implementation difficulties. Luckily, there are several published works that discuss solving this problem [18-22].

4.5 Conclusion

In conclusion, we have demonstrated that it is possible to use the SA wavefront sensor to achieve high-resolution and artifact-free quantitative phase microscopy images of laser beams and biological specimens. By adapting SA wavefront sensors into an OFM imaging scheme, it is feasible to construct a complete on-chip DIC-OFM device. It not only can enable a compact phase imaging solution for examining transparent samples in cases where staining is not an option, but also inspired an interesting line of research – 3D on-chip cell imaging based on complete wavefront detection.

Bibliography

1. F. Zernike, "Phase contrast, a new method for the microsopic observation of transparent objects," Physica **9**, 686-698 (1942).
2. F. Zernike, "Phase contrast, a new method for the microscopic observation of transparent objects Part II," Physica **9**, 974-986 (1942).
3. R. D. Allen, G. David, and B. G. Nomarski, "The Zeiss-Nomarski differential interference equipment for transmitted light microscopy," Z. wiss. Mikr. **69**, 8 (1969).
4. K. Creath, "Phase-measurement interferometry techniques," Prog. Opt. **26**, 44 (1988).
5. K. J. Chalut, W. J. Brown, and A. Wax, "Quantitative phase microscopy with asynchronous digital holography," Optics Express **15**, 3047-3052 (2007).
6. P. Marquet, B. Rappaz, P. J. Magistretti, E. Cuche, Y. Emery, T. Colomb, and C. Depeursinge, "Digital holographic microscopy: a noninvasive contrast imaging technique allowing quantitative visualization of living cells with subwavelength axial accuracy," Optics Letters **30**, 468-470 (2005).
7. B. Rappaz, P. Marquet, E. Cuche, Y. Emery, C. Depeursinge, and P. J. Magistretti, "Measurement of the integral refractive index and dynamic cell morphometry of living cells with digital holographic microscopy," Optics Express **13**, 9361-9373 (2005).
8. T. Ikeda, G. Popescu, R. R. Dasari, and M. S. Feld, "Hilbert phase microscopy for investigating fast dynamics in transparent systems," Optics Letters **30**, 1165-1167 (2005).
9. G. Popescu, T. Ikeda, K. Goda, C. A. Best-Popescu, M. Laposata, S. Manley, R. R. Dasari, K. Badizadegan, and M. S. Feld, "Optical measurement of cell membrane tension," Physical Review Letters **97** (2006).
10. M. V. Sarunic, S. Weinberg, and J. A. Izatt, "Full-field swept-source phase microscopy," Optics Letters **31**, 1462-1464 (2006).
11. D. O. Hogenboom, C. A. DiMarzio, T. J. Gaudette, A. J. Devaney, and S. C. Lindberg, "Three-dimensional images generated by quadrature interferometry," Optics Letters **23**, 783-785 (1998).
12. Z. Yaqoob, J. G. Wu, X. Q. Cui, X. Heng, and C. H. Yang, "Harmonically-related diffraction gratings-based interferometer for quadrature phase measurements," Optics Express **14**, 8127-8137 (2006).
13. http://www.microscopyu.com/articles/dic/dicindex.html,
14. http://micro.magnet.fsu.edu/primer/techniques/dic/dicphasecomparison.html.
15. M. Lew, X. Cui, X. Heng, and C. Yang, "Interference of a four-hole aperture for on-chip quantitative two-dimensional differential phase imaging," Optics Letters **32**, 2963-2965 (2007).
16. Z. S. Sacks, D. Rozas, and G. A. Swartzlander, "Holographic formation of optical-vortex filaments," Journal of the Optical Society of America B-Optical Physics **15**, 2226-2234 (1998).
17. X. Q. Cui, L. M. Lee, X. Heng, W. W. Zhong, P. W. Sternberg, D. Psaltis, and C. H. Yang, "Lensless high-resolution on-chip optofluidic microscopes for Caenorhabditis elegans and cell imaging," Proceedings of the National Academy of Sciences of the United States of America **105**, 10670-10675 (2008).

18. A. Agrawal, R. Raskar, and R. Chellappa, "What is the range of surface reconstructions from a gradient field?," in *Computer Vision - ECCV 2006. 9th European Conference on Computer Vision. Proceedings, Part I*, A. Leonardis, H. Bischof, and A. Pinz, eds. (Springer-Verlag, Graz, Austria, 2006), pp. 578-591.
19. M. Harker, and P. O'Leary, "Least squares surface reconstruction from measured gradient fields," in *2008 IEEE Conference on Computer Vision and Pattern Recognition (CVPR)*(Ieee, Anchorage, AK, USA, 2008), pp. 7 pp.-7 pp.
20. R. Frankot, R. Chellappa, H. Co, and C. El Segundo, "A method for enforcing integrability in shape from shadingalgorithms," IEEE Transactions on pattern analysis and machine intelligence **10**, 439-451 (1988).
21. T. Kuparinen, V. Kyrki, J. Mielikainen, and P. Toivanen, "On Surface Topography Reconstruction from Gradient Fields," (2007).
22. F. Roddier, and C. Roddier, "Wavefront reconstruction using iterative Fourier transforms," Applied Optics **30**, 1325-1327 (1991).

PART II WAVEFRONT MICROSCOPY (WM)

Part II is about a new microscopy concept – wavefront microscopy (WM). By simply adding our newly developed wavefront image sensor (WIS) onto the camera port of an optical microscope, we can turn it into a WM, which can detect both the amplitude and phase information of the wavefront induced by the specimen quantitatively and separately with a single data acquisition. It provides an easy and cost-effective solution for researchers and clinicians to incorporate phase imaging functionality into their current microscope systems, which could allow easier quantitative phase mapping of biological specimens and facilitate deep tissue imaging.

In Chapter 5, we will first introduce the enabling component of WM – wavefront imaging sensor (WIS). In Chapter 6, we will demonstrate how to turn a standard microscope into a WM by simply adding a WIS onto the camera port of the microscope, and the application of WM in imaging biological specimens. In Chapter 7, we will discuss some fundamental aspects about the imaging process of WM.

Chapter 5: Wavefront Image Sensor (WIS)

In this chapter, we will report a new class of imaging sensor, termed wavefront image sensor (WIS), which is capable of simultaneously measuring both the amplitude and phase information of a light field. Compared to a conventional wavefront sensor, our WIS has a much denser grid of apertures (spacing = 11 μm, diameter = 6 μm) patterned on an aluminium (Al) layer, which makes it more suitable for measuring the complicated wavefronts in biological imaging. By monitoring the tightly confined transmitted light spots in the high Fresnel number regime, we can accurately measure both intensity and phase front variations (a measured normalized phase gradient sensitivity of 0.1 mrad under the typical working condition - 1.0 second total signal accumulation time and 9.2 $\mu W/cm^2$ light intensity on the sensor). The WIS is not only the enabling component for wavefront microscopy (WM) (see next chapter), but also has broad applications in adaptive optics, LASIK surgery, machine recognition, texture assessment, and object ranging.

We will first start with the motivation – integrating optical functions onto an image sensor. Then we will review the challenges faced by current wavefront sensors, and present our approach. Next, we will describe a computer simulation and an off-chip verification experiment to show that our WIS works in the high Fresnel number regime. We will then introduce a new position estimation method, the cyclic algorithm, to calculate the normalized phase gradient of the wavefront over each WIS aperture. After that, we will present a calibration experiment to characterize the linearity and sensitivity of the WIS. Finally, we will conclude with discussion about how to improve the WIS.

5.1 Background

5.1.1 Integrating optical functionalities onto an image sensor

The first generation of monochromatic image sensors, e.g. CCD or CMOS, functioned as a basic light detection array; they did not optically manipulate the incident light field prior to detection. Later, researchers realized that color imaging could be easily achieved by incorporating individual optical filters on top of each pixel. In this way, we can take color images in a single-snapshot and, at the same time, eliminate the complexity of having to incorporate external and bulky optical filters in the optical systems.

Along a similar line of logic, we aim to explore the possibility of integrating some of the optical complexity in a microscope system onto an image sensor. This way, we will potentially simplify the implementation of microscope, and make the entire microscope system more robust.

5.1.2 Wavefront sensor

The wavefront sensor is a simple and elegant method for measuring the shape of a wavefront. It originated from the Hartmann screen test [1], which consists of a macro-scale aperture array arranged above an opaque screen in the aperture of a telescope, and was first proposed as a system for examining the optical aberrations of a telescope. However, the broadened light transmission through the apertures due to diffraction significantly limit sensitive detection and necessitate wide separation between the apertures, which in turn limits the number of useful image pixels. Later, the incorporation of a lens array into Shack-Hartmann sensors [2] allowed the formation of tighter light

spots. Nevertheless, the relatively large lens dimensions (typically on the order of 100 microns), the associated low image pixel numbers, and the general assembly difficulties have limited such sensors to pure phase measurements of relatively simple wavefronts in fields in which cost, ease-of-use and size are minor considerations, specifically astronomy, metrology and, increasingly, ophthalmology [1].

Here, we report a high-density and low-cost wavefront imaging sensor (WIS) that works in the high Fresnel number regime, and is capable of measuring both intensity and phase front variations.

5.2 Principle

The wavefront imaging sensor (WIS) consists of a 2D array of circular apertures defined on top of a metal coated image sensor; a spacer separates the apertures from the sensor pixels (Fig. 5-1 (a, b)). The coordinate systems we use in the part II of the thesis are shown in Fig. 5-1 b. When a plane wave of light is incident upon the aperture array, the transmission through each aperture forms a projection spot on the sensor pixels underneath. When a light wave with an unknown wavefront impinges upon the aperture array, the center of each projection spot will shift according to the normalized phase gradient of the light wave over its corresponding aperture. Mathematically, this shift in the *s*-direction can be expressed as

$$\Delta s(x,y) \approx H\frac{\theta_x(x,y)}{n} = \frac{H\lambda}{2\pi n}\frac{\partial\phi(x,y)}{\partial x} \tag{5-1}$$

when $\Delta s(x,y) << H$, where H is the distance from the aperture to the image sensor, $\theta_x(x,y)$ is the normalized phase gradient of the light wave along the *x*-direction over the

aperture (x, y), λ is the wavelength of the light wave, n is the refractive index of the spacer material, and $\frac{\partial \phi(x,y)}{\partial x}$ is the wavelength-dependent phase gradient along the x-direction over the aperture (see Fig. 5-1 (a, b) for coordinate references) [3]. Corresponding expressions for the light field along the y-directions can be written in a similar fashion.

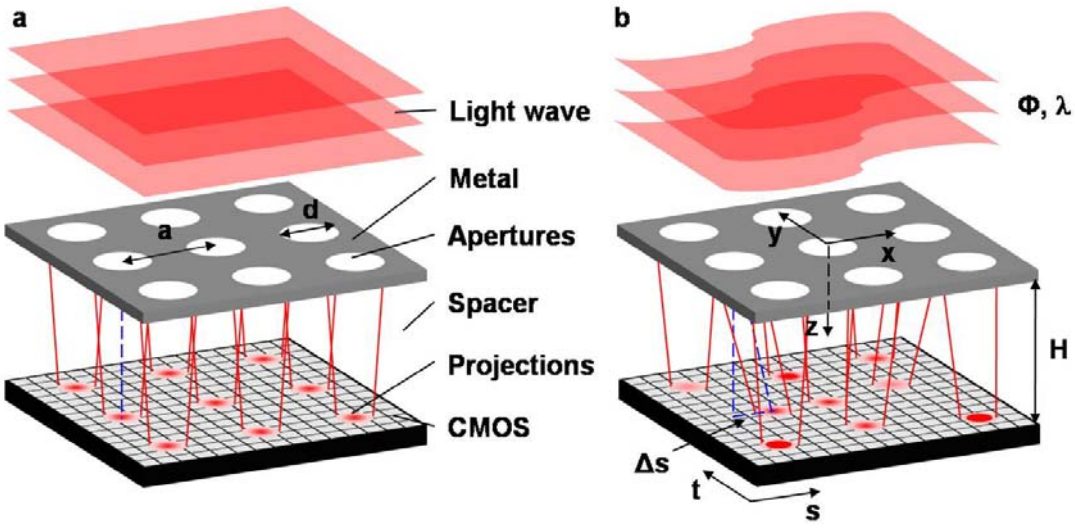

Figure 5-1 (color): Schematic of the wavefront image sensor (WIS). WIS apertures (white circles) are defined on the metal (gray) coated 2D CMOS image sensor (light gray grid). The spacer separates the apertures away from the image sensor. **(a)** The aperture projections (red circles) are evenly distributed on the image sensor under a vertical plane illumination. **(b)** The change of in transmission and shift of the aperture projections under an unknown light wave.

The close relationship between θ_x and $\frac{\partial \phi(x,y)}{\partial x}$, and our subsequent usage of θ_x deserves some elaboration. The normalized phase gradient, θ_x (and θ_y) can be appreciated as a wavelength-independent measure of the angle at which the incoming light impinges upon the aperture. In other words, θ_x (and θ_y) measures the directionality of the incoming light field. As the light source employed in these experiments is a broadband halogen lamp in a standard microscope, the choice of θ_x (and θ_y) for subsequent discussions is more straightforward.

In addition to providing a measure of θ_x (and θ_y), each projection spot also provides a measurement of the local light field intensity over its corresponding aperture. We obtain this value by summing the total light power associated with the projection spot (Fig. 5-1 (b)). Therefore, the WIS is able to retrieve the amplitude and phase information of the unknown light wave separately by simply evaluating two independent aspects of each projection spot.

We assign a grid of $N \times N$ pixels underneath each aperture to measure the transmission and shift of the projection spot. It has been proven in other studies [4-5] that estimating the shift of the projection spot with subpixel precision can be achieved even when the number of pixels involved (N) is small. If an image sensor with $MN \times MN$ pixels is used, we can then create a WIS with $M \times M$ apertures, or effectively generate a light field image of $M \times M$ pixels. Throughout this article, we will refer to pixels on the sensor as sensor pixels, and the smallest image point in the rendered light field image as image pixels.

5.3 Self-focusing effect of WIS apertures in the high Fresnel number regime

Our technology differs from conventional wavefront sensors in that we recognize that the projection spot from an aperture placed at appropriately close proximity to a sensor operates in the high Fresnel number regime (more specifically, $F = \frac{nd^2}{4H\lambda} = \frac{1.6 \times (6\mu m)^2}{4 \times 28\mu m \times 0.6\mu m} = 0.86$ in our case) and can therefore be tightly confined. In other words, light transmitted through an aperture would actually self-focus close to the aperture before spreading (diffraction); we design our device such that our sensor is located at the plane where this self-focusing occurs. Additionally, the lateral shifts of this projection spot are still responsive to the phase front gradients of the incident light field. These two facts enable us to create a simple-to-implement, highly compact, high-density (11 μm spacing between apertures), high image pixel count (280 × 350 image pixels over a sensor area of 3.08 mm × 3.85 mm in our prototypes) and high sensitivity WIS.

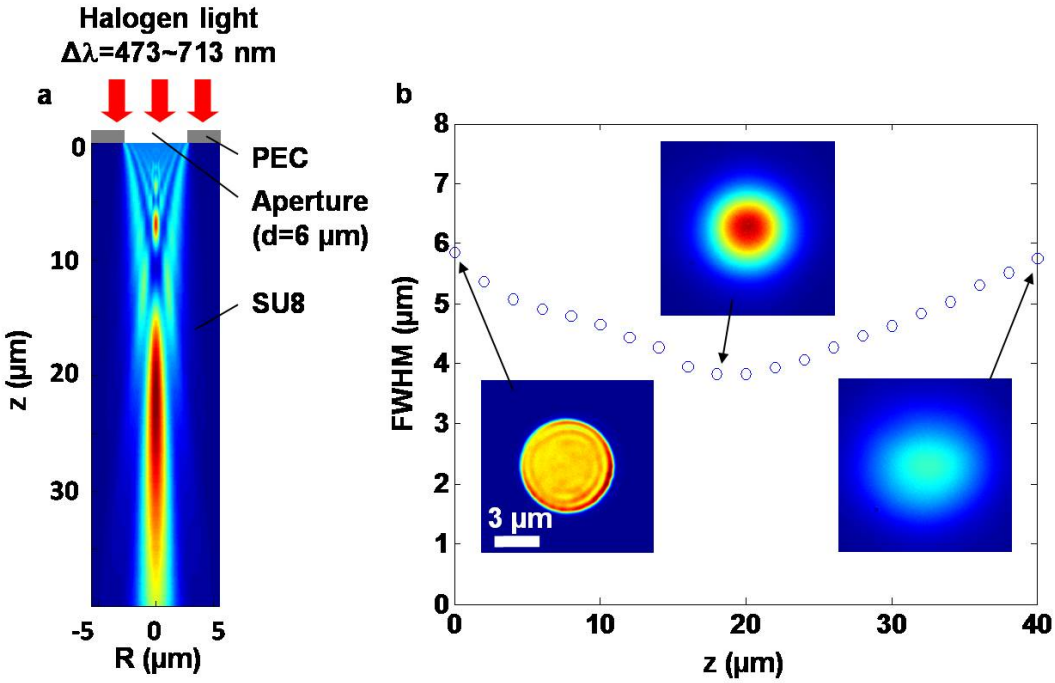

Figure 5-2 (color): Self-focusing effect of WIS apertures in the high Fresnel number regime. (a) The simulation of the diffraction (in SU8 resin) through a 6 μm diameter WIS aperture defined on a perfect electric conductor (PEC) layer illuminated by a halogen lamp. **(b)** Experimental data showing the self-focusing effect of a WIS aperture on an Al coated glass coverslip. The insets are the cross-sections of the aperture diffraction pattern perpendicular to the *z* axis.

We performed a 3D and broadband finite-difference time-domain **(**FDTD) simulation (CST Microwave Studio from CST of America, Inc.) to determine the light projection pattern associated with a WIS aperture. The aperture diameter was set at 6 μm, and the refractive index of the spacer material was set at 1.6 (Fig. 5-2 (a)). To reduce the complexity of the simulation, a 150 nm thick perfect electric conductor (PEC) film was

modelled in place of the Al layer we deposit on our WIS sensor. As the halogen lamp used with our WIS and WM system is a broadband light source, our simulation was performed over a range of wavelengths (473 - 713 nm) at an interval of 20 nm. We summed the simulation results, weighted based on the power distribution of the halogen lamp. As we can see from Fig. 5-2 (a), the projection light spot shrinks to a tightly confined spot (high Fresnel number regime) before expanding in an approximately linear fashion (as predicted by considering diffraction in the low Fresnel number regime).

Next, we implemented an experiment to quantitatively measure the actual projection light spot from a WIS aperture. First we punched a 6 μm aperture on an Al coated (150 nm thick) glass coverslip (refractive index n = 1.5). Then, we illuminated the aperture with the halogen lamp and used a microscope with an oil immersion 100× objective lens (*N.A.* = 1.3) to image the projection spot at different axial locations (Fig. 5-3). The result is plotted in Fig. 5-2 (b). We can see that the width of the spot (full width at half maximum – FWHM) reached a minimum (measured width = 3.8 μm) at an axial displacement of H = 18 μm.

We note that the simulation and experiment results share similar trends but do differ to some extent. We believe that the discrepancies are attributable to differences in aperture profile (the experimentally milled apertures tend to be rounder around the edges and texturally rougher than the simulation ideals), the finite grid density limitation associated with the simulation, and inadequacies of the spectral range coverage of the simulation (we only simulated the case for twelve discrete wavelengths in the spectrum range). Our WIS prototype was designed and implemented based on our experimental findings.

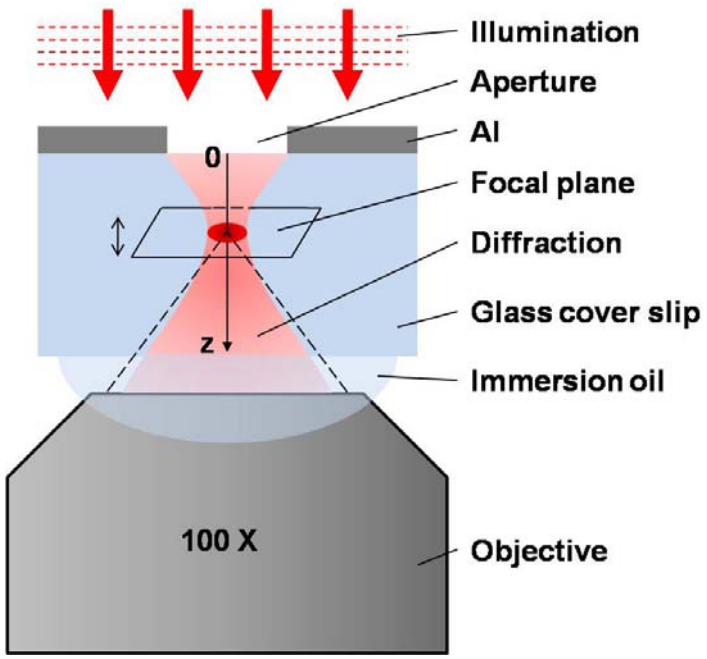

Figure 5-3 (color): Measuring the diffraction of a WIS aperture under the illumination of a halogen lamp. A 6 μm aperture was first etched on an Al coated (150 nm thick) glass coverslip (refractive index of 1.5), and then illuminated by a halogen lamp (The central wavelength was 0.6 μm and the FWHM of the spectrum was 0.2 μm). Cross-sections of the aperture diffraction at different *z* planes were imaged by a microscope with an oil (refractive index of 1.5) immersed 100× objective (*N.A.* = 1.3) by moving the focal plane of the microscope along the *z* axis with a micrometer at intervals of 2 μm.

5.4 Fabrication

As mentioned earlier, our ability to build a WSI is dependent on the tight projection spot confinement achieved by choosing a high Fresnel number optical design. Our evaluation experiments indicate that a 6 μm aperture can project a spot with diameter of 3.8 μm (FWHM) at a height of H = 18 μm above the sensing surface – 37% smaller than the aperture diameter itself. This spot size confinement is robust; we found that the spot diameter remained below 5 μm (FWHM) for H ranging between 4 and 34 μm.

Our high-density WIS (Fig. 5-4 (a, b)) prototype was fabricated with a commercially available complementary metal–oxide–semiconductor (CMOS) image sensor (MT9P031I12STM from Aptina Imaging) as the substrate. There are 1944 × 2592 pixels of size 2.2 μm on the sensor. We removed its glass window to gain access to the surface of the sensor. Next we planarized the surface of the sensor die with a 10 μm thick layer of SU8 resin, and then coated it with a 150 nm thick layer of Al to mask the sensor from light. The SU8 layer served two functions. First, the SU8 layer nullified the optical properties of the lenses on top of each sensor pixel. These tiny and relatively low-quality lenses are ubiquitous in the current generation of CMOS sensors. They serve to more efficiently funnel light onto the light sensitive region of the sensor pixels. Their presence should have minimal impact on our WIS prototype and, in fact, they should improve light collection efficiency and boost our signals. However, to make our initial WIS demonstration clear and unambiguous, we decided to nullify the lenses with the SU8 layer. Second, the SU8 layer served as a spacer between the Al layer and the sensor pixels. A stack of proprietary materials in the sensor functioned as an additional spacer as

well. Finally, we used photolithography to create a 2D aperture array (280×350 apertures, 6 μm aperture diameter and 11 μm aperture-to-aperture spacing) on the Al film (Fig. 5-4 (b)).

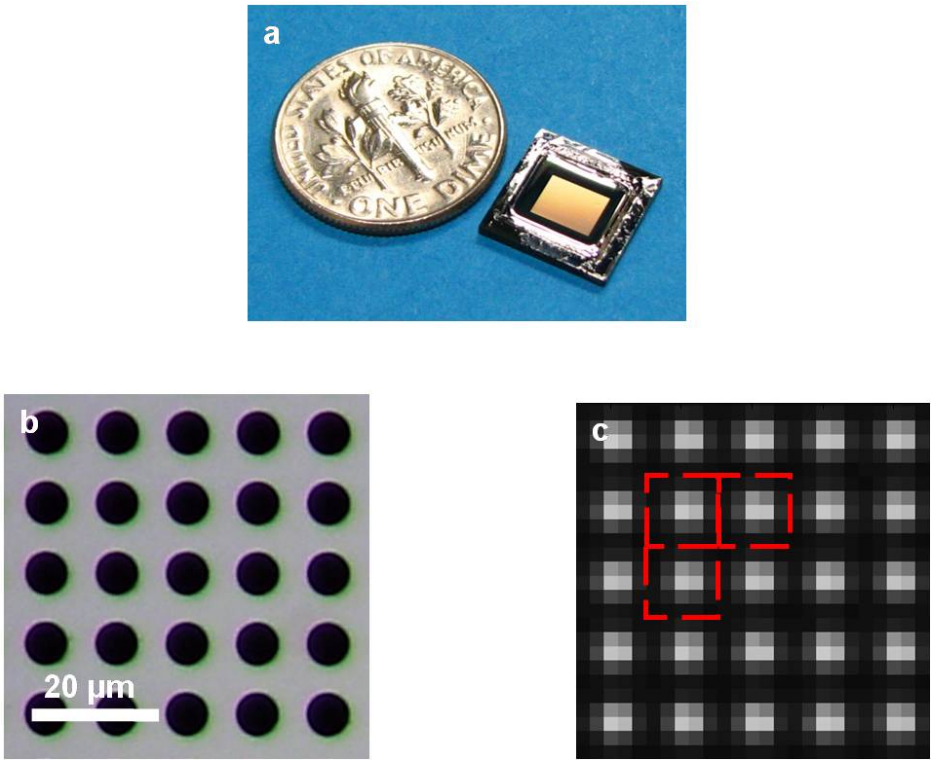

Figure 5-4 (color): WIS prototype device. (a) The fully integrated WIS is the size of a dime. **(b)** Apertures with 6 μm diameter and 11 μm spacing on a WIS. **(c)** A dedicated grid of 5×5 sensor pixels (the red dashed boxes) was assigned to each aperture projection.

We assigned a dedicated grid of 5×5 sensor pixels (Fig. 5-4 (c)) underneath each aperture to detect the associated projection spot. Because the precision of estimating the position of a light spot on a grid of sensor pixels is photon-shot noise limited (see Chapter 7), the local slope sensitivity of our WIS is also capped by the total number of captured

photons. Due to the small full-well-depth of the CMOS image sensor used in this prototype device (a maximum number of 10k photoelectrons can be stored in each sensor pixel), we need to integrate multiple frames of snap shots to accumulate data of high quality. Throughout the experiments in the Chapter 5 and 6, 100 frames of snap shots with a 10 ms exposure time for each snap shot were integrated. The typical light intensity on the sensor is 9.2 $\mu W/cm^2$.

The total detected signal summed over the pixel grid is a measure of the light intensity incident on the aperture. The lateral shifts of the projection spot are related to the normalized phase gradient of the incident light. We employed the algorithm described in the next section (Section 5.5) to determine the lateral shifts with sub-pixel accuracy. By assuming the effective refractive index of the entire stack of the SU8 and proprietary materials is 1.6, we estimated that the distance H from the aperture to the actual photosensitive area of the image sensor was (28±1) μm (Section 5.6). This configuration generated smoothly focused aperture projections on the image sensor, and enabled good performance for our WIS prototype. Based on our experimental data in Section 5.3, we determined that the projection spots have diameter of 4.5 μm (FWHM) - 25% narrower than the parent apertures. The slight mismatch between our achieved and the optimal spot sizes is attributable to the fact that our fabricated effective SU8 spacer thickness was larger than expected. Nevertheless, we expected this WIS prototype to be able to perform well.

5.5 Cyclic algorithm for estimating the center of each WIS projection spot

The centroid method is the most straightforward algorithm for determining the center of each WIS projection spot. However, because the centriod method assigns significant weights to the more heavily noise-corrupted data from dark pixels, it is intrinsically an unstable position estimator. We found that a relatively new position estimation algorithm – the cyclic method, is more suitable for our purpose. This algorithm uses cyclic and uni-norm complex weights instead. To clearly illustrate its principle, we will first discuss the cyclic algorithm for the 1D case along the *s* axis. Suppose the distribution of a light spot on the image sensor is $I(s)$, concentrated in a window$[-T/2, T/2]$. We can define a complex number $\tilde{s}_0$ for its initial position:

$$\tilde{s}_0 = \int_{-T/2}^{T/2} I(s)\exp(i\frac{2\pi}{T}s)ds\,. \tag{5-2}$$

If the center of the light spot shifts Δs, the complex number $\tilde{s}_1$ for the second position will be:

$$\begin{aligned}\tilde{s}_1 &= \int_{-T/2}^{T/2} I(s-\Delta s)\exp(i\frac{2\pi}{T}s)ds \\ &= \int_{-T/2-\Delta s}^{T/2-\Delta s} I(u)\exp(i\frac{2\pi}{T}(u+\Delta s))du \\ &= \exp(i\frac{2\pi}{T}\Delta s)\int_{-T/2-\Delta s}^{T/2-\Delta s} I(u)\exp(i\frac{2\pi}{T}u)du \\ &\approx \exp(i\frac{2\pi}{T}\Delta s)\tilde{s}_0\end{aligned}\,. \tag{5-3}$$

The last approximation is true when $\Delta s << T$, which is usually the case for WM. We can see that $\tilde{s}_1$ is nothing but $\tilde{s}_0$ rotated by an angle $\frac{2\pi}{T}\Delta s$ in the complex plane, so the shift of the light spot can be easily calculated from the above two complex numbers.

$$\Delta s = \frac{T}{2\pi}[angle(\tilde{s}_1) - angle(\tilde{s}_0)] \tag{5-4}$$

For the discrete data from the 2D image sensor pixels, we assigned a dedicated grid of 5×5 sensor pixels (Fig. 5-4 (c)) (the horizontal and vertical indexes of the pixels are m = -2, -1, 0, 1, 2 and n = -2, -1, 0, 1, 2, respectively) underneath each aperture to measure the shift of the light spot, and we replaced the integrals in Eq. (5-2) – (5-4) with summations:

$$\begin{aligned}
\tilde{s}_0 &= \sum_{m=-2,n=-2}^{2}\sum^{2} I_{mn}(s)\exp(i\frac{2\pi}{5}n) \\
\tilde{s}_1 &= \sum_{m=-2,\ n=-2}^{2}\sum^{2} I_{mn}(s-\Delta s)\exp(i\frac{2\pi}{5}n)\,. \\
\Delta s &= \frac{5}{2\pi}[angle(\tilde{s}_1) - angle(\tilde{s}_0)]
\end{aligned} \tag{5-5}$$

There might be some bias introduced by this simple replacement. However, this bias can be corrected with careful calibrations (see the next section).

5.6 Calibration experiment for the normalized phase gradient measurement

In order to test the linearity and sensitivity of our WIS, we introduced a specific normalized phase gradient to all of the WIS apertures (Fig. 5-5 (a, b)) by illuminating them with a plane halogen light at different incident angles. Figure 5-5 (c, d) shows good linearity of the normalized phase gradient responses in both the x and y directions over a range of +/-15 mrad. This range is adequate in addressing our microscopy application needs. If desired, our WIS prototype is capable of measuring phase gradients over a broader range as long as we collect a more extended set of calibration data. Each data point is the average normalized phase gradient measurement from the 350 apertures of the central row of our WIS; each error bar corresponds to the standard deviation among them. This normalized phase gradient variation between apertures is ~ 0.5 mrad.

From the slopes of the calibration curves, we can estimate the distance from the aperture of our WIS to the photo-sensitive area of the optical sensor chip. They are 27.2 μm and 28.0 μm in the x and y directions respectively, assuming the effective refractive index of the whole stack of the SU8 and proprietary materials is 1.6. The discrepancy between these two numbers might be due to the slight aperture-pixel misalignment in the x and y directions.

From the fluctuation of each aperture projection spot over time, we estimate that the sensitivity of our normalized phase gradient measurement is better than 0.1 mrad under the typical working condition - 1.0 second total signal accumulation time and 9.2 $\mu W/cm^2$ light intensity on the sensor.

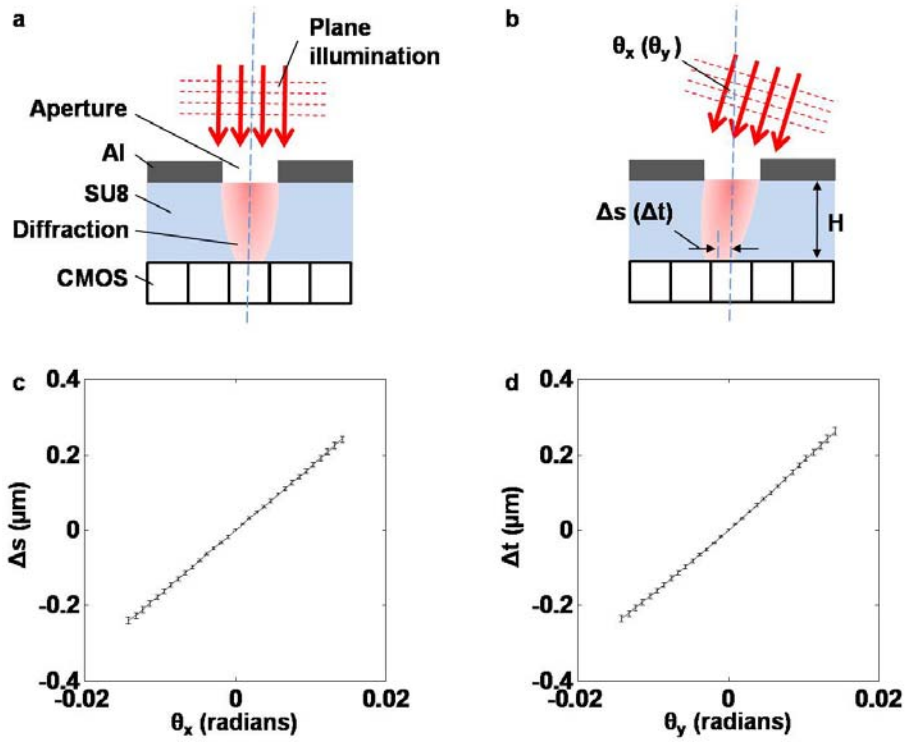

Figure 5-5 (color): Calibration experiment for normalized phase gradient measurements using a WIS. (a, b) The experiment setup under vertical illumination and tilted illumination, which imposed a specific normalized phase gradient θ_x or θ_y to the WIS. **(c, d)** the normalized phase gradient responses of the WIS in both x and y directions. Each data point is the average normalized phase gradient measurement from the 350 apertures of the central row of our sensor; each error bar corresponds to the standard deviation among the apertures.

5.7 Discussion

The added phase front sensing ability of the WIS does come at a price – we sacrifice the number of image pixels that a sensor possesses for the added ability. Fortunately, today's image sensors have an abundance of pixels and are, in fact, reaching a point where the number of pixels exceeds the number of useful resolvable image points that the associated optical system can deliver. The consolidation of these sensor pixels and corresponding reduction in the number of useful image pixels to add phase front sensing ability is therefore a worthy trade-off.

The WIS necessarily collects less light than a normal optical sensor chip as only a fraction of the total incident light will transmit through the aperture sieve – for our prototype, ~ 23% of the light is transmitted by the aperture sieve. Our particular prototype has an additional loss mechanism – the nullification of the lens above each sensor pixel prevents efficient channelling of the light to the actual sensing area of each pixel. This loss mechanism can be eliminated in future WIS designs by allowing that lenslet grid to be preserved during the fabrication process.

The low photon counts and poor signal-to-noise ratio (SNR) at the edge pixels in the pixels window (Fig. 5-4 (c)) under each WIS aperture prohibit us from rendering high-quality normalized phase gradient images with a single snap shot. In the proof-of-concept experiment, we integrated 100 frames to achieve spatial normalized phase gradient images with good SNR. In theory, with a 10 ms exposure time for each snap shot (commonly used in this study), the entire data acquisition process can be reasonably short (1 second). However, because of the limitation of the CMOS sensor and the slow readout

speed of the camera, it took us ~20 seconds to finish the data accumulation. We propose two ways to solve this problem.

First, we can use an on-chip image adder in the CMOS image sensor to do the signal accumulation, and output only one frame of the final image data at the end of process. Because there is no heavy data transfer involved, the entire data acquisition will be exposure time limited.

Second, from the photon counting point of view, taking 100 snap shots with 10 ms exposure for each snap shot is equivalent to taking 1 snap shot with a 1 second exposure. Thus, if we use a long enough exposure time, we can achieve reasonable SNR for the edge pixels in the pixels window. Of course, this will saturate the other pixels in the window because of the large number of photons collected. This can be solved easily by taking another snap shot with a shorter exposure time. If there are still saturated pixels, repeat the previous step until all pixels are appropriately exposed. At the end, the high-quality data for normalized phase gradient estimation can be obtained by assembling the snap shots normalized by the different exposure times. Depending on the number of pixels in the window, we can use 3~5 snap shots with decreasing exposure times to achieve the same data quality as in this preliminary study. And the total data acquisition time can be controlled in seconds.

Since the WIS is fully capable of capturing light intensity variations, it can serve as a direct camera chip replacement in other applications as well. A camera that can image wavefront is potentially useful in adaptive optics, machine recognition (For determining if a corner is pointed in or out), texture assessment, and object ranging. Amongst other applications in the medical field, this technology can significantly impact

LASIK surgery and high-resolution retinal imaging. As the cost for transforming a standard image sensor into a WIS is incremental on the foundry level, this is a low-cost and compact wavefront sensor that can address new applications for which the current wavefront sensing standard, the Hartmann-Shack sensor, is simply too costly and bulky to contemplate.

Finally, it is worth noting that the incorporation of the WIS functionality into a color sensor can be accomplished by starting with a substrate sensor chip that has stratified color sensing sites (such as Foveon X3). The implementation is straight forward in this case. A WIS capable of color sensing can also be built with the conventional color sensors that employ Bayer color pixel arrangements, as long as more sophisticated projection spot localization algorithms are developed. The development of such sensors will simplify camera choice for a microscopist – with the WIS functionality and color imaging capability on the same sensor, a microscopist would not need to switch between different cameras to collect phase-gradient and color images.

5.8 Conclusion

We have created a WIS with high sampling density in the high Fresnel number regime, which is capable of simultaneously measuring both the amplitude and phase front of complicated light fields in biological imaging. It not only enables the wavefront microscopy (see next chapter), but also promises broad applications in adaptive optics, LASIK surgery, machine recognition, texture assessment, and object ranging.

Bibliography

1. B. C. Platt, and R. Shack, "History and principles of Shack-Hartmann wavefront sensing," Journal of refractive surgery **17**, S573-S577 (2001).
2. R. V. Shack, and B. C. Platt, "Production and use of a lenticular hartmann screen," Journal of the Optical Society of America **61**, 656-& (1971).
3. X. Q. Cui, M. Lew, and C. H. Yang, "Quantitative differential interference contrast microscopy based on structured-aperture interference," Applied Physics Letters **93**, 3 (2008).
4. E. Betzig, G. H. Patterson, R. Sougrat, O. W. Lindwasser, S. Olenych, J. S. Bonifacino, M. W. Davidson, J. Lippincott-Schwartz, and H. F. Hess, "Imaging intracellular fluorescent proteins at nanometer resolution," Science **313**, 1642-1645 (2006).
5. M. J. Rust, M. Bates, and X. W. Zhuang, "Sub-diffraction-limit imaging by stochastic optical reconstruction microscopy (STORM)," Nature Methods **3**, 793-795 (2006).

Chapter 6: Wavefront Microscopy (WM) Method

In this chapter, we will propose a new microscopy concept – wavefront microscopy (WM), which for the first time allows for quantification of both amplitude and phase information from a microscope image of biological samples simultaneously. WM provides not only an easy and cost-effective solution for researchers and clinicians to incorporate phase imaging functionality into their current microscope systems, but also allows for easier refractive index mapping of biological samples thus facilitating deep tissue imaging with multiphoton microscopy.

First we will demonstrate how to convert a standard microscope into a WM by simply attaching the wavefront image sensor (WIS) (see Chapter 5) onto the camera port of the microscope. Then we will report the use of WM for biological imaging, including an unstained live nematode, a stained *ascaris* under cell division, and a strongly birefringent ctenoid fish scale. Next, we will then discuss some fundamental properties of WM and other useful phase representations allowed by WM. Finally, we will conclude by discussing the potential applications of WM in biomedical research.

6.1 Background

An optical microscope reveals abundant information about the structure and composition of a specimen through the variation of light waves. However, because human eyes and most image sensors are only sensitive to light intensity, the dominating optical microscope techniques, e.g., bright field and fluorescent microscopes, record only partial information from the light wave – the amplitude.

Measuring the phase of the light wave is important in bioscience as well; optical phase microscopes are greatly valued for their ability to render contrast based on refractive index variations in biological samples. For example, phase microscopes are useful in biomedical applications where minimal specimen preparation procedures are required. Such applications can include field analysis of blood- and water-borne pathogens [1] where cost-considerations and ease-of-use are important, and analysis of biopsy sections to determine tumor margins during surgical procedures where rapid processing is critical [2]. Phase microscopes are also useful in scenarios where staining is undesired or simply not an option. Such applications include examinations of live oocytes and embryos during in-vitro fertilization procedures [3], and longitudinal imaging of live cells or organisms [4].

Unlike the detection of the amplitude, the phase of the light wave must be converted into a detectable form to be visualized. For example, differential interference contrast (DIC) microscopes [5] and, to a lesser extent, phase contrast microscopes [6] and Hoffman phase microscopes [7] have been the primary phase microscopes of choice for the past five decades. However, phase information is mixed with amplitude information in these phase microscopy techniques. This limitation introduces ambiguities in the

rendered images and, additionally, prevents straight-forward quantitative phase analysis. Moreover, these phase microscopes require specialized optical components that must be switched in and out when changing the type of imaging mode. Additionally, DIC images of birefringent samples, such as muscle sections and collagen matrices, can have significant artifacts as the DIC microscope uses polarization in its phase-imaging strategy. The relative high cost of such systems also prevents broader usage of such phase microscopes. In recent years, numerous novel phase microscopy techniques have been developed [8-10]. However, their need for laser sources and relatively high levels of sophistication has thus far impeded their broad adoption as convenient and viable replacements for DIC microscopes. Quantitative optical phase [11] can also be calculated by collecting 2 or 3 successive images of the specimen around its focal plane. However, this technique requires the physical actuation of the camera to distinct positions, and is therefore intrinsically limited in speed.

Here we propose a new microscopy method – wavefront microscopy (WM), which can capture both the amplitude and phase information of the light wave separately, and generate quantitative bright-field and normalized phase gradient images of the specimen simultaneously. Our experiments further demonstrate that the normalized phase gradient images are improved versions of DIC microscope images in that they are artifact-free and quantitative. Another significance of our approach is that we can turn most optical microscope systems into WMs by simply placing a WIS at the camera port of the microscopes. Therefore, WM is a low-cost, easy-to-use solution to provide comprehensive microscopy information. We envision that it will generate a revolutionary impact on the biological imaging.

6.2 Wavefront microscope prototype

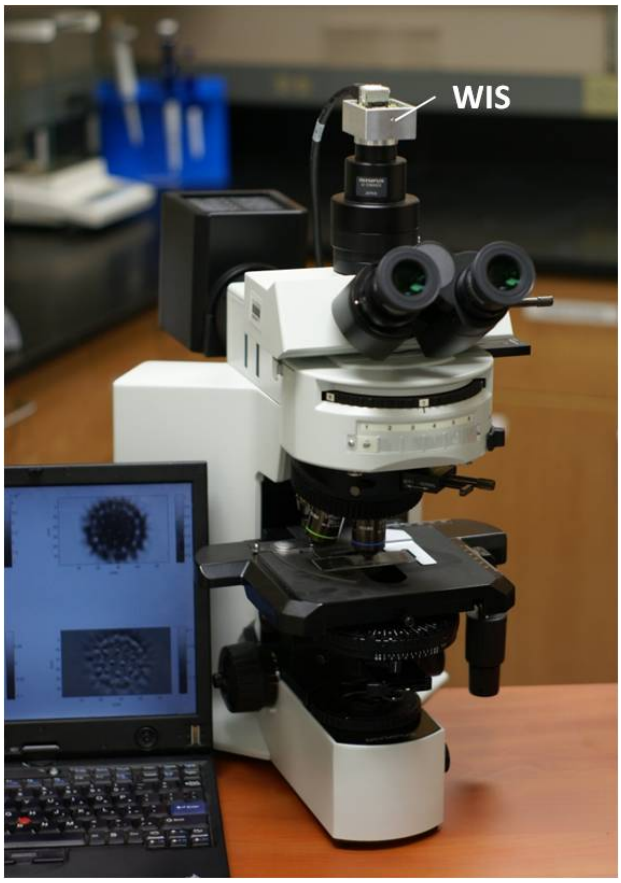

Figure 6-1 (color): WM prototype. Converting a standard optical microscope into a WM by simply adding a WIS to the camera port.

To demonstrate that we can indeed convert a standard microscope into a WM, we housed the prototype WIS device in a specially-machined C-mount compatible unit and attached it to an Olympus BX 51 microscope via its camera port (Fig. 6-1). The microscope was outfitted with a standard halogen microscope light source. We also equipped the microscope with push-in DIC prisms and polarizers, so that the microscope

could be easily reconfigured into a DIC microscope for comparison. We used a CMOS image sensor of size 9.9 μm pixels (MT9V403C12STM from Micron technology, Inc.) to record the DIC images. This allowed for a fair comparison of the image quality as the effective image pixel size of our WIS device is 11 μm. We noted that such a microscope operating with a 40×, *N.A.* = 0.75 objective has a resolution of 0.49 μm. As the microscope magnifies the image, it projects on its camera by the magnification factor. This implies that the image pixel on the sensor need only be 10 μm or smaller to enable the microscope to achieve its specified resolution (Nyquist sampling criterion consideration). The specifications of the standard CMOS sensor and our WIS device satisfied this condition.

6.3 Demonstration of WM in biological imaging

To demonstrate the potential utility of WM for a broad range of microscopy applications and to highlight its advantages over the conventional DIC microscope, we applied our prototype to image an unstained live nematode, a stained *ascaris* under cell division, and a strongly birefringent ctenoid fish scale.

6.3.1 Unstained live nematode

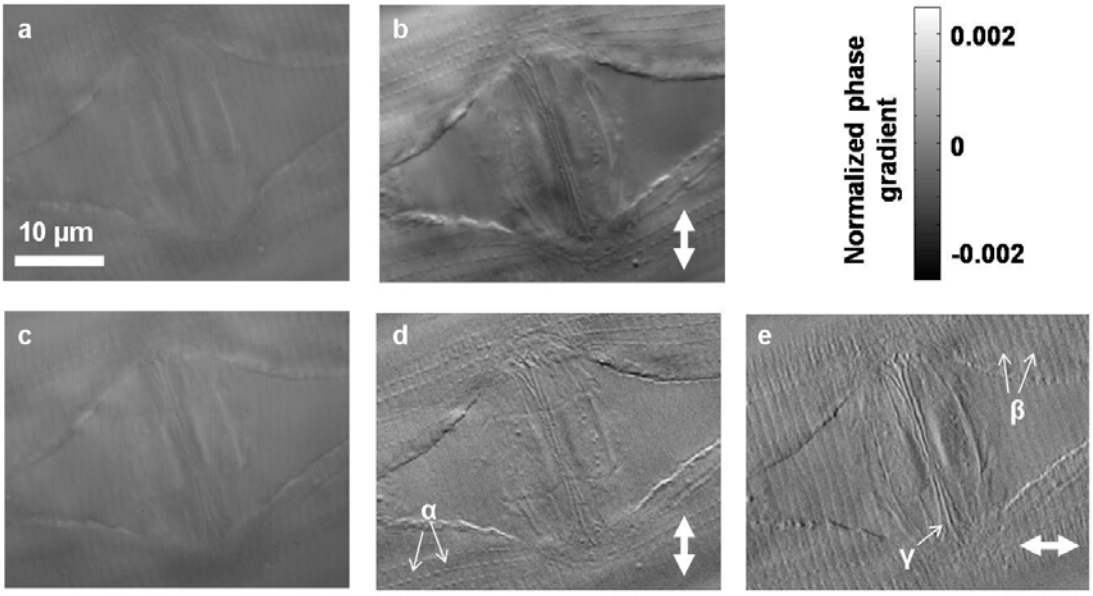

Figure 6-2: Images of an unstained wild-type hermaphrodite adult *Caenorhabditis elegans*. (a, b) Bright-field and DIC images, respectively. **(c-e)** Intensity, normalized phase gradient images from WM along *y* and *x* axes. The white arrows represent the directions of contrast enhancement. α are dense bodies, β are furrows and annuli on the skin, and γ is the vulva slit.

For our first set of experiments, we placed a wild-type hermaphrodite adult *C. elegans* (worm) on an agarose pad (2% agarose in M9 buffer) over a microscope slide, and paralyzed it with 0.6% sodium azide. The preparation was then covered with a cover slip. A 100× objective lens (*N.A.* = 1.3) and a condenser lens (*N.A.* = 0.9) were used during imaging. Figure 6-2 (a, b) are the acquired bright-field and DIC (shear direction is along *y* axis throughout the imaging experiments in this chapter) images of the worm around its vulva. Because the specimen was not stained, the DIC image provided a much better contrast than the bright-field image. Figure 6-2 (c-e) are the WM images: an intensity image (Fig. 6-2 (c)), a normalized phase gradient image along *y* axis (Fig. 6-2 (d)), and a normalized phase gradient image along *x* axis (Fig. 6-2 (e)) of the worm that are rendered from a single data acquisition. We can see that the WM intensity image is consistent with the bright-field image, and the WM *y*-directional normalized phase gradient image is consistent with the DIC image. However, the WM *x*-directional normalized phase gradient image contains phase information orthogonal to both the DIC image and our *y*-directional normalized phase gradient image, revealing different details of the worm. For example, dense bodies are clearly shown in the *y*-directional normalized phase gradient image, while the vulva slit and furrows and annuli on the skin are more obvious in the *x*-directional normalized phase gradient image.

6.3.2 Stained *ascaris* under cell division

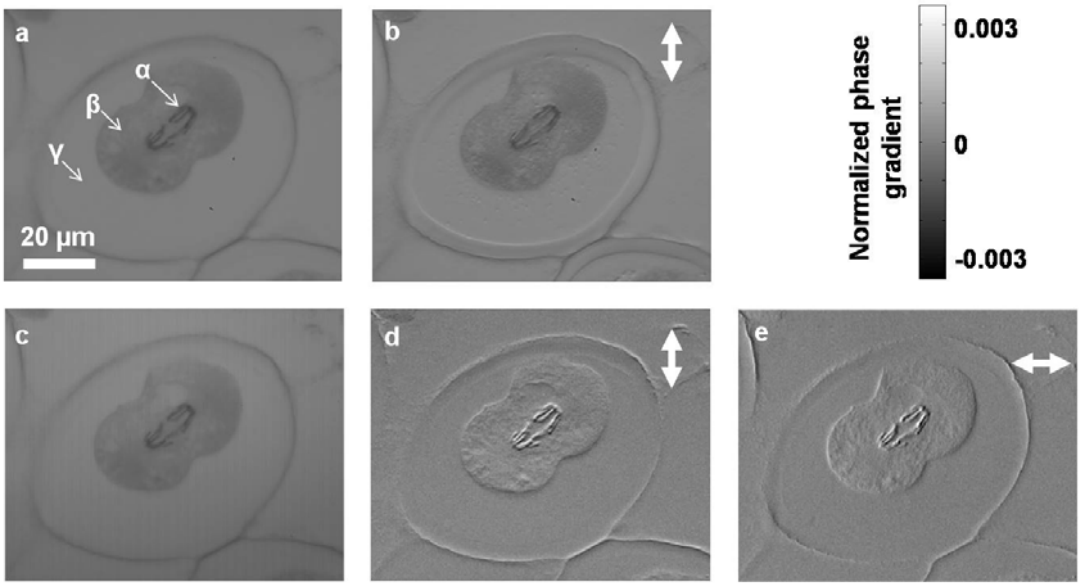

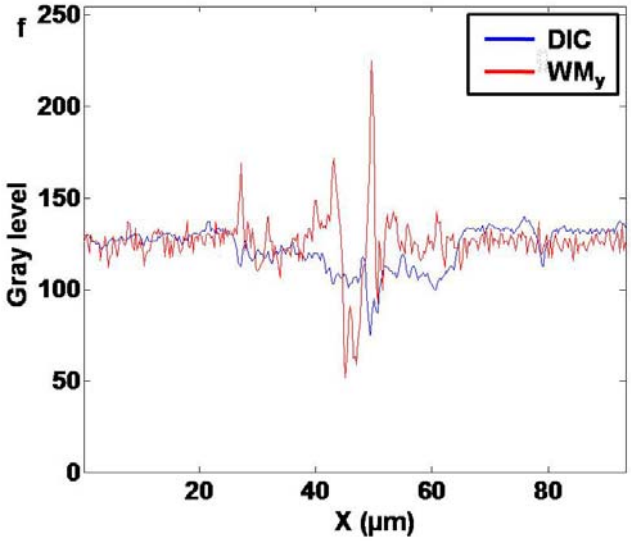

Figure 6-3: Images of a stained *ascaris* under cell division. (a, b) Bright-field and DIC images, respectively. **(c-e)** Intensity, normalized phase gradient images along *y* and *x* axes of WM, respectively. **(f)** The reduction of the amplitude caused by the chromosome

staining mixes with the phase information in the DIC images (the blue line profile), whereas the normalized phase gradient image of WM can separate out the pure phase information (the red line profile). The white arrows represent the directions of contrast enhancement. α are chromosomes, β is nucleoplasm, and γ is cytoplasm.

It is well known that DIC images carry mixed amplitude and phase information of the specimen image [12]. As such, stained specimens can generate ambiguous DIC images where a dark spot in the images may be attributable to an absorption site or a location where the normalized phase gradient has a large negative value. In this second set of experiments, we imaged an *ascaris* undergoing cell division (fixed by 10% formalin and stained with hematoxylin) to demonstrate the advantage of WM over DIC microscope in imaging stained specimens. The stained chromosomes of the *ascaris* appear as dark regions in both the bright-field (Fig. 6-3 (a)) and DIC image (Fig. 6-3 (b)). If the DIC microscope is a pure phase imager, we would have expected one edge of the chromosome clump to appear brighter and the other edge to appear darker (chromosomes are optically denser than the nucleoplasm). The average brightness should remain the same as the background. The WM rendered relief-like normalized phase gradient image (Fig. 6-3 (d, e)), which is a signature of a correct phase gradient image. The comparison of the line profiles (Fig. 6-3 (f)) from the DIC and WM phase gradient image further highlights the difference. The DIC trace has an obvious signal dip in the middle that is attributable to light absorption by the stain, while such a dip is absent from the WM trace. Additionally, the bright-field and WM intensity images (Fig. 6-3 (a, c)) are very similar

in appearance. A 40× objective lens (*N.A.* = 0.75) and a condenser lens (*N.A.* = 0.5) were used during imaging.

6.3.3 Birefringent ctenoid fish scale

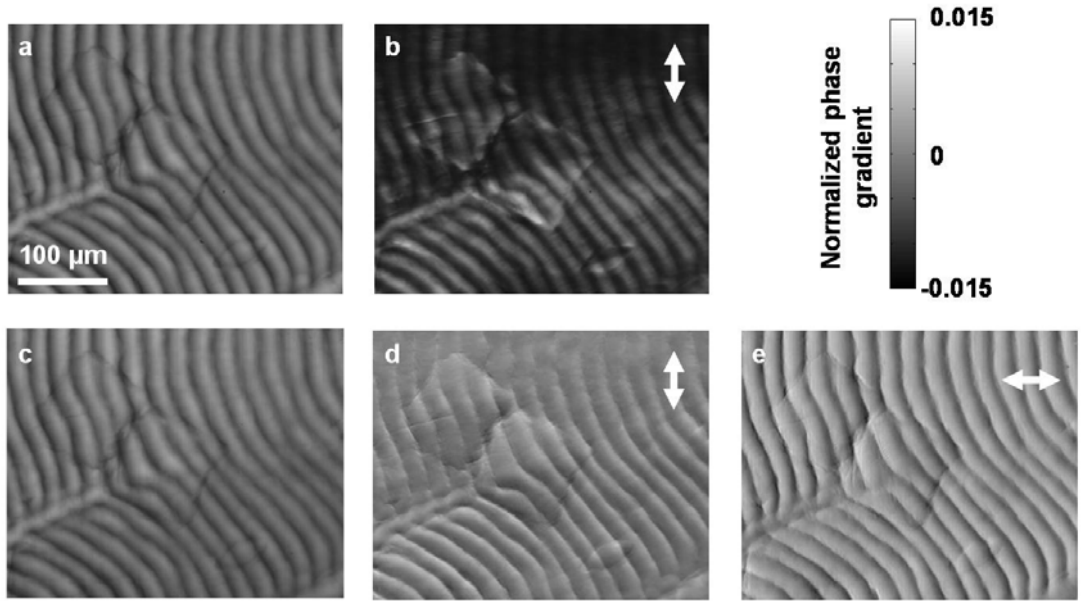

Figure 6-4: Images of a ctenoid scale from a fresh *striped bass*. (a) Bright-field image **(b)** DIC image with strong birefringent artifact. **(c-e)** Intensity, and artifact-free normalized phase gradient images from WM along *y* and *x* axes, respectively. The white arrows represent the direction of contrast enhancement.

Many biological specimens, such as muscle tissues and collagen matrices, show strong birefringence properties due to their asymmetrical structural arrangements. DIC microscopy generates severe artifacts when imaging a birefringent specimen; this is because the difference in refractive indices along orthogonal axes of the specimen

disrupts the necessary polarization conditions in the DIC microscope [13-14]. WM does not rely on the manipulation of the polarized light for its phase imaging ability and, as such, we can expect WM to image birefringent specimens well. In this third set of experiments, we imaged a ctenoid fish scale (from a fresh striped bass, held in 1× PBS solution between the microscope slide and cover slip), which is known to be birefringent. A 10× objective lens (*N.A.* = 0.3) and a condenser lens (*N.A.* = 0.2) were used during imaging. As with our other experiments, the bright-field (Fig. 6-4 (a)) and WM intensity (Fig. 6-4 (c)) images are consistent with each other. However, the severe birefringence artifacts in the DIC image hindered the viewing of fine structures on the fish scale (Fig. 6-4 (b)). In contrast, our WM did not generate birefringent artifacts, and the square and diamond shaped structures are clearly revealed in the normalized phase gradient images (Fig. 6-4 (d, e)).

6.4 Discussion

6.4.1 Resolution, sampling and point spread function of WM

The lateral resolution of WM is still limited by the *N.A.* of the objective lens. However, as with other digital imaging techniques, decreasing the aperture spacing of the WIS could reduce aliasing in the digitized image (see Chapter 3). We can use an image sensor with smaller pixels (e.g., the 1.67 μm CMOS image sensor from Aptina Imaging) to further reduce the aperture spacing.

The size and shape (e.g., the four-hole aperture in Chapter 4) of the aperture are related to the point spread function (PSF) of the total WM microscope system, so they

could be parameters tailored towards different imaging applications. For example, we can see that the normalized phase gradient images of our WM (Fig. 6-2 (d, e) are sharper than the DIC images (Fig. 6-2 (b)). This might be because the small apertures in the WIS can screen out more background light than the big and less-defined pixels in a conventional image sensor.

6.4.2 Other quantitative phase representations

The phase of a light wave is a fixed scalar potential function, so our two orthogonal normalized phase gradient θ_x and θ_y images are a complete set of the phase gradient information of the specimen. This complete information can be represented in several forms that may be more amenable to the specific needs of doctors or bio-scientists.

For example, we can enhance the contrast of the differential phase image of the specimen along any direction $\vec{n}$ by simply taking the inner product of the unit direction vector $\vec{n}$ and the spatial normalized phase gradient vector $\vec{\theta} = \theta_x \vec{i} + \theta_y \vec{j}$. In conventional DIC microscopy, this can only be done by bringing the specimen back to the DIC microscope and performing another measurement after rotating the DIC prisms.

Furthermore, the magnitude of the normalized phase gradient vector, $\left|\vec{\theta}\right| = \sqrt{\theta_x{}^2 + \theta_y{}^2}$, highlights the boundaries of the specimen, where the phase changes dramatically. Its map can be very useful for applications such as automatic segmentation and counting of cells or other subcellular organelles. This map is also

objective, as it is not dependent on the relative orientation of the specimen to the imaging axis of the DIC microscope.

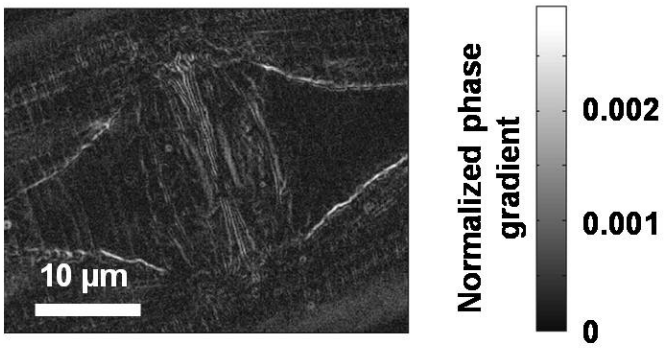

Figure 6-5: Normalized phase gradient vector magnitude image of an unstained wild-type hermaphrodite adult *C. elegans.* This image corresponds to the image set in Fig. 6-2.

Sometimes representing the normalized phase gradient vector $\vec{\theta} = \theta_x \vec{i} + \theta_y \vec{j}$ in its vector form can be enlightening as well. For example, Figure 6-6 (a, b) shows the normalized phase gradient vector plots (blue arrows) of a transparent polystyrene microsphere. From the direction of the vectors, we can observe how the normalized phase gradient changes across the specimen wavefront. In Figure 6-6 (a), the converging normalized phase gradient vectors correspond to the change of the normalized phase gradient when the focal plane is at the bottom of the microsphere. In Figure 6-6 (b), the diverging normalized phase gradient vectors represent the case when the focal plane is at the top of the microsphere. In contrast, the gray level images of the magnitude of the normalized phase gradient vector $\left|\vec{\theta}\right| = \sqrt{\theta_x{}^2 + \theta_y{}^2}$ in the background of Figure 6-6 (a, b)

look similar for both cases, and they do not tell us if the wavefront is bending in or popping out.

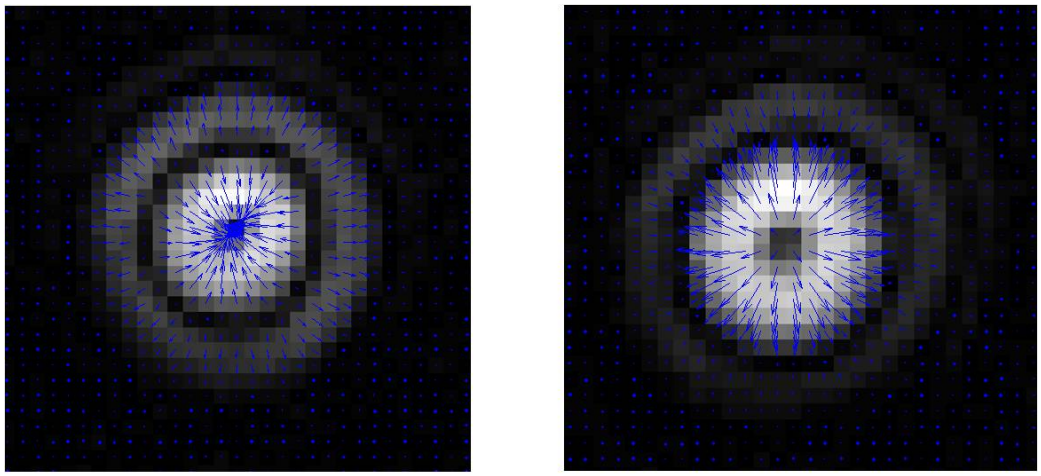

Figure 6-6 (color): Normalized phase gradient vector plot of a polystyrene microsphere. (a) The converging normalized phase gradient vectors correspond to the change of the phase delay when the focal plane is at the bottom of the microsphere. **(b)** The diverging normalized phase gradient vectors represent the case when the focal plane is at the top of the microsphere.

6.5 Conclusion and potential applications

We demonstrated that we can transform a standard microscope into a WM. WM provides not only standard bright-field images, but also can provide quantitative normalized phase gradient images. These images are improvements over standard DIC images in that 1)

they are quantitative, 2) immune to birefringence-generated artifacts, 3) they clearly separate the amplitude and phase information of a light field.

The ability to perform quantitative and pure phase imaging is useful in numerous applications. For example, we can use this ability to quantify the optical thickness of cells or organelles [15], and to determine the chemical concentration in a microfluidic system [16]. Currently, performing such measurements requires fairly sophisticated and well-designed interferometer schemes. WM provides an alternate approach that is simple to set up and easy to use.

Immunity from the birefringence artifacts can broaden the use of phase microscopy for examining tissues in-situ. For example, an endoscopic format of WM can be used in examining muscle, cartilage, tendon, and other collagen-rich tissues during surgery.

In a practical context, most standard optical microscope systems can be turned into a WM without any major modification. It provides an easy and cost-effective solution for researchers and clinicians to incorporate phase imaging functionality into their current microscope systems, and may allow for specialized phase microscopy techniques to become available to average microscopists and even high school students. The usage of WM can further include correction of the aberration generated by the heterogeneity of tissue specimens via adaptive optics strategies to facilitate deep tissue imaging of multiphoton microscopy [17-18].

Last, the concept of WM can be applied across the spectrum of electromagnetic waves other than the visible light. For example, WM in the X-ray range regime could

measure the directions of X-ray photons bent by the specimen, and reveal distinct contrast from conventional techniques [19].

Bibliography

1. S. L. Stanley, "Amoebiasis," Lancet **361**, 1025-1034 (2003).
2. M. M. Haglund, M. S. Berger, and D. W. Hochman, "Enhanced optical imaging of human gliomas and tumor margins," Neurosurgery **38**, 308-317 (1996).
3. J. Vanblerkom, H. Bell, and G. Henry, "The occurrence, recognition and developmental fate of pseudo-multipronuclear eggs after in-vitro fertilization of human oocytes," Hum. Reprod. **2**, 217-225 (1987).
4. R. J. Sommer, and P. W. Sternberg, "Changes of induction and competence during the evolution of vulva development in nematodes," Science **265**, 114-118 (1994).
5. G. Nomarski, "New theory of image formation in differential interference microscopy," Journal of the Optical Society of America **59**, 1524-& (1969).
6. F. Zernike, "Phase contrast, a new method for the microsopic observation of transparent objects," Physica **9**, 686-698 (1942).
7. R. Hoffman, and L. Gross, "The modulation contrast microscope," Nature **254**, 586-588 (1975).
8. P. Marquet, B. Rappaz, P. J. Magistretti, E. Cuche, Y. Emery, T. Colomb, and C. Depeursinge, "Digital holographic microscopy: a noninvasive contrast imaging technique allowing quantitative visualization of living cells with subwavelength axial accuracy," Optics Letters **30**, 468-470 (2005).
9. W. Choi, C. Fang-Yen, K. Badizadegan, S. Oh, N. Lue, R. R. Dasari, and M. S. Feld, "Tomographic phase microscopy," Nature Methods **4**, 717-719 (2007).
10. M. V. Sarunic, S. Weinberg, and J. A. Izatt, "Full-field swept-source phase microscopy," Optics Letters **31**, 1462-1464 (2006).
11. A. Barty, K. A. Nugent, D. Paganin, and A. Roberts, "Quantitative optical phase microscopy," Optics Letters **23**, 817-819 (1998).
12. M. R. Arnison, K. G. Larkin, C. J. R. Sheppard, N. I. Smith, and C. J. Cogswell, "Linear phase imaging using differential interference contrast microscopy," Journal of Microscopy-Oxford **214**, 7-12 (2004).
13. X. Q. Cui, M. Lew, and C. H. Yang, "Quantitative differential interference contrast microscopy based on structured-aperture interference," Applied Physics Letters **93**, 3 (2008).
14. S. B. Mehta, and C. J. R. Sheppard, "Quantitative phase-gradient imaging at high resolution with asymmetric illumination-based differential phase contrast," Optics Letters **34**, 1924-1926 (2009).
15. G. Popescu, T. Ikeda, R. R. Dasari, and M. S. Feld, "Diffraction phase microscopy for quantifying cell structure and dynamics," Optics Letters **31**, 775-777 (2006).
16. J. G. Wu, Z. Yaqoob, X. Heng, L. M. Lee, X. Q. Cui, and C. H. Yang, "Full field phase imaging using a harmonically matched diffraction grating pair based homodyne quadrature interferometer," Applied Physics Letters **90**, 3 (2007).

17. M. J. Booth, M. A. A. Neil, R. Juskaitis, and T. Wilson, "Adaptive aberration correction in a confocal microscope," Proceedings of the National Academy of Sciences of the United States of America **99**, 5788-5792 (2002).
18. M. Rueckel, J. A. Mack-Bucher, and W. Denk, "Adaptive wavefront correction in two-photon microscopy using coherence-gated wavefront sensing," Proceedings of the National Academy of Sciences of the United States of America **103**, 17137-17142 (2006).
19. F. Pfeiffer, T. Weitkamp, O. Bunk, and C. David, "Phase retrieval and differential phase-contrast imaging with low-brilliance X-ray sources," Nature Physics **2**, 258-261 (2006).

Chapter 7: Fundamental Analysis of Wavefront Microscopy (WM) and Wavefront Image Sensor (WIS)

In this chapter, we will model both the wavefront image sensor (WIS) and wavefront microscopy (WM) systems to understand them quantitatively and discuss their fundamental limitations on detecting the amplitude and phase of a light wave.

We will start by answering the basic question, “Can we measure both the amplitude and phase of a light wave in the microscope system accurately at the same time?” To do this, we will re-examine the signal and system model of the conventional microscope. Then, we will analyze the wavefront imaging process in a microscope, and discuss the reduction of the normalized normalized phase gradient upon magnification, the calculation of phase from phase gradient, and the imaging depth in a WM system. Next, we will formalize the noise characteristics of the WIS. After that, we will discuss the normalized phase gradient estimation of the WIS and introduce a potentially useful estimation method in the frequency domain. Finally, we will conclude this chapter with a discussion of our findings.

7.1 Wavefront measurement in a microscope

7.1.1 Generalized microscope imaging model for wavefront microscopy

In the conventional signal and system model of microscope imaging (Section (1.1.2)), we assumed that the object function $f(u)$ is a real function that represents the light intensity (or the amplitude) distribution on the object. However, as we know, light contains both the amplitude and phase information, so it is more accurate to describe the object as a complex function $\tilde{f}(u)$ (the electrical field of the light emitted by the object). The more general model for the entire microscope imaging process is now:

$$\tilde{f}(u) \otimes \tilde{h}(u) = \tilde{i}(u) \tag{7-1}$$

$$\tilde{F}(f) \bullet \tilde{H}(f) = \tilde{I}(f), \tag{7-2}$$

where $\tilde{f}(u)$, $\tilde{h}(u)$, and $\tilde{i}(u)$ are the complex object, microscope, and image functions in space, respectively, and $\tilde{F}(f)$, $\tilde{H}(f)$, and $\tilde{I}(f)$ are the complex object, microscope, and image functions in frequency, respectively.

Can we measure both the amplitude and phase of a wavefront in a microscope accurately at the same time? The generalized model for microscope imaging in the frequency domain (Fig. 7-1) can be used to answer this question.

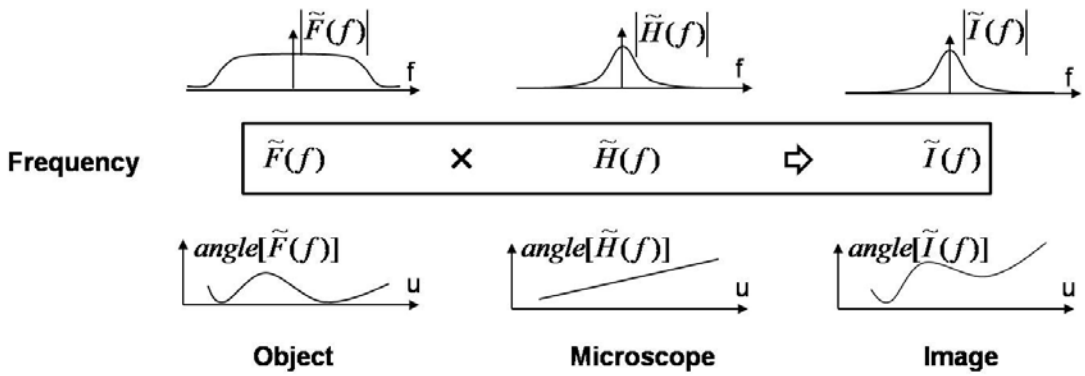

Figure 7-1: Generalized signal and system model for WM in the frequency domain.

The complex image function $\tilde{I}(f)$ is the product of the object function $\tilde{F}(f)$ and the transfer function of the microscope $\tilde{H}(f)$. Thus, the microscope system shapes the amplitude of the object spectrum $\left|\tilde{F}(f)\right|$ according to its transfer function $\left|\tilde{H}(f)\right|$ to form the amplitude of the image spectrum $\left|\tilde{I}(f)\right|$, and adds an additional phase $angle[\tilde{H}(f)]$ to phase of the object spectrum $angle[\tilde{F}(f)]$ to form the angle of the image spectrum $angle\left[\tilde{I}(f)\right]$.

When we use a microscope system to image an object wavefront, the microscope system will shape the amplitude of the object spectrum $\left|\tilde{F}(f)\right|$ according to its filter function $\left|\tilde{H}(f)\right|$ to form the amplitude of the image spectrum $\left|\tilde{I}(f)\right|$, and add an additional phase $angle[\tilde{H}(f)]$ to phase of the object spectrum $angle[\tilde{F}(f)]$ to form the angle of the image spectrum $angle\left[\tilde{I}(f)\right]$. Since the microscope system is fixed, we can always either calculate or measure the transfer function of the microscope, $\tilde{H}(f)$.

Therefore, we can remove it from the image spectrum $\tilde{I}(f)$, and obtain the object spectrum $\tilde{F}(f)$. The amplitude and phase of the measured object wavefront $\tilde{f}(u)$ are simply the amplitude and angle of the inverse Fourier transform of $\tilde{F}(f)$, respectively. In our experiment, we subtracted the normalized phase gradient data from a specimen image from that with no specimen to remove the additional phase added by the optical system of the microscope (see Section 7.1.2).

The bandwidth of the microscope system still limits our ability to detect the spatial amplitude and phase change of the wavefront induced by the object. If the change of the object wavefront is too fast, the microscope cannot respond to it and the corresponding signal will be attenuated. Limited by the noise during the imaging process, we will lose the fast amplitude and phase changes (or features) across the object wavefront. In other words, the resolution of wavefront microscopy is still limited by the *N.A.* of the microscope.

Since the wavefront signal is limited by the bandwidth of the microscope system, we need a wavefront sensor with a sampling rate that doubles the bandwidth of the microscope system to adequately sample the amplitude and phase images of the wavefront. For example, a microscope operating with a 40×, *N.A.* = 0.75 objective has a resolution of 0.49 μm. As the microscope magnifies the image, it projects on its camera an image enlarged by the magnification factor. This implies that the image pixel on the sensor need only be 10 μm or smaller to enable the microscope to achieve its specified resolution (Nyquist sampling criterion consideration). Our WIS device has a spacing of 11 μm between neighboring apertures and satisfies this wavefront sampling condition.

7.1.2 Normalized phase gradient reduction by the magnification

As the microscope magnifies a wavefront by a factor of *M*, it reduces the normalized phase gradient *M* times as well. Here we provide an illustration based on the ABCD ray transfer matrix analysis.

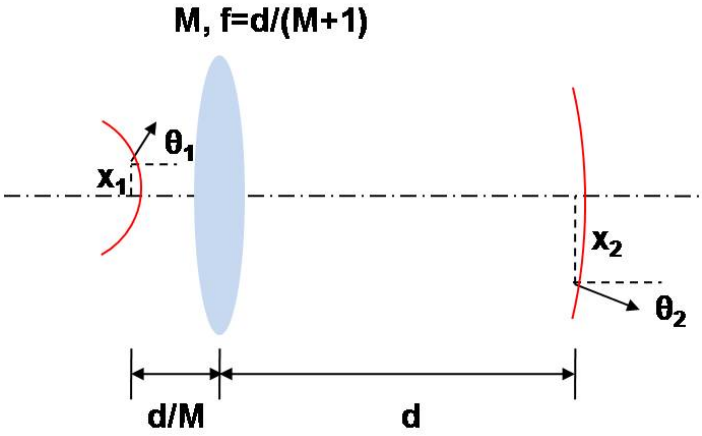

Figure 7-2 (color): Normalized phase gradient reduction by the magnification of microscope systems. In a microscope system with magnification *M*, a point x_1 on the object wavefront (the object distance is *d/M*) is projected to the point $x_2=Mx_1$ on the image wavefront (the image distance is *d*); the normalized phase gradient θ_1 at point x_1 is *M* times larger than normalized phase gradient θ_2 at point x_2.

Suppose we use an effective thin lens to model a microscope, where the magnification of the system is *M*, the image distance is *d*, the object distance is *d/M,* and the focal length of the lens is *f=d/(M+1)* (Fig. 7-2). A point x_1 on the object wavefront will be projected to a point x_2 on the image wavefront. If the normalized phase gradient

of the wavefront at point x_1 is θ_1, then the position x_2 and normalized phase gradient θ_2 of the wavefront at point x_2 can be calculated as:

$$\begin{pmatrix} x_2 \\ \theta_2 \end{pmatrix} = \begin{pmatrix} 1 & d \\ 0 & 1 \end{pmatrix} \begin{pmatrix} 1 & 0 \\ -\dfrac{1}{M+1} & 1 \end{pmatrix} \begin{pmatrix} 1 & \dfrac{d}{M} \\ 0 & 1 \end{pmatrix} \begin{pmatrix} x_1 \\ \theta_1 \end{pmatrix} = \begin{pmatrix} -M & 0 \\ -\dfrac{M+1}{d} & -\dfrac{1}{M} \end{pmatrix} \begin{pmatrix} x_1 \\ \theta_1 \end{pmatrix}$$
$$\Rightarrow \begin{cases} x_2 = -Mx_1 \\ \theta_2 = -\dfrac{x_1}{f} - \dfrac{1}{M}\theta_1 \end{cases} . \quad (7\text{-}3)$$

We can see that the image is magnified M times and inverted as expected. However, the normalized phase gradient at the image point is unfortunately being reduced M times and some additional contribution to the normalized phase gradient is imposed by the optical system. Another more intuitive way of explaining this effect is that although the phase between two points on the image wavefront has not been changed, the distance between them has been enlarged M times. Therefore, the normalized phase gradient on the image wavefront is reduced M times.

This finding means that when we magnify the details in an object we lose sensitivity in normalized phase gradient detection. However, it does not necessarily mean that the normalized phase gradient image under a high magnification will be poor in quality. An objective lens with high magnification typically has larger *N.A.* than lower magnification objectives, which allows higher normalized phase gradient components in the object pass through the microscope system. For example, the 10×, 40×, and 100× Olympus UPLFLN objectives have *N.A.*s of 0.3, 0.75 and 1.30 respectively. Therefore, the dynamic ranges of the normalized phase gradient images under different magnifications are almost the same.

The additional contribution to the normalized phase gradient imposed by the optical system can be removed by simply taking a reference image without the presence of the specimen, and subtracting it from the image with the specimen in place (this process has been used in the biological imaging of Chapter 6).

7.1.3 Phase gradient and phase

Since the phase of the wavefront is a scalar function, ideally it can be calculated by simply integrating the phase gradient. However, in the presence of noise, this calculation must be performed with caution. Fortunately, much research has been completed in this area, leading to the development of several approaches including the Frankot Chellappa algorithm [1], the Poisson surface reconstruction [2], the affine transformations [3], and the iterative Fourier transform [4].

7.1.4 Depth of field

WM uses apertures to collect light effectively blocking out-of-focus light. As demonstrated in Figure 7-3, the in-focus light can pass through the aperture and efficiently be detected by the image sensor, whereas the out-of-focus light will form a blob around the aperture and that will mostly be blocked by the metal film on the WIS. This is very similar to the case of a conventional microscope system (the physical size of the image sensor pixels are acting as the apertures in the WIS), with depth of field is given by [5]:

$$d_{dof} = \frac{\lambda_0 n}{N.A.^2} + \frac{n}{M \bullet N.A.} e, \tag{7-4}$$

where d_{dof} represents the depth of field, λ_0 is the wavelength of the illumination light, n is the refractive index of the medium between the coverslip and the objective lens, $N.A.$ is the numerical aperture of the objective lens, e is the aperture size, and M is the magnification of the microscope. For example, when the aperture size in a WIS is 6 μm and the illumination wavelength is 0.6 μm, the 40X objective lens with 0.75 *N.A.* will form a depth of field of 1.3 μm; the 100× oil immersion lens (n=1.3) with 1.30 *N.A.* will form a depth of field of 0.6 μm.

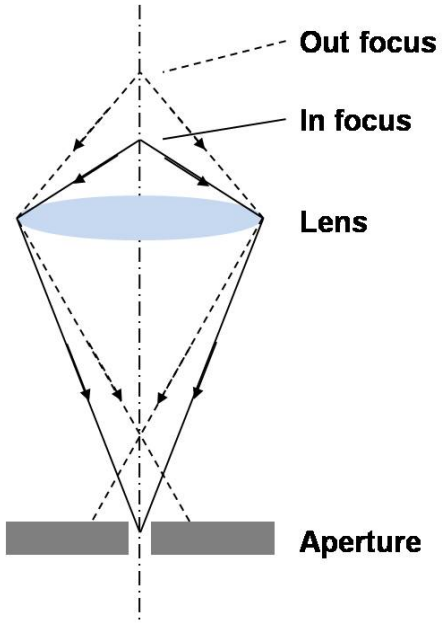

Figure 7-3 (color): Depth of field in a WM. The in-focus light can pass through the aperture and efficiently be detected by a WIS, whereas the out-of-focus light will form a blob around the aperture that is mostly blocked by the metal film on a WIS. Therefore, the depth of field of WM is limited.

7.2 Noise analysis of the amplitude and normalized phase gradient measurement in the WIS

7.2.1 Amplitude measurement

The amplitude measurement of the WIS is the same as that of a conventional image sensor, so they share the same noise characteristics. When the light intensity is high, it is the photon shot noise limited; when the light intensity is low, the electronic noises (dark noise, readout noise and 1/f noise) become dominant.

7.2.2 Normalized phase gradient measurement

The noise analysis of the normalized phase gradient measurement is more complicated. Here we will present a basic noise model based on Thompson's localization analysis [6] and the assumption of Fraunhofer diffraction in the WIS.

Thompson concluded in his paper that the precision of locating a Gaussian light spot (the projection of the WIS aperture is similar to a Gaussian distribution as well) on a pixelated and noisy image sensor can be formalized as:

$$\left\langle (\Delta x)^2 \right\rangle = \frac{s^2 + a^2/12}{N} + \frac{8\pi s^4 b^2}{a^2 N^2}, \tag{7-5}$$

where x is the location of the light spot, s is the standard deviation of the light spot distribution, a is the pixel size, b is the background noise, and N is the number of photons detected.

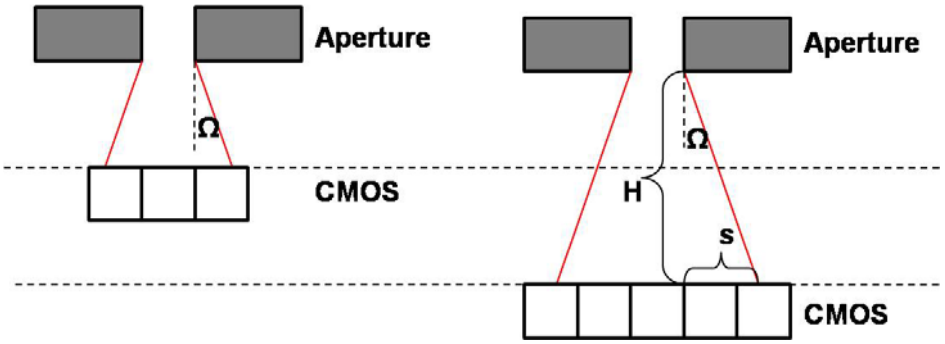

Figure 7-4 (color): Fraunhofer diffraction approximation in the WIS. Here we assume the width of the projection spot grows linearly with distance (*H*) from the aperture to the image sensor.

Noting that $x = H\theta$, we can model the precision of measuring the normalized phase gradient θ as:

$$\left\langle (\Delta\theta)^2 \right\rangle = \frac{\left\langle (\Delta x)^2 \right\rangle}{H^2} = \frac{\frac{s^2 + a^2/12}{N} + \frac{8\pi s^4 b^2}{a^2 N^2}}{H^2}. \tag{7-6}$$

Under the assumption of the Fraunhofer diffraction in the WIS (Fig. 7-4), we will have $s = H\Omega$, where H is the distance from the aperture to the image sensor, and Ω is the diffraction angle. Therefore, the noise characteristics of the normalized phase gradient measurement is

$$\left\langle (\Delta\theta)^2 \right\rangle = \Omega^2 \left(\frac{1}{N} + \frac{a^2}{12Ns^2} + \frac{8\pi s^2 b^2}{a^2 N^2} \right). \tag{7-7}$$

In general, the less the aperture projection is diffracted, the higher the precision of the normalized phase gradient measurement is; the more photons that are detected in total, the higher the precision of the normalized phase gradient measurement is.

The first term in Eq. 7-7 is the fundamental detection limit on the normalized phase gradient due to photon counting noise. No matter how small the image sensor pixels or how low the background noise of the sensor pixels is, this is the smallest normalized phase gradient that can be resolved by measuring the average angle of all N photons. The second term is the pixelation noise component. The more pixels that are used to predict the center of the projection spot, the more precise the normalized phase gradient measurement we can achieve. The third term is the background noise component (constant noise over all pixels, e.g., quantization noise, readout noise, or dark counts). The smaller the background noise, the more precise the measurement we can achieve. However, unlike in the second term, fewer pixels are desirable because the total background noise will be less. Therefore, there is an optimal number of sensor pixels in the normalized phase gradient measurement, which is close to three in each x and y dimension [7]. Our WIS operates close to this optimal number.

If the diffraction of the WIS apertures is not the Fraunhofer diffraction, the noise characteristics of the normalized phase gradient measurement will not be as neat as Eq. (7-7). However, as a rule of thumb, the tighter we can focus the light, the higher the normalized phase gradient sensitivity we can achieve.

7.3 Normalized phase gradient estimation in the frequency domain

In the previous section, we discussed the normalized phase gradient sensitivity that can be achieved in the presence of noise. The question is how we implement it. Generally, there are two ways. The first is to assign several dedicated pixels to each aperture (Fig. 5-4 (c)), and estimate the normalized phase gradient on each aperture individually. For example, the centroid and cyclic estimators fall in this category. These methods fail, however, when we decrease the spacing between apertures to increase the sampling rate of the WIS due to crosstalk between neighboring light projections (Fig. 7-5).

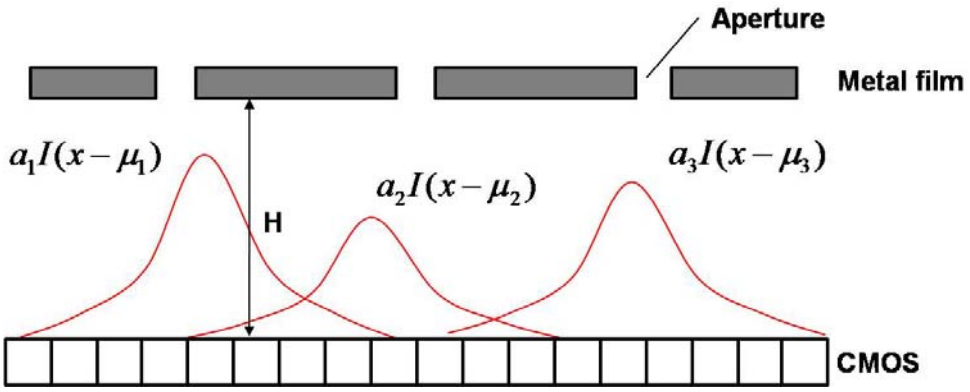

Figure 7-5 (color): Crosstalk between neighboring light projections. In a WIS with closely packed apertures, the crosstalk between light spot distributions $a_1I(x-\mu_1)$, $a_2I(x-\mu_2)$, and $a_3I(x-\mu_3)$ can be severe.

A second approach is to estimate the normalized phase gradient on all apertures at once. This way, the crosstalk will be considered useful signal. For example, let us assume the light projections in Fig. 7-5 are Gaussian functions. We can use the summation of

three Gaussian functions to fit the light distribution data, and find the parameters best describing the amplitudes and shifts of each light projection spot. The normalized phase gradient can be calculated from the shifts according to Eq. (5-1). However, when the estimation problem becomes 2D, and the number of light projection spots is more than ~10k, this estimation becomes a formidable task.

Fortunately, there is a frequency domain method [8] which can be used to estimate all normalized phase gradients on the WIS apertures at once, with no restriction from the crosstalk between neighboring light projection spots. This method utilizes the periodicity of the raw image data from the CMOS sensor (Fig. 5-4 (c)), and performs a spatial Fourier transform on the entire light distribution to determine the center positions of all the light spots simultaneously via an analysis in the spatial frequency domain.

In more specific terms, the distribution of aperture projections on the CMOS sensor can be considered a summation of two cosine functions in x and y directions modulated by the amplitude and spatial normalized phase gradient of the incoming wavefront:

$$I(x,y) = A(u,v)\left[2 - \cos(kx - H\frac{\lambda}{2\pi}\frac{\partial\phi(u,v)}{\partial u}) - \cos(ky - H\frac{\lambda}{2\pi}\frac{\partial\phi(u,v)}{\partial v})\right], \qquad (7\text{-}8)$$

where $A(u,v)$ and $\phi(u,v)$ are the amplitude and the phase of the wavefront at the aperture located at (u,v). $k = 2\pi / P$, where P is the aperture spacing. H is the distance from the aperture plane to the CMOS sensor pixels. We can rewrite the above equation as:

$$
\begin{aligned}
I(x,y) &= 1/2[2A(u,v) - C_x(u,v)\exp(ikx) - C_x^{*}(u,v)\exp(-ikx) \\
&\quad - C_y(u,v)\exp(ikx) - C_y^{*}(u,v)\exp(-ikx)] \\
C_x(u,v) &= A(u,v)\exp(-H\frac{\lambda}{2\pi}\frac{\partial\phi(u,v)}{\partial u}) \\
C_y(u,v) &= A(u,v)\exp(-H\frac{\lambda}{2\pi}\frac{\partial\phi(u,v)}{\partial v})
\end{aligned}
\quad . \qquad (7\text{-}9)
$$

In the frequency domain, the above equation becomes:

$$
\hat{I} = 1/2\left[4\hat{A} - \hat{C}_x * \delta(q_x - k) - \hat{C}_x^{*} * \delta(q_x + k) - \hat{C}_y * \delta(q_y - k) - \hat{C}_y^{*} * \delta(q_y + k)\right], \qquad (7\text{-}10)
$$

where * denotes a convolution operation and ^ denotes the Fourier transform. We can easily see each term representing a separate peak in the frequency domain, where the amplitude and the spatial normalized phase gradient information of the wavefront are now completely contained in each of the first harmonic terms. In order to restore them back to the spatial domain, we simply need to bandpass-filter out one of the harmonics, and perform an inverse Fourier transform on that region.

The crosstalk constraint, that previously limited our aperture spacing, is relaxed in this frequency domain algorithm. The algorithm admits crosstalk in its periodicity assumption and solves for the center positions of the mixed aperture projections simultaneously, whereas the previous centroid algorithm is only successful when the crosstalk is negligible. However, there is also a limit for this algorithm, because we need at least two pixels between neighboring apertures to sense the periodicity throughout the array of aperture projections. In the future work, we will leave a margin and choose three pixels as the target aperture spacing. If it succeeds, this will increase the sampling rate of the WIS from 11 μm to 6.6 μm, which will further improve the quality of wavefront image captured by the WIS and broaden the applicable areas for the WIS. For example,

in photography, where a optical system with demagnification is usually involved, the requirement on the sample rate of the image sensor is more stringent.

7.4 Conclusion

We have shown that WM is possible. In theory, we can measure both the amplitude and phase of a light wave in the microscope system accurately at the same time. In reality, there is some subtlety. On one hand, we are limited by the *N.A.* of the optical microscope system and detection sensitivity, thus we are not able to detect the high frequency components of the amplitude and phase information of light scattered by the specimen with the WIS. On the other hand, the microscope system with limited bandwidth ensures the unknown object wavefront is not too complicated (containing too much information) to be imaged correctly (without aliasing errors) by the WIS with certain sampling density. In the future, as we further increase the sampling density of the WIS, we might be able to image fast-changing wavefronts directly with our WIS. It will remove the limitation set by the optical system of the microscope.

The sensitivity of the normalized phase gradient measurement in the WIS is limited by the number of photons detected, the size of the pixel sensor and the background electronic noise. Under the Fraunhofer diffraction assumption, we can use $\Delta\theta = 1.22\lambda / D$ to characterize the anglular spread. If we only consider the photon counting noise, the precision of determining the normalized phase gradient will be $\delta\theta = \Delta\theta / N = 1.22\lambda /(N \cdot D)$ for recording N photons. In our WIS prototype,

$\delta\theta = 1.22 * 0.6\mu m / (10^6 \cdot 6\mu m) = 1 \times 10^{-7}$ radians, when our CMOS sensor collects 10^6 photoelectrons for measurement. This is considerably less than the 1×10^{-4} radians in our calibration experiment. Therefore, there is still room for us to improve the normalized phase gradient sensitivity of the WIS. We can either use image sensor with smaller pixels, less electronic noise, or adapt a better estimation method for the normalized phase gradient measurement.

Estimating the normalized phase gradient on all apertures at once seems to be the most important way to improve the normalized phase gradient sensitivity of the WIS. The frequency domain method is promising because it can both improve the performance and increase the calculation speed of our analysis.

Bibliography

1. M. Harker, and P. O'Leary, "Least squares surface reconstruction from measured gradient fields," in *2008 IEEE Conference on Computer Vision and Pattern Recognition (CVPR)*(Ieee, Anchorage, AK, USA, 2008), pp. 7 pp.-7 pp.
2. R. Frankot, R. Chellappa, H. Co, and C. El Segundo, "A method for enforcing integrability in shape from shadingalgorithms," IEEE Transactions on pattern analysis and machine intelligence **10**, 439-451 (1988).
3. T. Kuparinen, V. Kyrki, J. Mielikainen, and P. Toivanen, "On Surface Topography Reconstruction from Gradient Fields," (2007).
4. F. Roddier, and C. Roddier, "Wavefront reconstruction using iterative Fourier transforms," Applied Optics **30**, 1325-1327 (1991).
5. http://www.microscopyu.com/articles/formulas/formulasfielddepth.html.
6. R. E. Thompson, D. R. Larson, and W. W. Webb, "Precise nanometer localization analysis for individual fluorescent probes," Biophysical Journal **82**, 2775-2783 (2002).
7. K. Winick, "Cramér-Rao lower bounds on the performance of charge-coupled-device optical position estimators," Journal of the Optical Society of America A **3**, 1809-1815 (1986).
8. Y. Carmon, and E. N. Ribak, "Phase retrieval by demodulation of a Hartmann-Shack sensor," Opt. Commun. **215**, 285-288 (2003).

Summary

In this thesis, we have presented two new microscope imaging techniques: optofluidic microscopy (OFM) and wavefront microscopy (WM). Part I of the thesis focuses on OFM and comprises Chapter 2, 3 and 4; Part II focuses on WM and includes Chapter 5, 6 and 7.

In OFM research, we abandoned the format of conventional microscope imaging, which requires expensive lenses and a large space to magnify images in microscopes, and instead utilized microfluidic flow to deliver specimens across array(s) of micron-sized apertures defined on a metal-coated CMOS sensor to acquire direct projection images. The invention of OFM can potentially provide low-cost, compact, automated, and disposable cell imaging devices for biomedicine applications and bioscience research. It can also change the way we conduct certain experiments with the availability of tens of hundreds of microscopes on a single chip.

In Chapter 2, we demonstrated the first completely on-chip OFM prototype device. The prototype is as small as a dime, but can render microscope images comparable in quality to those of a conventional optical microscope with a 20× objective. We applied this device in imaging and quantitative phenotype characterization of *C. elegans* to demonstrate the capability of OFM for automated cell-level imaging.

In Chapter 3, we established a signal and system model for OFM imaging. We understood that OFM imaging is a three-stage system, including image collection, digital sampling, and reconstruction filtering. The resolution of OFM is determined by its PSF,

and it depends on both the size of OFM apertures and the height of the object to the OFM apertures. Experimentally we characterized that the ultimate resolution of the OFM device with 1 μm apertures was 0.9 μm and the resolution degraded to 3 μm at H = 2.5 μm; the ultimate resolution of the OFM device with 0.5 μm apertures was 0.8 μm and the resolution degraded to 2 μm at H = 2.5 μm. We found that the sampling rate and aliasing error of OFM are intertwined, and noticed that the aliasing artifact in our OFM image can be controlled to less than 0.4% when using the doubled sampling rate.

In Chapter 4, we presented a new on-chip phase imaging method – structured aperture interference (SAI), which does not require bulky and complicated optical components as in conventional phase imaging methods. We used the SAI wavefront sensor to characterize the phase profile of a Gaussian beam and an optical vortex quantitatively, and to image biological samples without artifacts under a 1:1 optical relay system. These results clearly demonstrated that it is feasible to create a phase sensitive OFM device on a chip based on SAI.

In WM research, we proposed a new microscopy concept – quantifying both amplitude and phase information of the microscope image of a biological sample simultaneously. The significance of our approach is that we can turn an optical microscope into a WM by simply adding our newly developed wavefront image sensor (WIS) to its camera port, allowing for quantitative phase mapping of biological specimens. This technique can be used with most optical microscope systems, and may facilitate the adaptive microscope imaging in deep tissues.

In Chapter 5, we demonstrated the enabling component of WM – the WIS. The WIS works in the high Fresnel number regime, and is used to accurately measure both

intensity and phase front variations (measured normalized phase gradient accuracy of 5×10^{-4} radians) of a light wave. Because we integrated all of the optical functionality on the WIS chip itself, when used in place of the conventional camera in a standard bright-field microscope, this sensor can transform the microscope into a WM to provide both bright-field (transmitted light intensity) and normalized phase gradient images.

In Chapter 6, we demonstrated the application of WM for biological imaging and showed its advantages over conventional differential interference contrast (DIC) microscopy. First, through imaging a live and wild-type hermaphrodite adult *C. elegans*, we demonstrated that WM generates consistent intensity and normalized phase gradient images for unstained specimens as compared to conventional microscope techniques. Second, through imaging a stained ascaris under cell division, we demonstrated that WM can render correct normalized phase gradient images, even for a specimen with strong absorption. In contrast, the DIC phase images are always contaminated by the absorption contrast. Third, through imaging a strongly birefringent ctenoid fish scale, we demonstrated that WM can be used to image a broad range of tissue samples without birefringent artifact, which is ubiquitous in DIC microscopes.

In Chapter 7, we took the phase term into consideration, and generalized the signal and system model of the microscope imaging to be suitable for analyzing the WM system. We proved that we can measure both the amplitude and phase of a light wave in a microscope system accurately at the same time. By using the ray transfer matrix method, we explained the reduction of the normalized phase gradient and the additional phase introduced to the object wavefront by the microscope optics. Based on Thompson's localization analysis and the assumption of Fraunhofer diffraction in the WIS, we

formalized the noise characteristics of the normalized phase gradient measurement. The fundamental normalized phase gradient sensitivity associated with the photon counting noise is 1×10^{-7} radians, which is much less than the measured 1×10^{-4} radians in our WIS prototype. It encourages us to further improve the performance of the WIS. We plan to use a frequency domain method to estimate the normalized phase gradient on all WIS apertures at once, and implement faster and better normalized phase gradient measurement in WM.

The invention of OFM and WM could reduce the cost and improve the efficiency and quality of microscope imaging in biological research and clinical diagnosis. We anticipate that they will generate a revolutionary impact on biological imaging. Our quantitative studies of OFM and WM imaging systems deepen our understanding about the nature of imaging, and should open up our views to future microscopy research.